

**ELECTROCHEMICAL AND CHEMICAL  
METHODS FOR THE FABRICATION OF  
FUNCTIONAL NANOCOMPOSITES**

By

Tianshi Zhang, B. Eng.

A Thesis

Submitted to the School of Graduate Studies

In Partial Fulfillment of the Requirements

For the Degree

Master of Applied Science

McMaster University

© Copyright by Tianshi Zhang, August 2016

MASTERS OF APPLIED SCIENCE (2016)

McMaster University

(Materials Science and Engineering)

Hamilton, Ontario

TITLE: Electrochemical and Chemical Methods for the Fabrication of Functional Nanocomposites

AUTHOR: Tianshi Zhang, B.ENG. (Changshu Institute of Technology, China)

SUPERVISOR: Professor I. Zhitomirsky

NUMBER OF PAGES: xvi, 125

## Abstract

Novel electrochemical and chemical strategies have been developed for the fabrication of functional nanocomposites. New scientific and engineering contribution of this work to colloidal nanotechnology included the development of advanced chelating dispersing agents, such as various small organic molecules and chelating polymers. The unique feature of such dispersion agents is their strong adsorption on the surface of different materials, which allows superior dispersion. The chelating monomers of chelating polymers, such as PAZO and PMSS provided multiple adsorption sites for bonding to metal atoms on the particles surface. We analyzed and developed new fundamental adsorption and dispersion mechanisms. An important finding was the possibility of co-dispersion and co-deposition of advanced materials such as oxides, nitrides, complex oxides and minerals using universal dispersing agents and formation of composites by EPD method.

It was found that Caffeic acid (CA) can be used as an efficient dispersing agent for the synthesis of ZnO nanorods of reduced size and a dispersing agent for the EPD of ZnO films. Another important achievement of this work was the application of tannic acid as an efficient capping and dispersing agent for synthesis and EPD of inorganic materials and composites. An important discovery was the use of lauryl gallate dispersant as a reducing agent for the synthesis of AgNp and a vehicle for particle dispersion and extraction in the liquid-liquid extraction method.

Further advancements in our new technologies allowed us to develop composite films using anodic EPD using weak polyelectrolytes, such as alginate. The composite coatings exhibited

protective and flame retardant properties. We analyzed the deposition mechanisms and kinetics as well as microstructure of the coatings. In another strategy, we developed electrochemical strategies for the deposition of composites, based on strong polyelectrolytes. The approach is based on the EPD of the polyelectrolyte molecules and electrosynthesis of EPD of ceramic particles. The electrostatic heterocoagulation mechanism was proposed for the deposit formation. We investigated the deposition kinetics, composition and microstructure of the composites prepared by the new strategies. The new electrochemical strategies can be used for the deposition of other composites, based on functional polymers with pH independent charge.

New methods have been developed for the chemical synthesis of PPy based composites, using PMSS, PMSS–SR11 and PMSS–SR31 as anionic dopants for chemical polymerization and dispersants for MWCNT. The composites showed promising performance for application in electrodes of electrochemical supercapacitors. Good electrochemical performance was achieved at high active mass loadings. The electrodes showed high capacitance, large voltage window and low impedance. The analysis of electrochemical testing results and chemical structure of PMSS, PMSS–SR11 and PMSS–SR31 provided an insight into the influence of the anionic functional groups on the capacitance and capacitance retention a high charge-discharge rates.

## **Acknowledgement**

First and foremost, I would like to express my sincerest gratitude to my supervisor, Professor Igor Zhitomirsky for his constant support through the whole journey of my master's studies and thesis writing. Your patience, guidance and brilliant advices on both my research and course make me feel really fortunate and enjoyable to be your student.

I would also like to thank Advanced Ceramics for their financial support and all my lab mates for your moral and experimental support.

Finally, I would like to thank the following individuals for their help in my research project:

Dr. Oleg Rubel for the adsorption analysis in DFT studies.

Dr. James Britten and Victoria Jarvis for XRD training and analysis.

Steve Kornic and Megan Fair for FTIR and UV-Vis training and analysis.

Marcia Reid for TEM training and analysis.

## Table of Contents

Abstract.....	iii
Acknowledgement .....	v
Chapter 1 Introduction .....	1
Chapter 2 Literature review .....	2
2.1 Polymer-matrix nanocomposites.....	2
2.1.1 Polymer - ceramic nanocomposites.....	2
2.1.2 Polymer - carbon nanotube nanocomposite.....	3
2.2 Fabrication techniques.....	5
2.2.1 Electrodeposition techniques .....	5
2.2.1.1 Electrolytic deposition .....	8
2.2.1.2 Electrophoretic deposition .....	10
2.2.1.3 Particle interactions.....	11
2.2.1.3.1 The DLVO theory .....	11
2.2.1.3.2 Other interparticle forces .....	16
2.2.1.4 Suspension stability and Particle Charging.....	18
2.2.1.4.1 Double layer and zeta potential.....	18
2.2.1.4.2 Influence of solvents on particle charging .....	22

2.2.1.4.3 Additives for particle charging .....	23
2.2.1.5 Solvents.....	23
2.2.1.6 Binders .....	25
2.2.1.8 Kinetics of electrophoretic deposition .....	28
2.2.2 Chemical techniques.....	32
2.2.2.1 Chemical Reduction.....	32
2.2.2.2 Chemical Polymerization.....	33
Chapter 3 Objectives.....	34
Chapter 4 Experimental Procedures.....	35
4.1 Materials.....	35
4.2 Materials Synthesis .....	39
4.2.1 Hydrothermal synthesis of ZnO nanorods.....	39
4.2.2 Chemical polymerization of PPy and PPy-MWCNTs .....	40
4.3 Fabrication of electrodes for electrochemical tests .....	41
4.4 Electrodeposition and adhesion test .....	42
4.5 In-situ deposition yield study .....	45
4.6 Materials characterization methods.....	46
4.6.1 X-ray diffraction analysis .....	46
4.6.2 FTIR and UV-Vis spectroscopy .....	46

4.6.3 Scanning and transmission electron microscopy .....	47
4.6.4 Thermogravimetric and differential thermal analysis .....	47
4.7 Electrochemical Tests .....	48
4.7.1 Cyclic voltammetry study.....	49
4.7.2 Impedance spectroscopy study .....	49
4.7.3 Corrosion study – Tafel plot.....	50
Chapter 5 Results and Discussions .....	52
5.1 Development of chelating dispersant .....	52
5.1.1 Chelating molecules .....	52
5.1.1.1 Using Caffeic acid as a capping agent for synthesis and dispersant for EPD.....	52
5.1.1.2 Electrophoretic Deposition of Functional Organic Molecules (BiqCOOH) and Composite Films .....	59
5.1.1.3 Using Tannic acid as a capping agent for synthesis and dispersant for EPD .....	65
5.1.1.4 Using Lauyl gallate as a reducing and dispersing agent for the fabrication of silver nanoparticles by liquid–liquid extraction.....	69
5.1.2 Chelating polymers.....	74
5.1.2.1 PAZO as universal dispersant for EPD.....	74
5.1.2.2 EPD of materials using poly(styrene-alt-maleic acid) as a dispersant.....	82
5.2 Electrophoretic deposition of ceramics using weak polyelectrolytes .....	85

5.3 Electrophoretic deposition of ceramics using strong polyelectrolytes..... 93

5.4 Electrophoretic deposition of quaternized hydroxyethylcellulose ethoxylate and composite materials. .... 102

5.5 Fabrication of PPy-MWCNT composites ..... 106

Chapter 6 Conclusions ..... 114

Chapter 7 Future work ..... 117

Bibliography ..... 119

## List of Figures

Figure 2-1 Schematic of EPD and ELD, showing electrophoretic motion of positively charged ceramic particles and ions $M^+$ , followed by hydrolysis of the ions to form colloidal nanoparticles and coagulation of the particles to form EPD and ELD deposits. ....	6
Figure 2-2: Major features of EPD and ELD.....	7
Figure 2-3 Schematic of the interaction energy as a function of separation between two particles in suspension.....	14
Figure 2-4 Total interaction energy between spherical particles as a function of interparticle separation at (a) low and (b) high electrolyte concentrations theory.....	15
Figure 2-5 Schematic illustrating electrical double layer structure and the electric potential near the solid surface with both Stern and Gouy layers indicated.....	19
Figure 2-6 Schematic of the double layer surrounding a charged particle and evolution of the electric potential from the surface potential, $\psi_0$ , to zero far from the particle.....	20
Figure 2-7 Zeta potential of ceramic particles versus pH of suspension. ....	21
Figure 4-1 Hydrothermal process for producing ZnO nanorods. ....	39
Figure 4-2 Chemical synthesis of (a) PPy powder and (b) MWCNT/PPy composite materials..	40
Figure 4-3 Fabrication of electrodes for electrochemical cells.....	41
Figure 4-4 A schematic of the setup of the deposition cell.....	42
Figure 4-5 Classification of adhesion test results. ....	44
Figure 4-6 A schematic of QCM analysis system. ....	45
Figure 4-7 A schematic of a standard three electrode electrochemical cell. ....	48

Figure 5-1 Chemical structure of CA.....	53
Figure 5-2 SEM image of ZnO nanorods, prepared by the hydrothermal synthesis method. ....	54
Figure 5-3 TEM images of ZnO prepared (A) without CA and (B) in the presence of CA. ....	55
Figure 5-4 X-ray diffraction pattern of ZnO prepared (A) without and (B) in the presence of CA (▼ - peaks, corresponding to the JCPDS file 36-1451).....	56
Figure 5-5 SEM images of the films prepared by EPD at deposition voltages of (A) 30 and (B) 50 V from 4 g L <sup>-1</sup> suspensions of ZnO, prepared in the presence of CA.....	57
Figure 5-6 FTIR spectra of deposit, obtained by EPD from 4 g L <sup>-1</sup> suspensions of ZnO, containing 1 g L <sup>-1</sup> CA. ....	58
Figure 5-7 Chemical structure of BiqCOOK molecule. ....	60
Figure 5-8 SEM images at different magnifications for the deposit obtained from 1 g L <sup>-1</sup> BiqCOOK solution in a water–ethanol solvent at a deposition voltage of 30 V. ....	62
Figure 5-9 SEM images of films, prepared from 1 g L <sup>-1</sup> BiqCOOK solution in a water–ethanol solvent, containing (a) 4 g L <sup>-1</sup> Pd, (b) 10 g L <sup>-1</sup> NiO at a deposition voltage of 30 V. ....	63
Figure 5-10 FTIR spectra of deposits, prepared from 1 g L <sup>-1</sup> BiqCOOK solution in a (a) water–ethanol solvent, containing (b) 4 g L <sup>-1</sup> Pd and (c) 10 g L <sup>-1</sup> NiO at a deposition voltage of 30 V. ....	64
Figure 5-11 Chemical structure of TA molecule. ....	66
Figure 5-12 TEM images of ZnO prepared (A) without TA and (B) in the presence of TA. ....	67
Figure 5-13 X-ray diffraction patterns of ZnO, prepared (A) without TA and (B) in the presence of TA (▼ - ZnO, JCPDS file 36-1451).....	68

Figure 5-14 SEM image of the film, prepared at a deposition voltage of 30 V from 4 g L <sup>-1</sup> ZnO suspensions in ethanol, containing 1 g L <sup>-1</sup> TA. ZnO was synthesized in the presence of TA, arrow show ZnO particles. ....	69
Figure 5-15 (A) Chemical structure of LG, (B) extraction of AgNp to the n-butanol phase using LG. ....	70
Figure 5-16 X-ray diffraction pattern of AgNp, obtained by reduction of AgNO <sub>3</sub> with LG (▼ - JCPDS file 04-0783). ....	71
Figure 5-17 TEM image of AgNp, obtained by reduction of AgNO <sub>3</sub> with LG, inset shows a corresponding selected area electron diffraction pattern. ....	72
Figure 5-18 FTIR spectra of AgNp extracted to n-butanol using LG.....	73
Figure 5-19 Structure and adsorption mechanism of PAZO on surface of inorganic material. ...	74
Figure 5-20 Deposit mass versus PAZO concentration in suspensions, containing 4 g L <sup>-1</sup> of (a) ZNO, (b) Al <sub>2</sub> TiO <sub>5</sub> , (c) ZrSiO <sub>4</sub> , (d) BN, (e)Hydrotalcite at a deposition voltage of 100 V and deposition time of 4 min. ....	77
Figure 5-21 SEM images of deposits, prepared from 1 g L <sup>-1</sup> PAZO solutions, containing 4 g L <sup>-1</sup> (A) ZnO, (B) Al <sub>2</sub> TiO <sub>5</sub> , (C) ZrSiO <sub>4</sub> , (D) BN, and (E) Hydrotalcite.....	79
Figure 5-22 UV–Vis spectra of the deposits, prepared from 1 g L <sup>-1</sup> PAZO solutions, containing 4 g L <sup>-1</sup> of (a) BN, (b) hydrotalcite, (c) ZnO and (d) ZrSiO <sub>4</sub> .....	80
Figure 5-23 Chemical structure of PMSS. ....	82
Figure 5-24 Deposit mass versus time for deposits prepared from 1 g L <sup>-1</sup> PMSS solutions, containing 10 g L <sup>-1</sup> (a) BN and (b) Si <sub>3</sub> N <sub>4</sub> .....	83

Figure 5-25 SEM images of deposits, prepared from 1 g L <sup>-1</sup> PMSS solutions, containing 10 g L <sup>-1</sup> (A) BN and (B) Si <sub>3</sub> N <sub>4</sub> . .....	84
Figure 5-26 Deposit mass versus time for deposits prepared from 4 g L <sup>-1</sup> huntite suspension, containing 1 g L <sup>-1</sup> sodium alginate.....	87
Figure 5-27 (A) XRD and (B) FTIR data for (a)as-received huntite, and (b) deposit, prepared from 4 g L <sup>-1</sup> huntite suspension, containing 1 g L <sup>-1</sup> sodium alginate (▼ – huntite, JCPDS file 014-0409). .....	88
Figure 5-28 SEM images at different magnifications for coatings, prepared from 4 g L <sup>-1</sup> huntite suspension, containing (A and B) 1 g L <sup>-1</sup> sodium alginate. ....	89
Figure 5-29 (a) TGA and (b) DTA data for (A) as-received huntite and deposits, prepared from 4 g L <sup>-1</sup> huntite suspension, containing (B) 1g L <sup>-1</sup> sodium alginate.....	90
Figure 5-30 Tafel plots for (a) uncoated stainless steel, and coated from 4 g L <sup>-1</sup> huntite suspension, containing and (b) 1 g L <sup>-1</sup> sodium alginate. ....	92
Figure 5-31 Chemical structure of PVT.....	93
Figure 5-32 Electrodeposition mechanisms, combining EPD of PVT and (a) electrosynthesis or (b) EPD of zirconia. ....	94
Figure 5-33 (A) Time dependence of QCM mass gain for deposition from solutions, containing (a) 0.7 mM ZrOCl <sub>2</sub> , (b) 0.05 g/L PVT, (c) 0.7 mM ZrOCl <sub>2</sub> and 0.05 g/L PVT at a cell voltage of 5 V, (B) deposit mass versus PVT concentration in 5 mM ZrOCl <sub>2</sub> solutions at a current density of 10 mA cm <sup>-2</sup> and a deposition time of 5 min.....	96

Figure 5-34 Deposit mass versus (A) zirconia concentration in 0.5 g L <sup>-1</sup> PVT solutions and (B) versus PVT concentration in 4 g L <sup>-1</sup> zirconia solutions at a deposition voltage of 100 V and deposition time of 5 min. ....	97
Figure 5-35 FTIR spectra of deposits, prepared from (a) 5 mM ZrOCl <sub>2</sub> solutions, containing 0.35 g L <sup>-1</sup> PVT at a current density of 10 mA cm <sup>-2</sup> and (b) 6 g L <sup>-1</sup> zirconia solutions, containing 0.5 g L <sup>-1</sup> PVT at a deposition voltage of 100 V. ....	98
Figure 5-36 (a) TGA and (b) DTA data for deposits, prepared from (A) 5 mM ZrOCl <sub>2</sub> solutions, containing 0.35 g L <sup>-1</sup> PVT and (B) 6 g L <sup>-1</sup> zirconia solutions, containing 0.5 g L <sup>-1</sup> PVT. ....	99
Figure 5-37 SEM images at different magnifications of deposits, obtained from 5 mM ZrOCl <sub>2</sub> solutions, containing (A, B) 0.35, (C, D) 0.7 and (E, F) 0.9 g L <sup>-1</sup> PVT at a current density of 10 mA cm <sup>-2</sup> . ....	100
Figure 5-38 Chemical structure of HCE. ....	102
Figure 5-39 (A) Time dependence of QCM mass gain for deposition from 0.05 g/L HCE solution at a cell voltage of 5V (B) Deposit mass versus HCE concentration in pure HCE solutions at a voltage of 30V and a deposition time of 5 min. ....	103
Figure 5-40 Deposit mass versus time for deposits prepared from (A) 2 g L <sup>-1</sup> HCE solutions, containing 4 g L <sup>-1</sup> (a) rutile, (b)Al <sub>2</sub> TiO <sub>5</sub> , (c)hydrotalcite and (d)CNT (B) 2 g L <sup>-1</sup> HCE and 0.5 g L <sup>-1</sup> gallocyanine solutions, containing 4 g L <sup>-1</sup> (b)Al <sub>2</sub> TiO <sub>5</sub> , (c)hydrotalcite and (d)CNT. ....	104
Figure 5-41 SEM images of deposits, prepared from 2 g L <sup>-1</sup> HCE solutions, containing 4 g L <sup>-1</sup> rutile, Al <sub>2</sub> TiO <sub>5</sub> , hydrotalcite and CNT. ....	105
Figure 5-42 Chemical structure of (A) PMSS and (B)PMSS-SR11 or PMSS-SR31. ....	106

Figure 5-43 SEM images of PPy prepared (A, B, C) without MWCNTs and (D, E, F) in the presence of MWCNTs. (A, D), (B, E) and (C, F) were prepared in the presence of PMSS, PMSS-SR11 and PMSS-SR31, respectively. ....	108
Figure 5-44 CVs at scan rates of (a) 2, (b) 5, (c)10, (d)20, (e)50, (f)100 $\text{mV s}^{-1}$ , for mass loading $\sim 20 \text{ mg cm}^{-2}$ (A) pure PPy electrodes and (B) PPy/MWCNT composite electrodes doped with PMSS. ....	109
Figure 5-45 CVs at scan rates of (a) 2, (b) 5, (c)10, (d)20, (e)50, (f)100 $\text{mV s}^{-1}$ , for mass loading $\sim 20 \text{ mg cm}^{-2}$ (A) pure PPy electrodes and (B) PPy/MWCNT composite electrodes doped with PMSS-SR11. ....	110
Figure 5-46 CVs at scan rates of (a) 2, (b) 5, (c)10, (d)20, (e)50, (f)100 $\text{mV s}^{-1}$ , for mass loading $\sim 20 \text{ mg cm}^{-2}$ (A) pure PPy electrodes and (B) PPy/MWCNT composite electrodes doped with PMSS-SR31. ....	110
Figure 5-47 Cs vs. scan rate of ES electrodes, prepared with pure PPy powders doped with (a) PMSS, (b) PMSS-SR11, (c) PMSS-SR11, and PPy/MWCNT composite materials with PPy/MWCNT mass ratio of 4:1, doped with (d) PMSS, (e) PMSS-SR11 and (f) PMSS-SR31, at .....	111
Figure 5-48 Nyquist plot of $Z^*$ (inset shows high frequency range) for ES electrodes, prepared with pure PPy powders doped with (a) PMSS, (b) PMSS-SR11, (c) PMSS-SR31, and PPy/MWCNT composite materials with PPy/MWCNT mass ratio of 4:1, doped with (d) PMSS, (e) PMSS-SR11 and (f) PMSS-SR31, at electrode mass loading of $\sim 20 \text{ mg cm}^{-2}$ . ....	112

## **Table of Contents**

Table 2-1 Major features compared between EPD and ELD. ....	7
Table 2-2 Examples of solvents used for electrodeposition .....	25
Table 4-1 Materials purchased from commercial suppliers.....	35

# Chapter 1 Introduction

Nanocomposite is a multiphase solid material where one of the phases has one, two or three dimensions of less than 100 nanometers, or structures having nano-scale repeat distances between the different phases that make up the material. Nanocomposites combine functional properties of individual component and exhibit improved properties. In general, nanocomposites usually can be divided into ceramic-matrix, metal-matrix and polymer-matrix nanocomposites.

The polymer-matrix nanocomposites have been attracting significant interest. Such composites are manufactured commercially for many diverse applications such as biomedical implants, corrosion inhibitors, sensors, electrical devices, etc. In the last few decades, there has been a strong emphasis on the development of polymeric nanocomposites, where at least one of the dimensions of the filler material is of the order of a nanometer. The final product does not have to be in nanoscale, but can be micro or macroscopic in size[1]. Currently, a lot of researchers are working on the fabrication techniques of polymer-matrix nanocomposites. The development of new electrochemical and chemical methods for the fabrication of functional nanocomposites are drawing tremendous attention.

This research resulted in the development of novel composites, which exhibited advanced functional properties. The development of advanced dispersing agents with strong adsorption as well as the development of electrophoretic deposition methods for the deposition of new polymers and composites were discussed in this thesis.

## Chapter 2 Literature review

### 2.1 Polymer-matrix nanocomposites

Polymer nanocomposites (PNC) consist of a polymer or copolymer having nanoparticles or nanofillers dispersed in the polymer matrix. These may be of different shape (e.g., platelets, fibers, spheroids), but at least one dimension must be in the range of 1–50 nm.

In 1998, Chemistry in Britain published an article titled “Nano sandwiches” [2], stating, ‘Nature is a master chemist with incredible talent’. Using natural reagents and polymers such as carbohydrates, lipids, and proteins, nature makes strong composites such as bones, shells, and wood. The properties of nanocomposite materials depend not only on the properties of their individual component, but also on their morphology and interfacial characteristics[2]. In my research, different types of polymer-matrix nanocomposites were investigated.

#### 2.1.1 Polymer - ceramic nanocomposites

There has been growing interest on producing new materials by filling polymers with inorganic natural and/or synthetic compounds. These composite materials possess high heat resistance, high dielectric constant[3], mechanical strength and impact resistance or present weak electrical conductivity and low permeability for gases like oxygen or water vapor. The selection of nanoparticles depends on the desired thermal, mechanical, and electrical properties of the

nanocomposites. For example, Al nanoparticles are often selected due to their high conductivity; calcium carbonate particles are chosen because of the relative low cost of the material, and silicon carbide (SiC) nanoparticles are used because of their high hardness, corrosion resistance, and strength[4].

Some efforts have been made to design coatings with composite ceramic-polymer microstructures, where a ceramic phase forms a connected network in a polymer matrix. Processing and microstructure development of ceramic and polymer coating prepared by depositing from a solution or dispersion have been of interest in last few years [5, 6]. Colloidal slurries of ceramics, sol-gel derived ceramics and polymers have been studied as coating systems.

### **2.1.2 Polymer - carbon nanotube nanocomposite**

There has been intense recent research focused on the fabrication, characterization and application of polymer-carbon nanotube composites, driven by a growing recognition of the unique mechanical, electrical, thermal and other materials-related properties of carbon nanotubes[7, 8]. Moreover, many potential applications have been proposed for carbon nanotubes, including conductive and high-strength composites; energy storage and energy conversion devices; sensors; field emission displays and radiation sources; hydrogen storage media and nanometer-sized semiconductor devices; probes and interconnects[9].

In the fabrication of high-quality polymer-carbon nanocomposites with predictable and optimal performance, a homogeneous dispersion of the carbon nanotubes in the polymer matrix is

required. Methodologies such as sonication of carbon nanotubes in a polymer solution[10, 11] and in situ polymerization in the presence of carbon nanotubes [12, 13] were developed for the homogeneous dispersion of the nanotubes in the polymer matrix. Improvement in the compatibility between the functionalized carbon nanotubes and the hosting polymer matrices has been discussed. For example, Tour, Krishnamoorti and coworkers[14] reported the functionalization of single-walled carbon nanotubes (SWNTs) with diazonium salts, and the functionalized SWNTs were used to form polystyrene-based composites [14]. These nanocomposites were found to have a lower percolation threshold than those obtained with pristine SWNTs. Sun and coworkers reported the functionalization and solubilization of SWNTs and multiple walled carbon nanotubes (MWNTs) with polystyrene copolymers bearing hydroxyl or amine moieties for the subsequent fabrication of polystyrene-carbon nanocomposite films using a wet-casting method. The films thus obtained were found to have excellent optical quality, and were free of any significant nanotube aggregation effects [15].

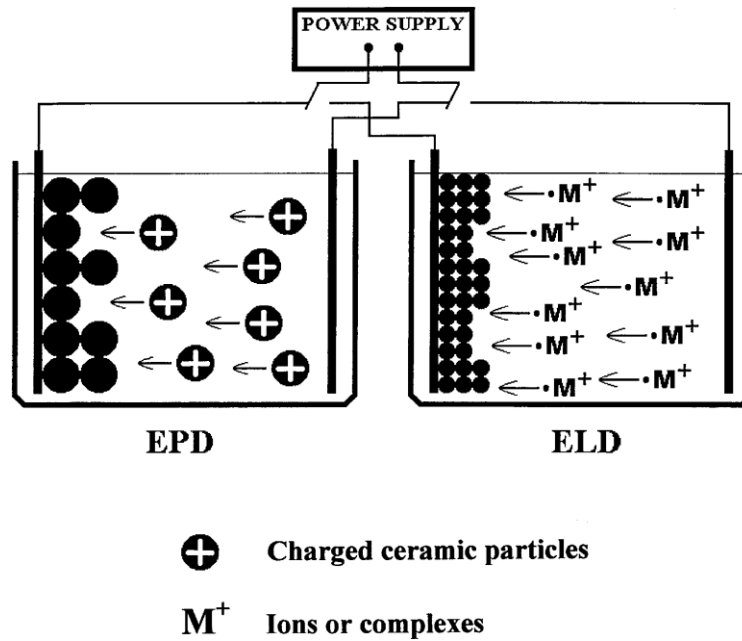
## 2.2 Fabrication techniques

### 2.2.1 Electrodeposition techniques

Electrochemical methods are increasingly being used for the preparation of thin films and coatings. Electrodeposition as a method to fabricate the organic-inorganic composite coatings is attracting significant research interest [16, 17]. Electrodeposition offers a lot of advantages for surface modification over other techniques:

- Capability of manufacturing nanostructured multi-component films.
- High purity of deposited materials.
- Applicable to substrates of complex shape.
- Can be used for deposition of ceramics, glasses, polymers, composites.
- Rigid control of the composition and microstructure of deposit.
- Low cost of equipment and materials.
- Easy to be scaled up to industry level.

Electrodeposition of organic and ceramic materials can be performed either by cathodic or anodic deposition methods. However, anodic deposition has limited utility regarding possible materials to be deposited by this method and substrates used for deposition. Cathodic deposition has important advantages for industrial applications. Two processes are commonly used to prepare organic and ceramic coatings by electrodeposition: the electrophoretic deposition (EPD) and the electrolytic deposition (ELD), shown in Figure 2-1.

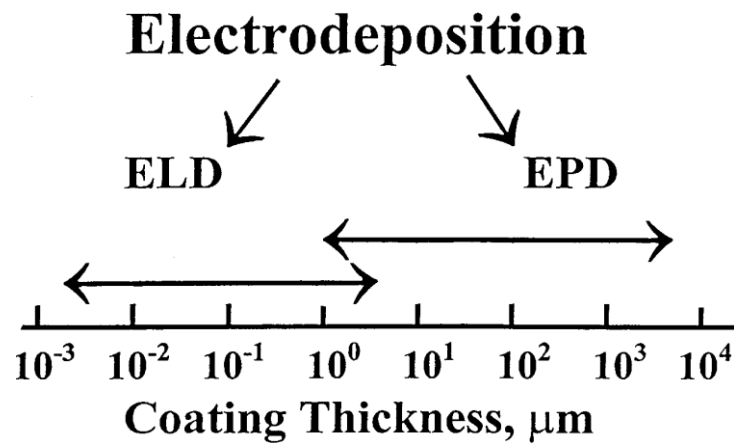


**Figure 2-1 Schematic of EPD and ELD, showing electrophoretic motion of positively charged ceramic particles and ions  $M^+$ , followed by hydrolysis of the ions to form colloidal nanoparticles and coagulation of the particles to form EPD and ELD deposits.**

EPD is achieved via motion of charged particles dispersed in a liquid medium toward the electrode under an applied electric field. Deposit formation on the electrode is achieved via particle coagulation. ELD leads to thin ceramic films from solutions of metal salts by production of colloidal particles in electrode reactions. Thus, electrode reactions in ELD and electrophoretic motion of charged particles in EPD result in the accumulation of ceramic particles and formation of ceramic films at the relevant electrodes[18]. The distinguishing features of the two methods were compared in table 2-1. The range of thickness of coating deposited by these techniques is shown in Figure 2-2. EPD is an important tool for the preparation of thick ceramic films. ELD enables the formation of nanostructured thin ceramic films.

**Table 2-1 Major features compared between EPD and ELD.**

	<b>EPD</b>	<b>ELD</b>
<b>Moving species</b>	<b>Particles</b>	<b>Ions</b>
<b>Preferred solvent</b>	<b>Organic</b>	<b>Water</b>
<b>Electrode reactions</b>	<b>Not involved</b>	<b>Involved</b>
<b>Deposition rate</b>	<b>High</b>	<b>Low</b>
<b>Particle size in film</b>	<b>Micro</b>	<b>Nano</b>
<b>Films thickness</b>	<b>1<math>\mu</math>m- 1mm</b>	<b>10-1000nm</b>

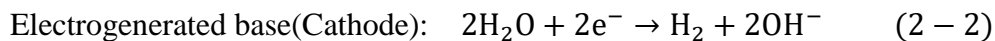
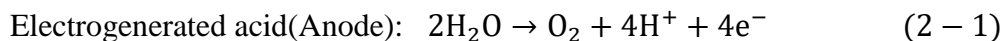
**Figure 2-2: Major features of EPD and ELD.**

Successful applications of electrodeposition require understanding of the deposition mechanisms. It is important to note that the hydrolysis reactions in ELD and the electrophoretic

motion of charged particles in EPD method result in the accumulation of ceramic particles at the electrode. Deposit formation is achieved via particle coagulation. A thorough understanding of the mechanisms of particle coagulation is crucial for successful electrodeposition and the development of new strategies for the fabrication of advanced organic-inorganic coatings. To better understand the mechanisms of electrodeposition, the fundamentals of ELD and EPD process will be discussed in the following part. The topics include the classical Derjaguin-Landau-Verwey-Overbeek (DLVO) theory of colloidal stability, forces between colloidal particles, additives used in bath formulations, and other factors influencing deposit stability and structure formation.

### 2.2.1.1 Electrolytic deposition

In the electrolytic deposition process, the hydrolysis of water which will produce  $H^+$  and  $OH^-$  at anode and cathode electrode surface respectively (Eqs.(2-1)-(2-2)), resulting in a significant decrease in pH value near the anode and increase in pH value near cathode [19]:



Various cationic species could be hydrolyzed by an electrogenerated base to form colloidal particles of oxides, hydroxides or peroxides.[20, 21] It was shown that electrosynthesis is similar to the wet chemical method of powder processing that makes use of electrogenerated base instead of alkali [22]. Hydrolysis reactions result in the accumulation of colloidal particles near the electrode. The mechanism for deposition proposed in [22] is based on the DLVO theory of

colloidal stability. It was shown [22] that the formation of a deposit is caused by flocculation introduced by the electrolyte. It is important to note that some pH changes take place, even at open circuit [23], leading to deposit formation.

ELD enables rigid control of film thickness, uniformity and deposition rate. The uniformity of ELD films results from the insulating properties of the deposits and the electric field dependence of the deposition rate. It was pointed out that the coagulation of colloidal particles near the cathode could be enhanced by the electric field and electrohydrodynamic flows, resulting from the cathodic reactions. Moreover, particle coagulation could also be enhanced by columbic attraction [24], resulting from ion correlation and depletion forces. Cationic surfactants and polyelectrolytes act as electrolytes in compressing the double layer of ceramic particles, resulting in particle flocculation and increasing the deposition process efficiency. Cathodic reactions result in a significant increase in pH value near the cathode, and it is expected that the colloidal particles formed near the cathode could be negatively charged [25]. The rate of  $\text{OH}^-$  generation is of paramount importance for the deposition process. When the rate of  $\text{OH}^-$  generation is faster than the rate of  $\text{OH}^-$  consumption by hydrolysis reactions at the electrode, a fraction of the  $\text{OH}^-$  ions generated at the cathode is transported away by the electric current and diffusion. In this case, the high pH boundary moves away from the electrode surface, resulting in lower adhesion of the deposits. The particle formation kinetics and deposit composition are influenced by solvent, additives, temperature and current density[22].

### **2.2.1.2 Electrophoretic deposition**

The mechanisms of the deposit formation of EPD have been discussed in numerous publications. One hypothesis is that charged particles undergo reactions at the electrode, which neutralize them. A difference in pH near the electrodes compared with the rest of the suspension is believed to play a major role in this reduction of charge. The competing forces governing the formation of deposit in the vicinity of the electrode include: the Van der Waals' force between particles; the interparticle repulsion of charged particles; the interaction of the deposit forming particles and ions or electrolytes in the suspension; and the pressure exerted by the motion of the charged particles under the influence of applied electric field.

According to Hamaker and Verwey [26], the formation of a deposition by electrophoresis is similar to the formation of sediment due to gravitation. It was supposed that applied electric field exerts sufficient force to overcome particles mutual repulsion. It is important to note that electrophoresis results in the accumulation of charged particles at the electrode surface. The deposit formation is achieved via the particle coagulation, which is influenced by the electrode reactions, solvents, additives and other factors [16].

In several experiments [27-30], EPD of ceramic particles was performed in the presence of electrolytes and polyelectrolytes. These additives are adsorbed on the particles to create positive charges and stabilize the suspensions. The additives are also important for the deposition of uniform and adherent deposits. EPD of ceramic particles could be associated with ELD of hydroxides or alkoxides, which form an adhesive matrix [30]. The adhesive materials promote particle coagulation and bind the particles to the substrate. Therefore, the binder materials may

enhance the effect of the Van der Waals' force. The water content and electrolyte concentration in the bath was also reported as a key factor during deposition process [31].

EPD of composite materials is an area of intense interest. Many important advantages of EPD were cited [17, 32, 33], which make this technique important for various applications. EPD can be applied to organic and inorganic nanoparticles for the fabrication of advanced functional composite materials. Moreover, EPD can be combined with other electrochemical strategies[30].

### **2.2.1.3 Particle interactions**

#### **2.2.1.3.1 The DLVO theory**

The state of dispersion of particles in suspension can be controlled by careful manipulation of the interparticle forces and their interactions. A quantitative description of the relationship between stability of colloidal suspension and energies of interactions between colloidal particles and other surfaces in a liquid has been given by the classical DLVO (Derjaguin-Landau-Verwey-Overbeek) theory [34]. The fundamental mechanisms of EPD have been largely denoted in literatures primarily in the framework of the DLVO theory.

There are some critical assumptions in the DLVO theory [35]:

- Infinite flat solid surface
- Uniform surface charge density

- No redistribution of surface charge
- No change of concentration profiles of both counter ions and surface charge determining ions,
- Solvent exerts influences via the dielectric constant only

According to this theory, the stability of a colloidal system is determined by the total pair interaction between colloidal particles, which consists of columbic double-layer repulsion and Van der Waals' attraction. So, the total energy  $V_T$  of interaction of two isolated, identically charged particles may be defined as:

$$V_T = V_A + V_R \quad (2 - 3)$$

The attractive energy  $V_A$  of the London-Van der Waals' interaction between two spherical particles can be expressed by:

$$V_A = -\frac{A}{6} \left( \frac{2}{s^2 - 4} + \frac{2}{s^2} + \ln \frac{s^2 - 4}{s^2} \right) \quad (2 - 4)$$

Where A is the Hamaker constant  $s = 2+D/r$ , with D the shortest distance between the two spheres and r the particle radius. If  $D \ll r$ , Equation (2-4) can be simplified to:

$$V_A = -A \frac{a}{12H} \quad (2 - 5)$$

The coulombic double-layer repulsion repulsive energy  $V_R$  is:

$$V_A = 2\pi\epsilon\epsilon_0 a\psi^2 \ln[1 + e^{-\kappa H}] \quad (2 - 6)$$

Where  $\epsilon$  is the dielectric constant of the solvent,  $\epsilon_0$  is the vacuum dielectric permittivity,  $\psi$  is the surface potential,  $1/\kappa$  is the Debye length:

$$\kappa = \left( \frac{e^2 \sum n_i z_i^2}{\epsilon \epsilon_0 k T} \right)^{1/2} \quad (2 - 7)$$

Where  $e$  is the electron charge,  $k$  is the Boltzman constant,  $T$  is the absolute temperature,  $n_i$  is the concentration of ions with valence  $z_i$ , Repulsion between colloidal particles is directly related to the diffuse layer charge on the particles.

A schematic plot of  $V_R$  and  $V_A$  versus  $D$  is shown in Figure 2-3[36] . It shows the Van der Waals attraction energy, coulombic double-layer repulsion energy, and the resultant total energy as a function of distance from the surface of a spherical particle. The DLVO theory explains the potential energy curve for the interaction. A peak of height  $E_B$  is located slightly away from the surface, as the coulombic double-layer repulsion energy dominates the Van der Waals attraction energy. The peak is known as the energy barrier and this is the energy barrier to particle coagulation[35]. If the particles are closer than the energy barrier ( $E_B$ ) the adhesion of particles is irreversible. The coulombic double-layer repulsion energy is dependent on the concentration and valence state of electrolyte ions as shown in Equations (2-6) and (2-7). Therefore, the total energy is strongly influenced by the concentration and valence state of counter-ions.

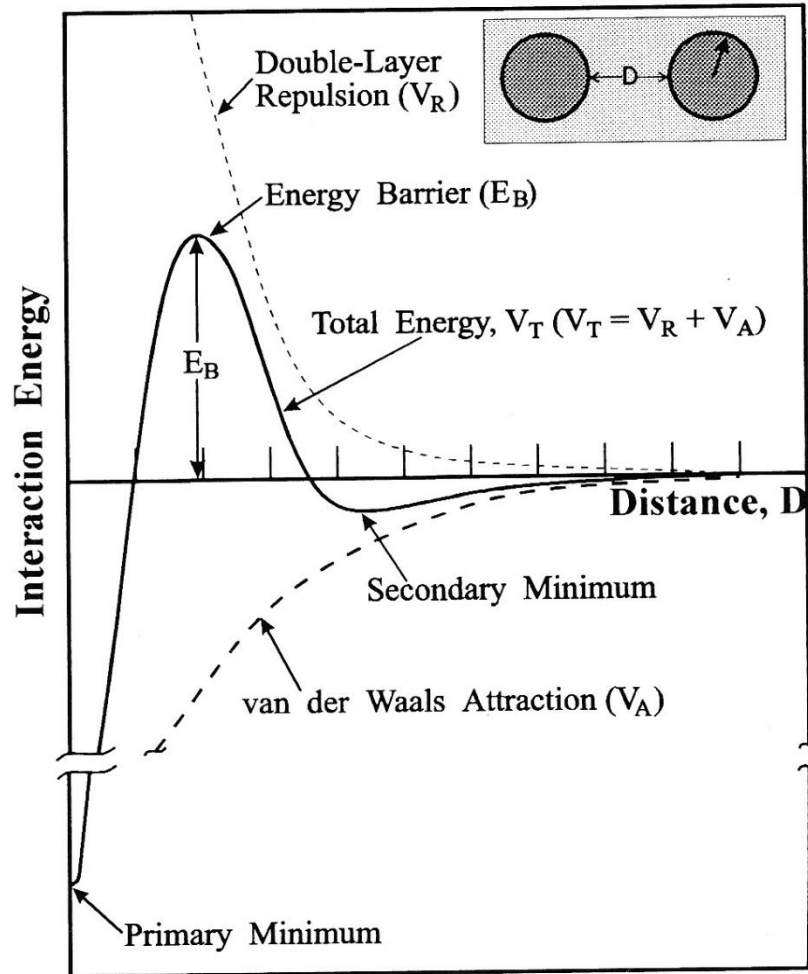


**Figure 2-3 Schematic of the interaction energy as a function of separation between two particles in suspension.**

The DLVO theory describes the potential energy curve for pair interaction, as shown in Figure 2-4(a). When the diffuse-layer repulsion is sufficiently high compared to the Van der Waals' attraction, the total energy of particle interaction exhibits a maximum, which makes an energy barrier to particle coagulation. The thickness of double layer (characterized by the Debye length,  $1/\kappa$ ) is very sensitive to the concentration of electrolyte [34]. The DLVO theory explains

the existence of a critical electrolyte concentration (flocculation value) for coagulation, decreasing with the valence of the electrolyte ions of a charge opposite to that of colloidal particles (rule of Schulze and Hardey) [34]. It was denoted that the potential energy peak decreases as the electrolyte concentration increases. As the energy barrier disappears, coagulation becomes possible (Figure 2-4b).

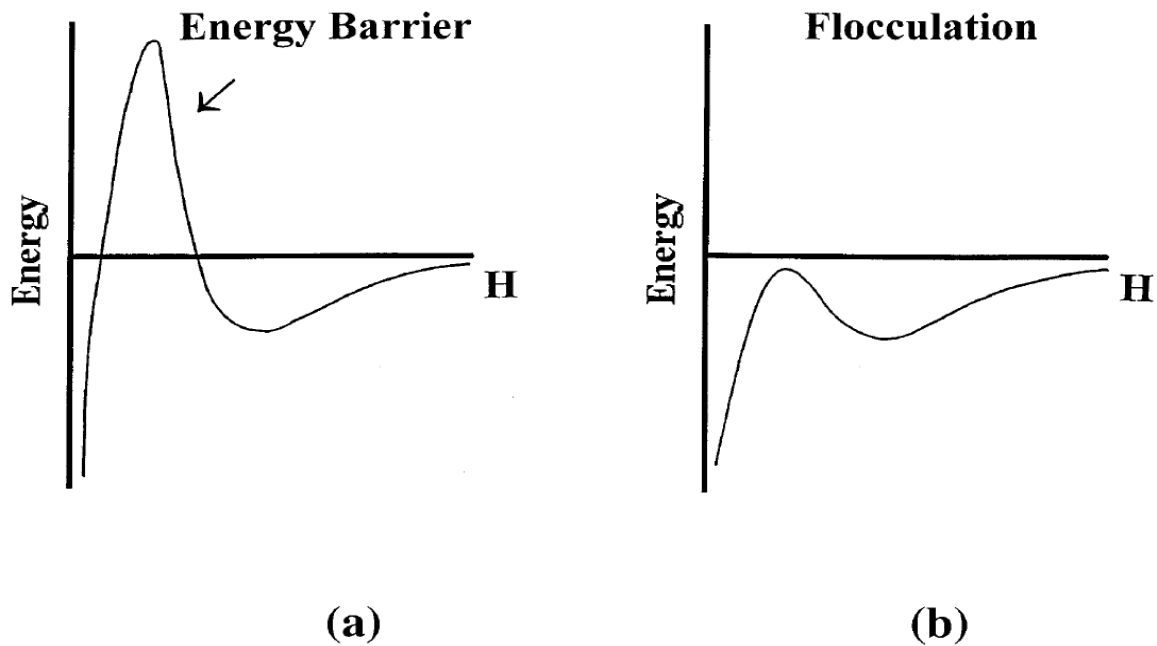
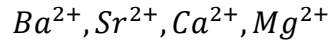


**Figure 2-4 Total interaction energy between spherical particles as a function of interparticle separation at (a) low and (b) high electrolyte concentrations theory.**

Flocculation by ions compressing the double layer also follows the Hofmeister series [34].

Within the series of ions of the same charge, the flocculation value increases in the order:





Therefore, a negatively charged sol is flocculated by large cations at a smaller concentration than by small cations of the same valence. The flocculation value was found to be in the range 20-200 for monovalent ions, 0.3-3 for divalent ions, and 0.003-0.1 for trivalent ions [34]. Flocculation values are affected by sol concentration, temperature, particle size of the colloid, and chemical nature of the sol.

#### **2.2.1.3.2 Other interparticle forces**

In the original DLVO theory, only the Van der Waals and electrostatic interactions were considered. Now it has also been identified that in addition to these forces, other physical interactions have to be considered. The attractive ion correlation force between particles could be significant enough to cause aggregation and flocculation of colloidal particles [37]. Ions present in ELD and EPD baths could also influence particle interactions. Electric field-induced aggregation of fine ceramic particles has been observed in the bulk of suspensions during EPD [38]. Forces of other origins, such as long-range attractions [39], electrohydrodynamic flows [40], polarization interaction, and capillary interactions etc., can also act between the particles.

It is important to note that stabilization of colloidal dispersions may also be influenced by steric stabilization and structural forces. These mechanisms become important when there are macromolecules adsorbed or bounded to the particle surface. Stabilisation is caused by the repulsion between these adsorbed macromolecules. The steric stabilization forces are generally

short-range forces ( $< 2$  nm) [41]. Presence of these forces can also change the shape of the potential well that controls the particle- substrate interaction. The addition of polymers to a colloidal suspension might lead to both attractive and repulsive forces. In other words, polymer adsorption may lead to colloid stability or to particle flocculation. Steric repulsion depends on the thickness of the adsorbed layer, the configuration of the polymer, the firmness with which the polymer is anchored to the surface, and the fraction of molecules adsorbed. Adsorbed polyelectrolytes or neutral polymers may induce flocculation by charge neutralization or bridging flocculation [42, 43]. According to [44, 45], the attraction between colloidal particles and polyelectrolytes includes electrostatic, hydrophobic, and dipole-dipole interactions. The interaction between two charged surfaces neutralized by grafted polyelectrolytes and counter-ions has been studied in [42]. In salt-free systems, a long-range repulsion due to free counter-ions and short-range bridging attraction was considered. It was demonstrated that the addition of salts screens the long-range repulsion. The flocculation or stabilization of colloidal particles may also be induced by non-adsorbing polymers. Addition of non-adsorbing polymer may lead to depletion flocculation or depletion stabilization [46].

Well dispersed and stable suspensions are very important for the successful deposition. In general, suspensions can be dispersed by electrostatic, steric, or electrosteric stabilization mechanisms. The suspension stability is characterized by settling rate and tendency to undergo or avoid flocculation. Suspensions containing colloidal particles which are  $1\ \mu\text{m}$  or less in diameter tend to be stable due to Brownian motion of the particles. Particles larger than  $1\ \mu\text{m}$  require continuous hydrodynamic agitation to remain in suspension. Flocculating suspensions settle rapidly and form low density, weakly adhering deposits. It is important to note that deposition will

not occur if a suspension is too stable, because the repulsive forces between the particles will not be overcome by the electric field. According to some models for EPD, the suspension should be unstable in the vicinity of the electrodes [36]. This local instability could be caused by the formation of ions from electrolysis or discharge of the particles. These ions then cause flocculation close to the electrode surface. Most investigators use zeta ( $\zeta$ ) potential or electrophoretic mobility to characterize a suspension

## **2.2.1.4 Suspension stability and Particle Charging**

### **2.2.1.4.1 Double layer and zeta potential**

A suspension for EPD is a complex system, in which each component has a certain effect on deposition efficiency. It is critical to gain well dispersed and stable suspensions.

In the EPD process, the charged particles in a suspension are forced to move toward an electrode under the influence of an applied electric field. Very often charged particles in a suspension are covered by counter ions, and the concentration of counter ions around the particles is much higher near the surface of the particles and decreases as the distance from the surface increases. Such inhomogeneous distributions of ions close to the particle surface result in the formation of so called double-layer, as shown in Figure 2-5[35].

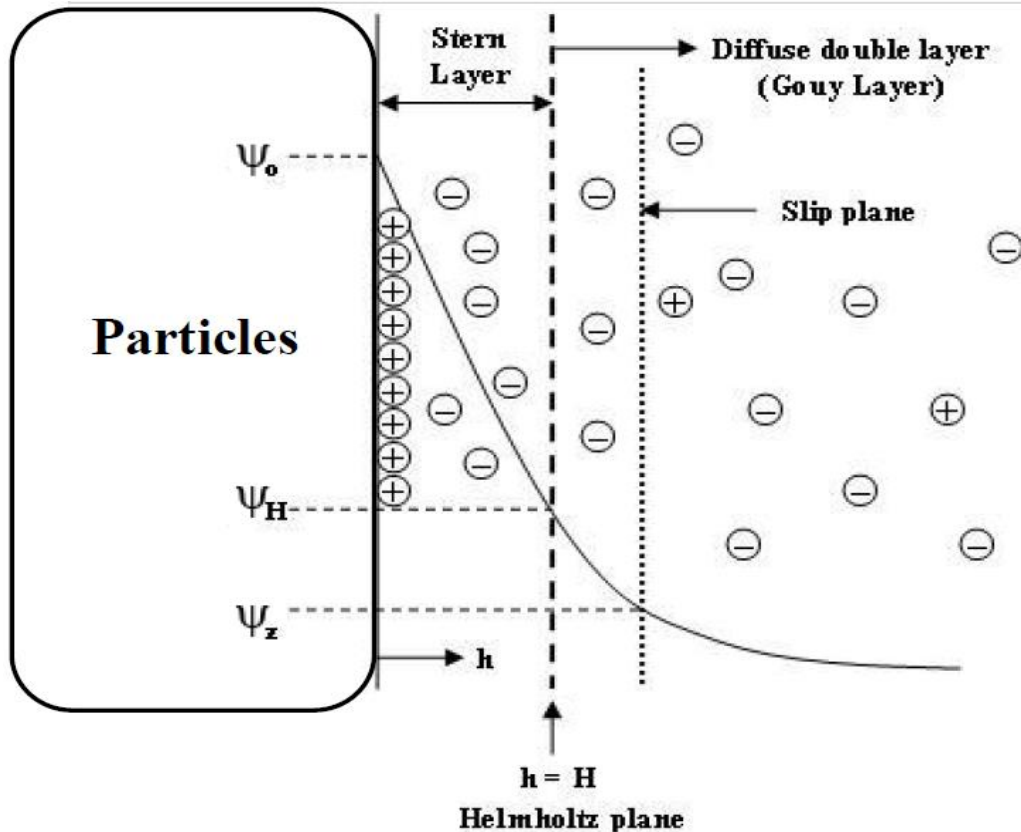


**Figure 2-5 Schematic illustrating electrical double layer structure and the electric potential near the solid surface with both Stern and Gouy layers indicated.**

The double layer is composed of Stern layer and diffuse double layer or Gouy layer, and these two layers is separated by Helmholtz plane. The electric potential reduces linearly in the Stern layer. However, in diffuse double layer, the counter ions diffuse freely and the potential does not decrease linearly. The motion of these ions and the particle are in opposite directions when an electric field is applied. But, some ions are also attached to the particle, and as a consequence, a fraction of these ions which are surrounding the particle will not move in the opposite direction but move along with the particles. The potential at the surface of shear, the boundary between the

electrolyte solution moving with the particle and the electrolyte solution, which does not move with the particle, is called the zeta-potential,  $\psi_\xi$ , which is schematically illustrated in Figure 2-6 [47]. Zeta-potential is the principal parameter determining the electrokinetic behaviour of the particle. In principle, a particle with a negative surface charge can show a positive zeta-potential.

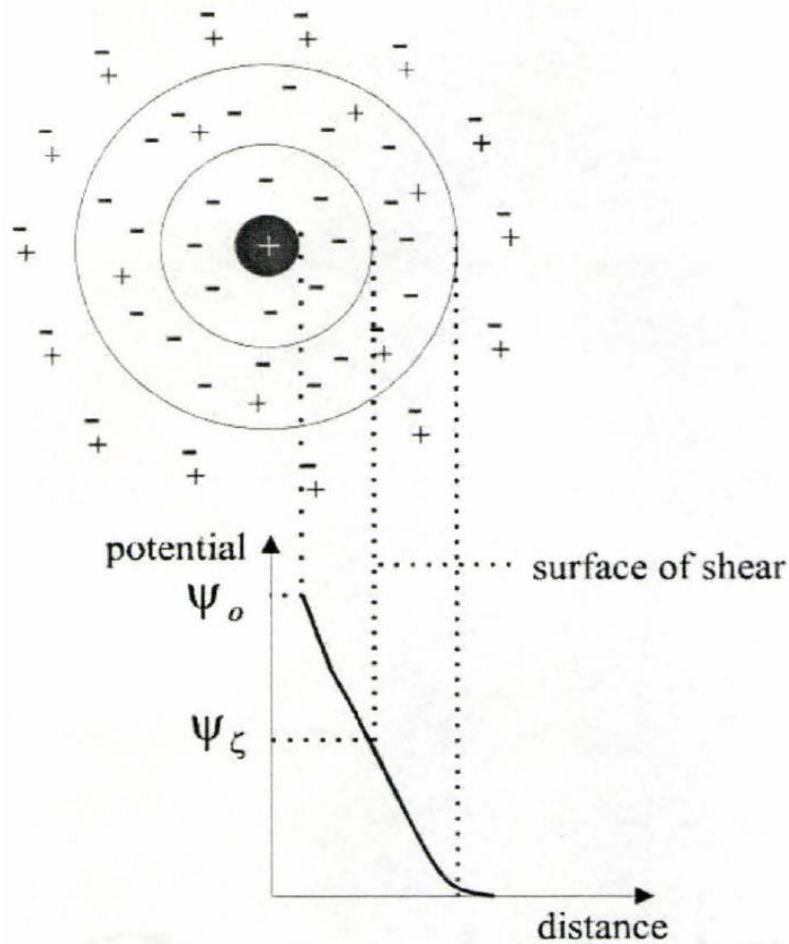


**Figure 2-6 Schematic of the double layer surrounding a charged particle and evolution of the electric potential from the surface potential,  $\psi_0$ , to zero far from the particle.**

For aqueous suspensions of ceramic powders, especially oxides, the  $\zeta$  potential changes with pH if  $H^+$  and  $OH^-$  are potential-determining ions, showing an isoelectric point (IEP) (Figure 2-7).  $\zeta$  potential is positive at low pH and negative at high pH.

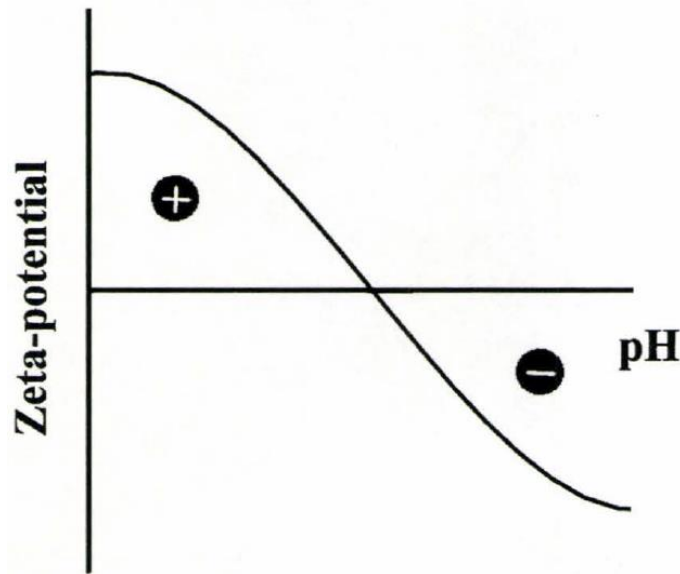
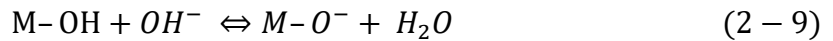


**Figure 2-7 Zeta potential of ceramic particles versus pH of suspension.**

According to the DLVO theory,  $\zeta$  potential is important for the stability of colloidal dispersions. The  $\zeta$  potential indicates the degree of repulsion between adjacent, similarly charged particles in the dispersion. A high  $\zeta$  potential will confer stability, however when the potential is low, attraction overcomes repulsion and the dispersion will break and flocculate. So, colloids with high  $\zeta$  potential are electrically stabilized while colloids with low  $\zeta$  potentials incline to coagulate or flocculate.

#### 2.2.1.4.2 Influence of solvents on particle charging

In aqueous media, the charge at the particle-solvent interface could originate from adsorption or desorption of ions, or dissociation of surface groups. Surfaces of oxide particles dispersed in water tend to coordinate water molecules to form hydroxylated surfaces. The surfaces may become positively or negatively charged, depending on pH:



Particle charging is accomplished by electron transfer between the particle and solvent in non-aqueous media [48]. The charge on a colloidal particle could originate from the solvent. Different solvents will cause different charging mechanism. Alcohols, water, organic acids are viewed as proton donors and are critical for particle charging. A mixture of solvents may also be helpful to accomplish particle charging [49].

Damodaran and Moudgil [50] have suggested a mechanism of particle charging in organic solvents. They proposed that the adsorbed alcohol ionized into a protonated alcohol and an alkoxide ions, and then protonated alcohol dissociate and desorbed into the solution, leaving the proton on the particle surface.

#### **2.2.1.4.3 Additives for particle charging**

A wide variety of additives can be used to control particle charge so as to produce well-dispersed suspensions, such as acids [29, 50], I<sub>2</sub>-H<sub>2</sub>O-acetone [51], NH<sub>4</sub>OH [52], and phosphate ester [53]etc. Recently, increasing attention has been directed on the utilization of polymer additives to induce steric stabilization, where the organic macromolecules are attached to the particle surface, or depletion stabilization, where the macromolecules are free in suspension. The steric stabilization is effective in both aqueous and non-aqueous media. Polyelectrolytes are widely used additives that can impart electrostatic and steric stabilization to a colloidal dispersion. The polyelectrolytes can be categorized into two groups: strong polyelectrolytes, for which the degree of ionization is independent of the solution pH, and weak polyelectrolytes, for which the degree of ionization is determined by the solution pH. Poly(ethylenimine) (PEI) is a weak cationic polyelectrolyte. An increase in pH decreases the charge of PEI. In contrast, poly(diallyldimethyl ammonium chloride) (PDDA) is a strong polycation because of its quaternary ammonium group, and the degree of dissociation of the ionic groups is nearly pH-independent over a wide pH range. PEI and PDDA were used to stabilize ceramic suspensions, and as additives for particle charging and electrodeposition of various materials [29, 54].

#### **2.2.1.5 Solvents**

Solvents act as vehicles that carry the ceramic particles in suspensions (EPD) or ions in solutions (ELD). The solvent used in electrodeposition must dissolve inorganic salts and organic

additives. There are two principal types of solvents used for electrodeposition: water and organic liquids (Table 2-2). ELD needs a sufficient amount of water for base generation in cathodic reactions [55]. Non-aqueous solvents prevent the deposit from hydrating. It is known that methanol is capable of extracting non-bridging hydroxo groups and free water [56]. Mixed methyl alcohol-water and ethyl alcohol-water solutions were found to be preferable in order to reduce cracking and porosity in the electrolytic deposits [55, 57].

The addition of alcohols to aqueous solutions reduces the total dielectric constant of the solvent, and thus reduces the solubility of the deposits. It is in this regard that deposition experiments performed in mixed methyl alcohol-water solutions indicate a significant enhancement of the deposition rate [58]. Repulsion between colloidal particles formed near the electrode is related to the diffuse-layer charge on the particles. The thickness of the double layer decreases with decreasing dielectric constant of the solvent, promoting particle coagulation. Solvents for EPD should be inert with respect to the powder. Organic liquids are superior to water as a suspension medium for EPD. The use of water-based suspensions causes gas formation from the hydrolysis of water, preventing the deposition of a uniform adherent layer and yielding pinholes. A variety of non-aqueous organic solvents (Table 2-2) are commonly used to prepare suspensions for EPD. The charge on a colloidal particle could originate from solvents. Alcohols are known to behave as proton donors and are important for particle charging. A mixture of solvents may also be useful to achieve particle charging [49]. The addition of alcohols to aqueous suspensions of titania-containing electrolyte [59] resulted in a shift of the IEP towards higher pH values, or the absence of IEP. The experimental results presented in [59] indicate that the dielectric constant of the mixed solvent could be the factor that governs the shift of IEP.

**Table 2-2 Examples of solvents used for electrodeposition**

Solvent	Method of deposition	Deposited material
Water	ELD EPD	Al <sub>2</sub> O <sub>3</sub> -Cr <sub>2</sub> O <sub>3</sub> [55], ZnO [56] Al <sub>2</sub> O <sub>3</sub> [57]
Dimethylformamide <sup>a</sup>	ELD	Y <sub>2</sub> O <sub>3</sub> [58], TiO <sub>2</sub> [59]
Methyl alcohol-water	ELD	TiO <sub>2</sub> [5], RuO <sub>2</sub> -TiO <sub>2</sub> [60]
Ethyl alcohol-water	ELD EPD	CeO <sub>2</sub> [61], SnO <sub>2</sub> [62] CaSiO <sub>3</sub> [63]
Isopropyl alcohol	EPD	Hydroxyapatite [40,41]
Isopropyl alcohol <sup>a</sup>	ELD	YBa <sub>2</sub> Cu <sub>3</sub> O <sub>7-x</sub> [65]
Ethyl alcohol-acetylacetone	EPD	MgO, Al <sub>2</sub> O <sub>3</sub> [53]
Glacial acetic acid	EPD	PZT [66]
Ethyl alcohol	EPD	Al <sub>2</sub> O <sub>3</sub> , ZrO <sub>2</sub> [67]
Dichloromethane	EPD	β-alumina [68]
Acetone	EPD	YSZ [69]
Acetylacetone	EPD	YSZ [69]
Cyclohexanone	EPD	YSZ [69]
Methyl ethyl ketone	EPD	Al <sub>2</sub> O <sub>3</sub> [70]
Toluene-ethyl alcohol	EPD	Al <sub>2</sub> O <sub>3</sub> [70]

PZT, lead zirconate titanate; and YSZ, yttria-stabilized zirconia.

### 2.2.1.6 Binders

A binder is added to suspensions or solutions in order to increase the adherence and strength of the deposited material and prevent cracking. EPD of sub-micrometer particles offers advantages in the fabrication of uniform ceramic coatings with dense packing and good sinterability. However, the use of fine particles initiates deposit cracking, which could be prevented by the use of binder. The optimal amount of binder depends on the particle size and particle surface area. Many different binders have been used for non-aqueous EPD, including nitrocellulose [27, 60], alkyd resin [33], dewaxed shellac [60], and polyvinyl butyral (PVB) [28, 54]. It is advantageous to use a binder material, which also acts as a dispersant. Various dispersing

aids with an inherent binding effect were used in [29]. Compared with non-aqueous solvents, the variety of water-soluble binders and dispersants is restricted. The low strength of water-soluble binders limits their applicability. Polyvinyl alcohol is an important binder material for aqueous EPD [33].

Polymer binders are common additives in ceramic processing. The most common binders used in EPD are non-ionic-type polymers (polyvinyl alcohol, polyvinyl butyral, ethylcellulose, polyacrylamide, etc.) [54]. The polymer macromolecules adsorb onto the surfaces of ceramic particles. Positively charged ceramic particles provide electrophoretic transport of the polymeric molecules to form deposits on cathodic substrates. Cationic polyelectrolytes with inherent binding properties, such as PDDA or PEI, could be used for particle charging and EPD.

The application of neutral polymers to ELD presents difficulties, as the formation of ceramic particles is achieved near the electrode surface. One important finding was the feasibility of electrochemical intercalation of charged polyelectrolytes into electrolytic deposits [54]. Using cationic polyelectrolytes with inherent binding properties, problems related to cracking in electrolytic deposits could be diminished. Moreover, various organoceramic nanocomposites could be obtained using electrodeposition. The intercalation of polymers is achieved by their adsorption on the surface of colloidal particles, which are produced near the cathode and form a cathodic deposit.

The role of binders in EPD processing is multifunctional. Polymer binders are used to obtain adherent deposits and prevent cracks. In addition, the adsorbed polymer can provide steric stabilization of suspension of ceramic particles and reduce viscosity of the suspension. In EPD

processing, charged ceramic particles transport adsorbed polymer to the electrode surface, thus allowing the polymer binder to be included in the deposit. The control of polymer adsorption is of paramount importance. The amount of polymer adsorption depends on polymer concentration in suspension and specific polymer- particle, polymer- solvent, particle- solvent, and particle-dispersant interactions. Good solvents are necessary in order to achieve high polymer concentration in solution. However, the polymer can be adsorbed on the surface of ceramic particles when its solubility in the dispersion medium is low. Adsorption of polymer on ceramic particles in poor solvent can result in bridging flocculation. In contrast, good solvents are important to achieve steric stabilization. Polymer stabilizing moieties, which extend out from the particle surface must be well solvated in a good solvent. Therefore, for EPD, it could be advantageous to use copolymers of a block or graft type. Indeed, soluble polymers serve to anchor copolymer molecules to the particle surface, whereas chains of soluble polymers enable steric stabilization.

Metal alkoxides and hydroxides have also been used as binder materials [30, 61]. EPD of phosphor particles was performed from a bath containing  $\text{Mg}(\text{NO}_3)_2$ . Metal alkoxides or hydroxides formed on the cathode during deposition and acted as cementing materials to hold the deposit. The type of binder material formed is dependent on the amount of water in the deposition bath [30]. These results show that EPD and ELD could be combined to form advanced deposits.

### 2.2.1.8 Kinetics of electrophoretic deposition

It is very important to control the deposit rate during EPD. It will allow us to control the thickness of the deposited layer. The rate is also important for controlling the compositional profile of functionally graded materials [62]. Since the EPD was established, the kinetics of electrophoretic deposition has been the subject of numerous investigations. The first model of EPD kinetics was proposed by Hamaker in 1940 for electrophoretic cells with planar geometry. He observed that deposits weight ( $m$ ) is proportional to the concentration ( $C_s$ ) of the suspension, time ( $t$ ) of deposition, surface area ( $S$ ) of the deposit, and electric field ( $E$ ):

$$m = C_s \mu S E t \quad (2 - 10)$$

Where  $m$  (g) is deposit mass per unit area;  $C_s$  ( $\text{g cm}^{-3}$ ) is suspension concentration;  $\mu$  ( $\text{cm}^2 \text{s}^{-1} \text{V}^{-1}$ ) is electrophoretic mobility;  $S$  ( $\text{cm}^2$ ) is deposition area;  $E$  ( $\text{V cm}^{-1}$ ) is electric field;  $t$  (s) is time.

However, there are some limitations in this equation: to get a linear relationship between deposited mass and time, the parameters in Eq(2-10) must stay unchanged with time. This will limit the application of Hamaker expression only to short deposition times. At this point, more corrections are needed.

In 1996, Sarkar and Nicholson [36] firstly introduce an efficiency factor  $f \leq 1$  (i.e. if all the particles reaching the electrode take part of deposition  $f = 1$ ) to quantify the effect of the undermined process of deposition. It is expected that a colloidally stable suspension, i.e., particles with high zeta potential, have  $f \approx 1$ . Moreover, they also take the variation of particle concentration

with time into consideration. Referring the Hamaker equation Eq (2-10), they concluded a new expression on the EPD kinetics:

$$\frac{dm}{dt} = f\mu SEC(t) \quad (2-11)$$

In the early stages of the process the variation of bulk solid concentration in the suspension is negligible, since only a minor fraction of the powder is being deposited. But for long time, the amount of powder extracted from the bulk suspension becomes significant, and consequently  $C_s$  decreases. Then the  $C(t)$  can be expressed by:

$$C(t) = \frac{m_0 - m(t)}{V} \quad (2-12)$$

Where the  $m_0$  is the initial mass of powder in the suspension,  $V$  is the volume of suspension considered constant.

If it is assumed that the suspension is homogeneous and that there is no decrease of particle concentration due to sedimentation or any other process, i.e., the only change of concentration is due to EPD. In this case, at initial time  $t = 0$ , the deposited mass  $m(0) = 0$ . At  $t=t$ , the  $m(t)$  can be deducted by combining Eq. (2-11) and Eq. (2-12):

$$m(t) = m_0(1 - e^{-kt}) \quad (2-13)$$

Where  $k$  is defined as “kinetic parameter”:

$$k = \frac{SfE\mu}{V} \quad (2-14)$$

The Eq. (2-13) for EPD kinetics has been widely applied by Sarkar and Nicholson[36]. Eq. (2-13) can be reduced to the Hamaker model for short times. This equation is widely accepted in the literature .In recent years several authors have proposed different mathematical models based on this equation to describe the deep electrophoretic penetration and deposition of ceramics in porous substrates, to determine deposit thickness, or to control the homogeneity of the porous distribution in a ceramic membrane [63].

In constant-voltage EPD, the potential difference between the electrodes is maintained constant, but, because deposition requires a steeper potential gradient than electrophoresis, then, with increasing deposition (and therefore, increasing electrical resistance), the potential inducing electrophoresis (E, voltage drop/unit distance in the suspension) decrease and particle motion decrease, particle deposition rate even become zero if the gradient of the E is too flat. As the deposit forms, it replaces an equal thickness of suspension, and the total resistance of the system changes. This total resistance should consist of the resistance of deposit plus suspension. Then, the electric field strength applied to the suspension can be considered to be:

$$E = \frac{\Delta U}{L + L_{dep} \left( \frac{R_s}{R_d} - 1 \right)} \quad (2 - 15)$$

Where  $\Delta U$  (V) is the potential drop between the electrodes; L (cm) is the distance between electrodes;  $L_{dep}$ (cm) is the deposit thickness;  $R_s$  ( $\Omega$  cm) is the resistivity of the suspension;  $R_d$  ( $\Omega$  cm) is the resistivity of the deposit. The deposit thickness can be related to the weight of the deposit:

$$L_{dep} = \frac{V_d}{S} = \frac{m(t)/C_d}{S} \quad (2-16)$$

Where  $V_d$  ( $\text{cm}^3$ ) is the deposit volume;  $C_d$  ( $\text{g cm}^{-3}$ ) is the deposit concentration (deposit density).

Combine Eq. (2-15) and Eq. (2-16) gives:

$$E = \frac{\Delta U}{L + R'm(t)} \quad (2-17)$$

Where  $R'$  is a constant, the value of which is given by:

$$R' = \frac{\frac{R_s}{R_d} - 1}{C_d S} \quad (2-18)$$

Take the concentration change into consideration the modified the equation is:

$$\int dm = f \iint dS \mu E(t) C(t) dt \quad (2-19)$$

Combine Eq. (2-15), Eq. (2-16) and Eq. (2-19) the deposition equation comes:

$$R'm(t) + (R'm_0 + L) \ln\left(\frac{m_0 - m(t)}{m_0}\right) + k'\Delta U t = 0 \quad (2-20)$$

Where the  $k'$  is a redefined "kinetics parameter":

$$k' = \frac{f s \mu}{V} \quad (2-21)$$

The Eq. (2-20) is suitable for Constant-voltage EDP also a general kinetics expression for considering electric field and solid loading (concentration of suspension) variation.

## 2.2.2 Chemical techniques

Variety chemical methods are widely used for the fabrication of functional nanocomposites.

Several advanced means have been used in my experiments as following:

### 2.2.2.1 Chemical Reduction

The chemical reduction techniques, using a variety of organic and inorganic reducing agents, are widely applied in synthesis of nanoparticles. The most common approach for synthesis of silver NPs is chemical reduction. In general, different reducing agents such as sodium citrate, ascorbate, sodium borohydride ( $\text{NaBH}_4$ ), elemental hydrogen, polyol process, Tollens reagent, N, N-dimethylformamide (DMF), and poly (ethylene glycol)-block copolymers are used for reduction of silver ions ( $\text{Ag}^+$ ) in aqueous or non-aqueous solutions. These reducing agents reduce  $\text{Ag}^+$  and lead to the formation of metallic silver ( $\text{Ag}^0$ ), which is followed by agglomeration into oligomeric clusters. These clusters eventually lead to the formation of metallic colloidal silver particles [64-66].

However, most of these experiments are still in development stage and the experienced problems are the stability and aggregation of NPs, control of crystal growth, morphology, size and size distribution. Furthermore, extraction and purification of produced NPs for further applications are still important issues [67, 68].

### **2.2.2.2 Chemical Polymerization**

Chemical polymerization is a process of reacting monomer molecules together in a chemical reaction to form polymer chains or three-dimensional networks [69]. Polypyrrole (PPy), which is widely used in electrochemical supercapacitors devices [70-72], is a type of organic conducting polymer commonly synthesized by chemical polymerization from pyrrole. In the chemical synthesis process, chemical oxidants will be involved[73]. It has the advantages that easy for mass production, high material loading of electrode, and options to modify conducting polymers backbone covalently, which make the chemical polymerization promising in industrial production.

Typical processes for chemical polymerization of CP powders include emulsion polymerization, layer-by-layer assembly and solution polymerization. For example, Q.Wang [74][used ultrasonically initiated in-situ emulsion polymerization of n-butyl acrylate (BA) and methyl methacrylate (MMA) and prepared CP-encapsulated CNT. During the chemical polymerization synthesis process of PPy, the solvent, temperature, dopant [75], as well as the nature of oxidant[76] greatly affects the morphology and electrochemical properties of PPy in the chemical synthesis .

## Chapter 3 Objectives

The long term objective of this work is the development of new electrochemical and chemical methods for the fabrication of functional nanocomposites.

The long term objective is based on the short term objectives:

- Development of advanced dispersing agents with chelating properties and strong adsorption on inorganic particles and organic materials. Application of the dispersing agents for the synthesis of nanoparticles and electrophoretic deposition, investigation of new dispersant adsorption and dispersion mechanisms. Development of liquid-liquid extraction methods for the synthesis of nanoparticles using new dispersants.
- Development of electrophoretic deposition methods for the deposition of new polymers and composites, investigation of microstructure and properties of the composite materials, such as corrosion protection, flame retardant and energy storage properties.
- Development of new combined electrochemical methods for the synthesis of organic-inorganic nanocomposites using electrophoretic deposition of strong polyelectrolytes and electrosynthesis or electrophoretic deposition of inorganic particles.
- Development of advanced dispersants for fabrication of novel organic-inorganic composites and polymer-carbon nanotube composites by chemical methods. Analysis of microstructure and properties of new composite materials.

## Chapter 4 Experimental Procedures

### 4.1 Materials

All starting materials involved in my research were listed in the following Table 4-1:

**Table 4-1 Materials purchased from commercial suppliers.**

Category	Material	Supplier
Minerals	Huntite ( $\text{Mg}_3\text{Ca}(\text{CO}_3)_4$ )	Sibelco
	Hydrotalcite ( $\text{Mg}_6\text{Al}_2\text{CO}_3(\text{OH})_{16}\cdot 4(\text{H}_2\text{O})$ )	Sigma-Aldrich
	Aluminum hydroxide ( $\text{Al}(\text{OH})_3$ )	Sigma-Aldrich
	Zirconium Sillicate ( $\text{ZrSiO}_4$ )	Shandong Golden sun Zirconium Industry Co.,  China
	Silicon carbide ( $\text{SiC}$ )	IbidenCo., Japan
Oxides	Zinc Oxide ( $\text{ZnO}$ )	Sigma-Aldrich
	Titanium dioxide ( $\text{TiO}_2$ )	Sigma-Aldrich

	Nickel Oxide (NiO)	Sigma-Aldrich
	$Al_2TiO_5$	Alfa-Aesar, USA
	$MgAl_2O_4$	Cerac, USA
<b>Nitrides</b>	Boron Nitride (BN)	Sigma-Aldrich
	Silver Nitrate ( $AgNO_3$ )	Sigma-Aldrich
	Silicon nitride( $Si_3N_4$ )	H.C. Starck, Germany
<b>Dispersing/charging agent</b>	Sodium Alginate	Sigma-Aldrich
	Poly[1-[4-(3-carboxy-4-hydroxyphenylazo) benzenesulfonamido]-1,2-ethanediyl, sodium salt] (PAZO)	Sigma-Aldrich
	Caffeic acid (CA)	Sigma-Aldrich
	Lauryl gallate (LG)	Sigma-Aldrich
	Tannic acid (TA)	Sigma-Aldrich
	Poly(vinylbenzyl trimethylammonium chloride) (PVT)	Scientific Polymer Products, Inc

	Hydroxyethyl cellulose ethoxylate, quaternized (HCE)	Sigma-Aldrich
	2, 2'-Biquinoline-4,4'-dicarboxylic acid dipotassium salt trihydrate	Sigma-Aldrich
	Poly(styrene-alt-maleic acid) sodium salt solution	Sigma-Aldrich
	Poly(4-styrenesulfonic acid-co-maleic acid) sodium salt solution	Sigma-Aldrich
	Poly(4-styrenesulfonic acid-co-maleic acid) sodium salt	Sigma-Aldrich
<b>Metal</b>	Palladium (Pd)	Sigma-Aldrich
<b>Conductive carbon materials</b>	Multiwalled carbon nanotubes (MWCNTs)	Bayer Inc.  (Germany)
<b>Monomer for the polypyrrole (PPy)</b>	Pyrrrole (>98%)	Sigma-Aldrich
<b>Oxidant for the synthesis</b>	Ammonium peroxydisulfate (APS)	Sigma-Aldrich
<b>Electrolyte for ES</b>	Sodium sulfate (Na <sub>2</sub> SO <sub>4</sub> )	Sigma-Aldrich

<b>Other Chemicals</b>	Sodium hydroxide (NaOH)	Sigma Aldrich
	Zinc acetate dihydrate ( $\text{Zn}(\text{CH}_3\text{COO})_2 \cdot 2\text{H}_2\text{O}$ )	Sigma-Aldrich
	Zirconyl chloride octahydrate ( $\text{ZrOCl}_2 \cdot 8\text{H}_2\text{O}$ )	Fluka Chemical Corp
<b>Current collector</b>	316L stainless steel foils	Alfa Aesar
	Nickel foam (porosity ~95%)	Vale

## 4.2 Materials Synthesis

### 4.2.1 Hydrothermal synthesis of ZnO nanorods

For the synthesis of ZnO nanorods, as shown in Fig.4-1, 10mL of 0.1 M of zinc acetate solution in ethanol was mixed with 20 mL solution of 0.5 M NaOH in ethanol, containing 0.003 M reducing agent or without reducing agent. The mixed solution was stirred for 10 min and then transferred to a Teflon-lined stainless steel autoclave and heated at 150 °C for 24 hours. The obtained powder was washed by deionised water and ethanol and then dried at 60 °C for 12 h [77].

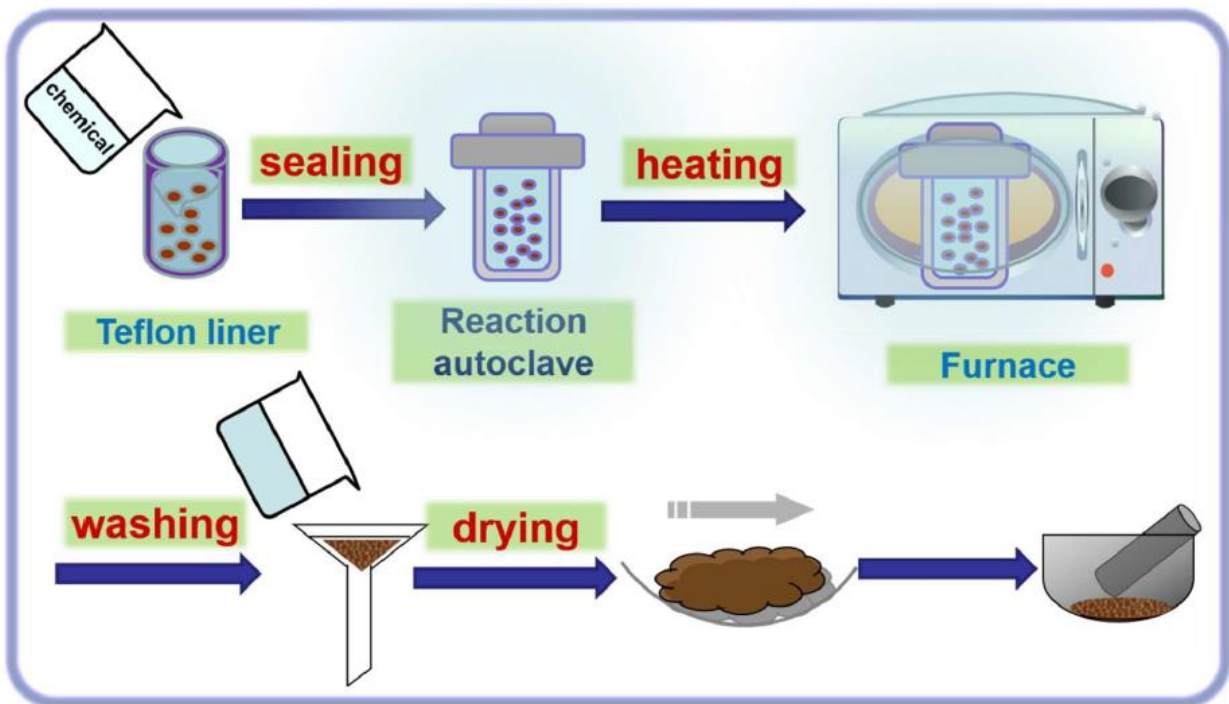


Figure 4-1 Hydrothermal process for producing ZnO nanorods.

## 4.2.2 Chemical polymerization of PPy and PPy-MWCNTs

PPy chemical polymerization was based on chemical reaction between Py monomer and APS oxidant. For the fabrication of PPy powder (see Fig.(4-1(a)), 0.2M Py monomer solution in deionized water was mixed with different dopants (Py: dopant mass ratio 10: 1.). The solution was cooled down to 4 °C by an ice-water bath and magnetic stirring was performed for 2 hrs. The PPy precipitation was obtained by adding APS solution (0.2 M in final solution) to the above solution. The resultant mixture was subsequently allowed to react for 20 hrs. PPy precipitates were filtered and thoroughly washed with deionized water, and then dried at 60 °C for 24 hrs in air. The final materials were grinded into fine powders and dried.

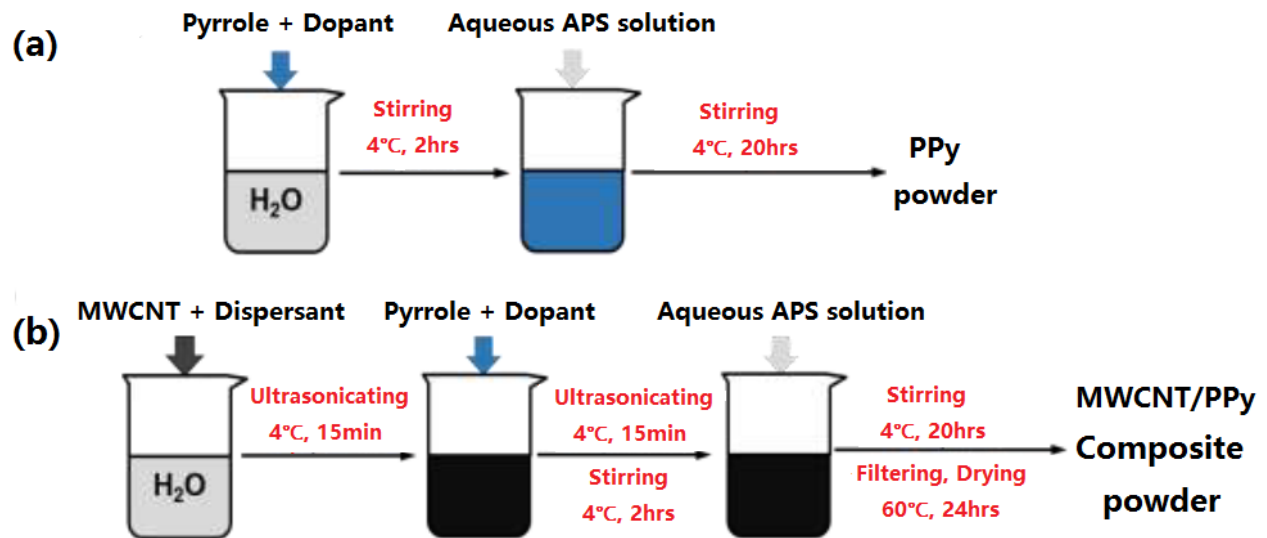
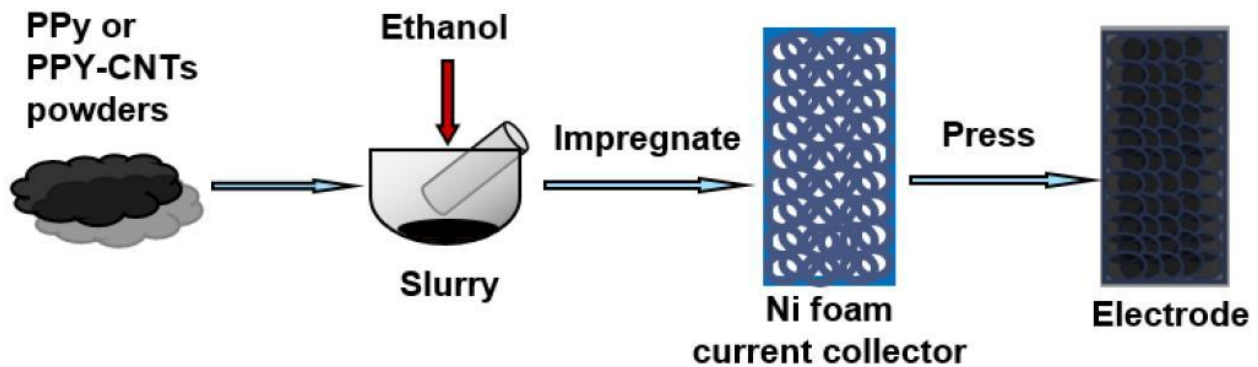


Figure 4-2 Chemical synthesis of (a) PPy powder and (b) MWCNT/PPy composite materials.

A similar procedure was used for the fabrication of PPy-MWCNT composite (see Fig.4-2(b)). In this procedure, the dopant for PPy was also used as dispersant for MWCNTs. Stable MWCNT suspension, containing a dopant, was prepared and added to the solution of Py monomer (0.2 M in final solution) in order to obtain composites with a PPy: MWCNT mass ratio of 4: 1. Ultrasonic agitation was used prior to the addition of APS in order to achieve homogeneous dispersion of MWCNTs. The PPy and composite PPy - MWCNT powders were washed completely with deionized water and dried in air at 60 °C for 24 h.

### 4.3 Fabrication of electrodes for electrochemical tests



**Figure 4-3 Fabrication of electrodes for electrochemical cells.**

The obtained PPy or PPy-MWCNTs powders were used for the fabrication of slurries, which were impregnated into current collectors to form electrodes (Fig.4-3). The procedure started

with the powder grinding in ethanol to make slurry. The obtained slurry was then impregnated into Ni foam current collector (95% volume porosity) with area of  $1 \times 1 \text{ cm}^2$ . The materials loading varied from 10 to  $30 \text{ mg cm}^{-2}$ . After drying in air at  $60 \text{ }^\circ\text{C}$ , the electrode was pressed to 30% of original thickness to enhance the contact between electrode materials and current collectors (Fig.4-3).

#### 4.4 Electrodeposition and adhesion test

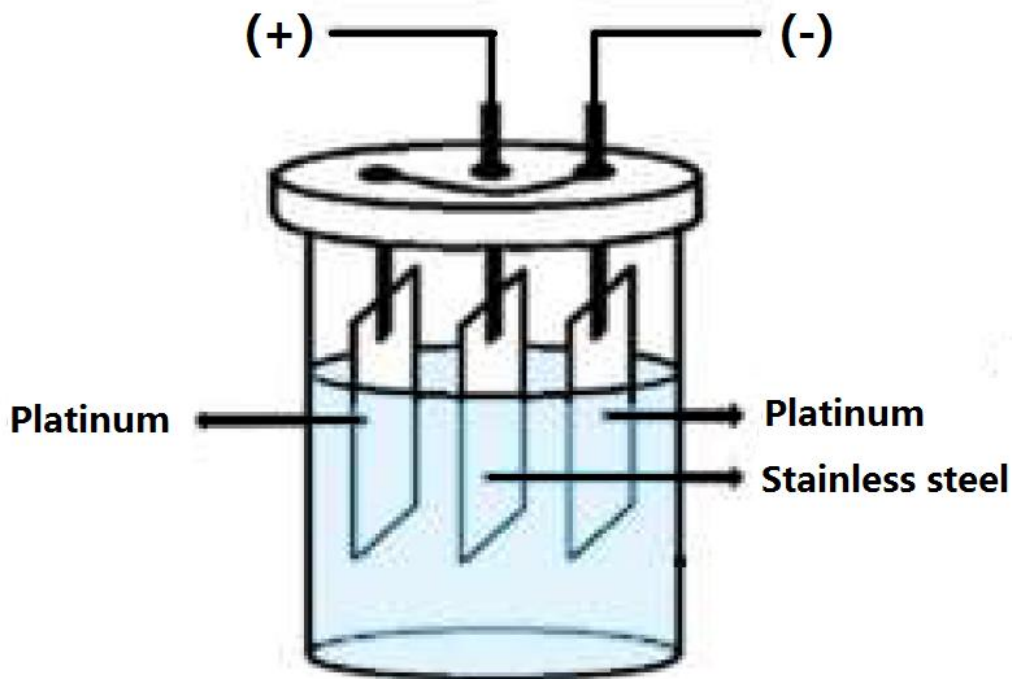


Figure 4-4 A schematic of the setup of the deposition cell.

A schematic of the setup of the electrochemical cell for deposition is shown in Fig.4-4. The cell included a stainless steel foil ( $25 \times 50 \times 0.1$  mm), used as substrate, centered between two parallel platinum (Pt) counter electrodes. The distance between the substrate and counter electrodes was 15 mm. The deposition voltage was varied in the range of 5–100 V. The deposition time was varied in the range of 0.5–10 min. An electrophoresis power supply EPS 601 (Amersham Biosciences) was employed to provide the DC electric field for electrodeposition, either in a constant current density (galvanostatic) or a constant voltage mode. All the films were prepared using fresh suspension. The films obtained were dried in air at room temperature for at least 24 hours before the further characterization. The deposition yield was studied for the films deposited on stainless steel substrates. In all experiments, the Mettler Toledo AX105 DeltaRange analytical balance was used. The accuracy of balance is 0.01 mg. A minimum of three samples were prepared in each deposition experiment. The deposition yield measurements were repeatable, and the error was less than 5%.

The adhesion of deposited films was characterized according to the ASTM D3359 standard. To start with, six cuts with 1mm apart were required in the x and y direction on the film. Pressure-sensitive tape (Elcometer 1539) was applied over the cutting area and then removed. Adhesion was evaluated by the comparison between different patterns on the tapes. The adhesion classification was performed using a table (ASTM D3359) shown in Fig.4 -5.

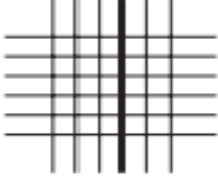
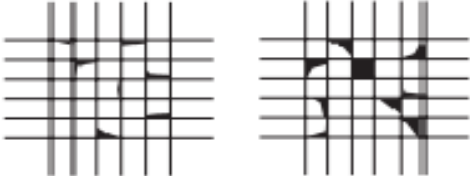
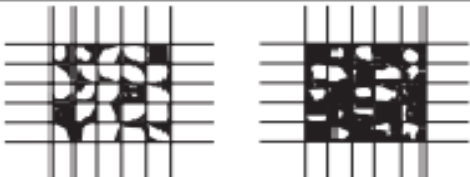
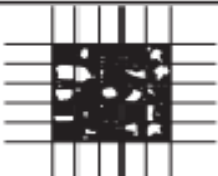
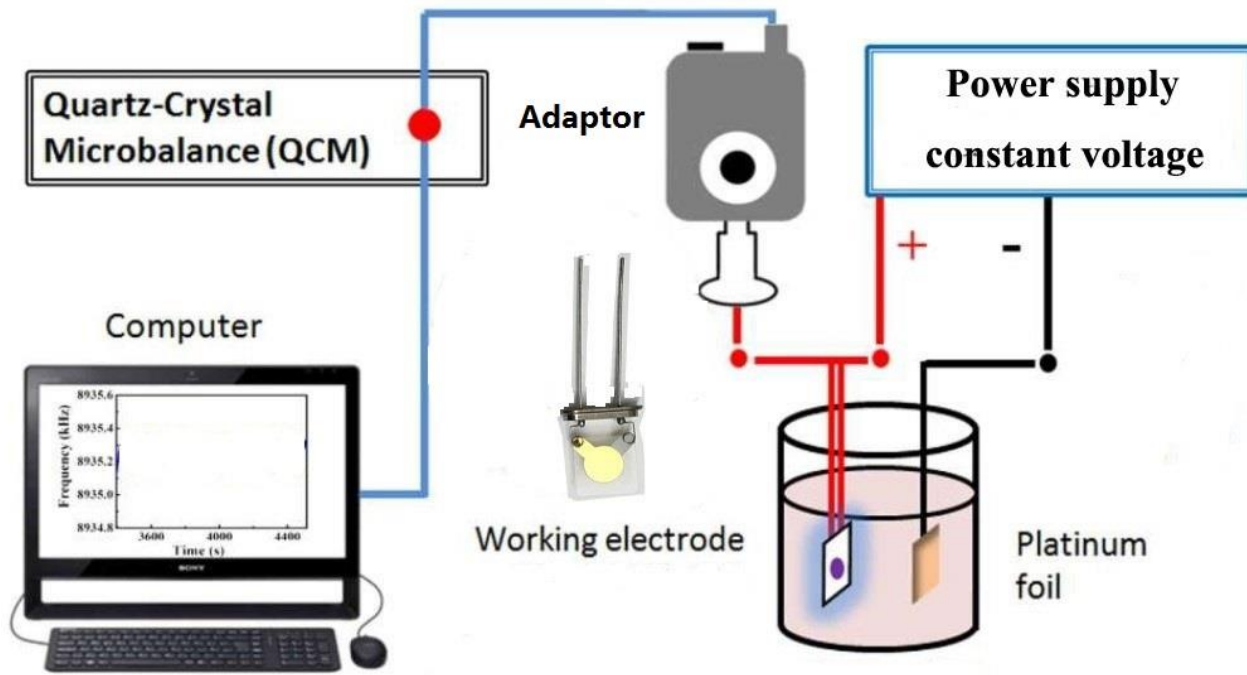
<b>Classification of Results</b>	
Classification for percentage of area removed	Surface of crosscut area (six each horizontal and vertical parallel cuts) where flaking has occurred: adhesion range by percent.*
<b>5B</b> – 0% None	
<b>4B</b> – Less than 5%	
<b>3B</b> – 5% to 15%	
<b>2B</b> – 15% to 35%	
<b>1B</b> – 35% to 65%	
<b>0B</b> – Greater than 65%	

Figure 4-5 Classification of adhesion test results.

## 4.5 In-situ deposition yield study

The deposition kinetics has been investigated in-situ using a quartz crystal microbalance. (QCM 922, Princeton Applied Research) controlled by a computer (Fig4-6) .



**Figure 4-6 A schematic of QCM analysis system.**

The electrochemical cell included an Au coated 9-MHz quartz resonator working electrode, a Pt wire counter electrode and dilute testing solutions. The resonators with an area of  $0.2 \text{ cm}^2$  were coated with active material from dilute solutions. The QCM studies of deposition yield were performed at a constant voltage 5V. A sourcemeter (Keithley model 2400) was used as a power supply for QCM studies. The deposit mass  $\Delta m$  was calculated using Sauerbrey's equation [78, 79] (Eq(4-1)):

$$-\Delta F = \frac{2F_0^2}{A\sqrt{\rho_q\mu_q}} \times \Delta m \quad (4 - 1)$$

Where  $\Delta F$  is the frequency decrease of the QCM,  $F_0$  is the parent frequency of QCM (9 MHz),  $A$  is the area of the gold electrode ( $0.2 \text{ cm}^2$ ),  $\rho_q$  is the density of quartz ( $2.65 \text{ g cm}^{-3}$ ) and  $\mu_q$  is the shear modulus of quartz ( $2.95 \times 10^{11} \text{ dyne cm}^{-2}$ ).

## **4.6 Materials characterization methods**

### **4.6.1 X-ray diffraction analysis**

X-ray diffractometry (XRD) is commonly used to determine the phase content in minerals and materials. It is also a very useful tool for the measurement of lattice parameters, internal stresses, crystal size, and crystal orientation etc. In my experiments, the phase content of the deposits was determined by XRD with a diffractometer (Nicolet I2), using monochromatized Cu Ka radiation at a scanning speed of  $0.5 \text{ }^\circ/\text{min}$ .

### **4.6.2 FTIR and UV-Vis spectroscopy**

The adsorption of dispersants was studied by Fourier transform infrared spectroscopy (FTIR) and UV-Vis spectroscopy tests. The deposits were removed from the substrates after drying in air for 72 h for the investigations. FTIR tests were performed using Bio-Rad FTS-40 instrument. The UV-Vis spectra were obtained using Cary-50 UV-Vis spectrophotometer.

### **4.6.3 Scanning and transmission electron microscopy**

The surface morphology and microstructures of the deposited coatings were studied by scanning electron microscopy (SEM) using a JEOL JSM-7000F scanning electron microscope. The transmission electron microscopy (TEM) investigations were performed using a Philips CM12 microscope and a JEOL 2010 FEG high-resolution transmission electron microscope.

### **4.6.4 Thermogravimetric and differential thermal analysis**

Thermogravimetric analysis (TG) is an analytical technique used to determine a material's thermal stability and its fraction of volatile components by monitoring the weight change that occurs as a specimen is heated. The measurement is normally carried out in air or in an inert atmosphere, and the weight is recorded as a function of increasing temperature. In addition to weight changes, some instruments also record the temperature difference between the specimen and one or more reference pans (differential thermal analysis, DTA), which can be used to monitor the energy released or absorbed via chemical reactions or phase transformations during the heating process. In my experiments, TG and DTA were carried out using the deposits that had been scraped from the Pt electrode after deposition and dried at room temperature for 24 hr. The thermoanalyzer (Netzsch STA-409) was operated in air between room temperature and 1200 °C at a heating rate of 5 °C/min.

## 4.7 Electrochemical Tests

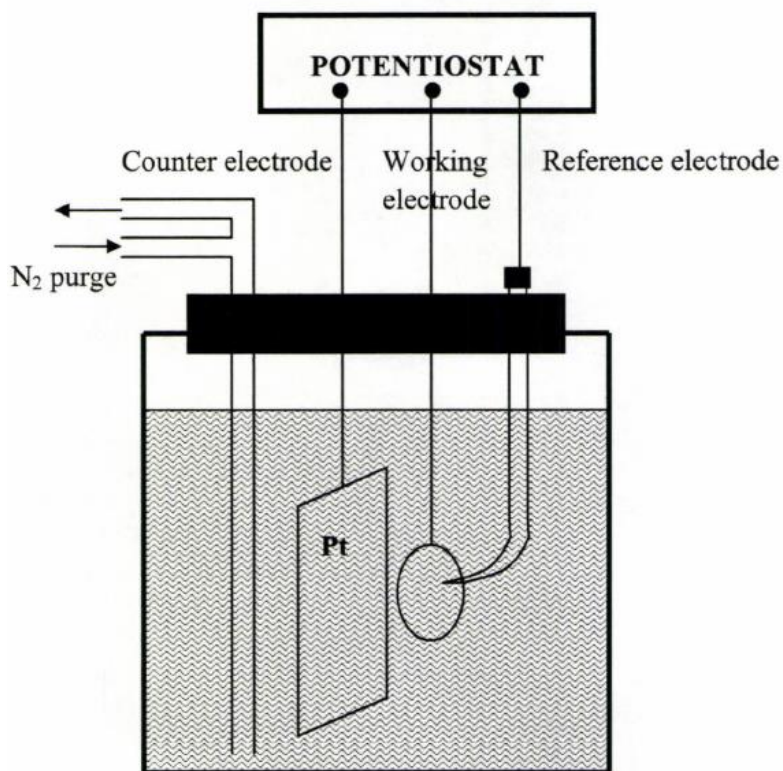


**Figure 4-7** A schematic of a standard three electrode electrochemical cell.

The electrochemical behaviors of the test electrodes were investigated using Potentiostat (PATSTAT 2273, Princeton Applied Research), controlled by a computer using the PowerSuite electrochemical software package. Electrochemical investigations of the single electrodes were carried out using a standard three electrode electrochemical cell (shown in Fig.4-7), with 0.5 M

sodium sulfate aqueous solution as electrolyte (deaerated by 99.995% nitrogen gas flow before and during test), platinum gauze as counter electrode and a standard calomel electrode (SCE) as reference electrode.

### 4.7.1 Cyclic voltammetry study

Cyclic voltammetry (CV) studies were performed within a potential range of -0.5 to +0.4 V versus SCE at scan rates of 2-100 mV s<sup>-1</sup> in 0.5M Na<sub>2</sub>SO<sub>4</sub> aqueous solutions. The total capacitance was calculated using the following expression (Eq.4-2):

$$C = \frac{Q}{\Delta V} \quad (4 - 2)$$

Where Q is charge obtained by half the integrated area of the CV curve and  $\Delta V$  is the width of the potential window. The mass normalized specific capacitance  $C_m=C/m$  (m-sample mass) and area-normalized specific capacitance  $C_s=C/S$  (S-geometric sample area), calculated from the CV data, were investigated versus mass loading, scan rate and cycle number.

### 4.7.2 Impedance spectroscopy study

The measurement of complex electrochemical impedance was conducted within a frequency range of 10 mHz to 100 kHz with AC signal amplitude of 5 mV in 0.1 or 0.5 M Na<sub>2</sub>SO<sub>4</sub> aqueous solutions. The obtained complex impedance data (Eq.4-3) plotted in Nyquist graph was

simulated using ZSimpWin software (Princeton Applied Research) and appropriate equivalent circuit was selected and applied to such simulation[80].

$$Z^* = Z' - iZ'' \quad (4 - 3)$$

The area normalized complex AC capacitance (Eq.4-4) was calculated[80] from the complex impedance data using Eq.4-5 and Eq.4-6, where  $\omega=2\pi f$  (f-frequency). The relaxation times (Eq.4-7) were calculated from the relaxation frequencies  $f_m$ , corresponding to the  $C_s''$  maxima.

$$C_s^* = C_s' - iC_s'' \quad (4 - 4)$$

$$C_s' = \frac{Z''}{\omega S Z^2} \quad (4 - 5)$$

$$C_s'' = \frac{Z'}{\omega S Z^2} \quad (4 - 6)$$

$$\tau = \frac{1}{f_m} \quad (4 - 7)$$

### 4.7.3 Corrosion study – Tafel plot

The Tafel technique provides a fast way of determining the corrosion rate of a specimen. In a typical experiment, a controlled-potential scan was programmed to take place within  $\pm 250$  mV of the corrosion potential of the specimen. The resulting current is logarithmically plotted versus the potential (log current versus potential). The corrosion rate can be calculated from the Tafel plot

data. In this study, the Tafel plots were obtained with a scan rate of 1 mV /s and the electrolyte was 3 wt% NaCl. The corrosion rate is calculated using Eq.4-8:

$$\text{Corrosion Rate (mpy)} = \frac{0.13 I_{\text{corr}}(\text{E.W.})}{d} \quad (4 - 8)$$

E.W. is the equivalent weight of the corroding species (g). Density of the corroding species ( $\text{g}/\text{cm}^3$ ) is d.  $I_{\text{corr}}$  is the corrosion current density ( $\mu\text{A}/\text{cm}^2$ ).

## **Chapter 5 Results and Discussions**

### **5.1 Development of chelating dispersant**

Electrophoretic deposition (EPD) is a colloidal technique for the deposition of ceramics, polymers and composites[36, 47]. One of the major issues in the development of EPD technology is the selection of dispersants. The particles must be well dispersed and charged in the suspensions. Recent studies highlighted the importance of strong dispersant adsorption on the particle surface[81]. Dispersants with chelating ligands, such as anionic and cationic molecules from the catechol, salicylic acid and gallic acid families [81] showed improved adsorption on oxide particles. The adsorption mechanisms involved complexation of metal atoms on the particle surfaces with chelating ligands of the molecules.

#### **5.1.1 Chelating molecules**

##### **5.1.1.1 Using Caffeic acid as a capping agent for synthesis and dispersant for EPD**

The surface modification of materials using molecules of the catechol family is emerging as a new area of technological and scientific interest[82]. Special attention to the adsorption of catecholates on inorganic particles resulted from the fundamental investigations of proteins, containing monomers with catechol ligands, which allowed for strong mussel adhesion to various

surfaces[83-85].It was found that such protein macromolecules contain catecholic amino acid, L-3,4-dihydroxyphenylalanine (DOPA), which interacts strongly with metal atoms on the particle surface[84].

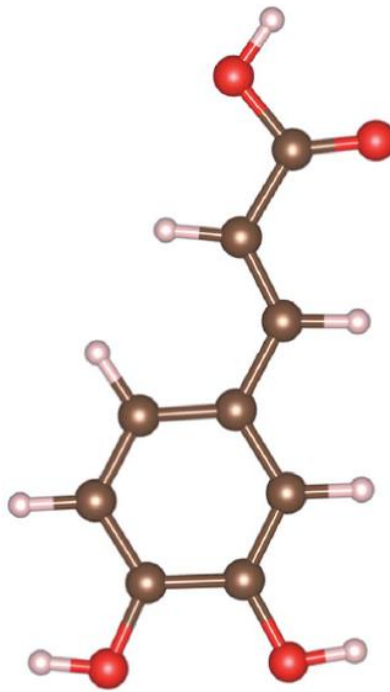


**Figure 5-1 Chemical structure of CA.**

Caffeic acid (CA) is the closest molecular analogue of DOPA (Fig.5-1). Similar to DOPA, the structure of CA contains a catechol ligand. The use of DOPA for colloidal processing of inorganic materials presents difficulties due to zwitterionic properties of this molecule, containing anionic carboxylic group and cationic amino group. In contrast, the structure of CA includes only anionic carboxylic group, which can impart a negative charge for the electrostatic dispersion of

particles, containing adsorbed CA. The adsorption of catecholates on ZnO is of particular interest for the development of sensors, photovoltaic and optical devices.

The goal of this investigation was the analysis of CA adsorption on wurtzite ZnO particles by different experimental methods. The important finding was the possibility of the fabrication of ZnO nanorods with reduced particle size and increased aspect ratio using CA as a dispersant. Moreover, the adsorbed CA allowed for the EPD of ZnO films from stable suspensions. The results of this investigation pave the way for the application of CA and other catecholates for the synthesis of nanoparticles and deposition of thin films.

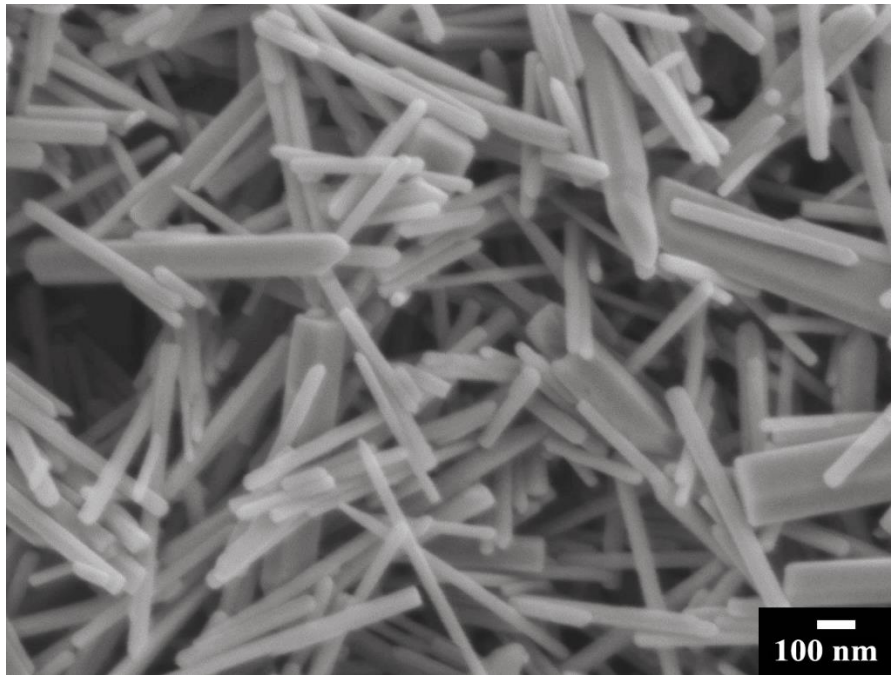


**Figure 5-2 SEM image of ZnO nanorods, prepared by the hydrothermal synthesis method.**

Fig.5-2 shows SEM image of rod-like particles, which were prepared by the hydrothermal method. The TEM images of the particles are shown in Fig.5-3(A). The electron microscopy data indicated that the typical diameter of the rod-like particles was in the range of 50–250 nm and the length was 0.2–1.5  $\mu\text{m}$ . The size of the ZnO particles prepared in the presence of CA was significantly smaller. The TEM data presented in Fig.5-3(A and B) allowed for the comparison of the morphologies of the particles prepared without CA and in the presence of CA. The particles, prepared in the presence of CA showed a nanorod morphology with typical diameter of the nanorods in the range of 10–30 nm and length of 0.2–1  $\mu\text{m}$ . The TEM images indicate that the particles, prepared in the presence of CA have higher aspect ratio, compared to the particles, prepared without CA.

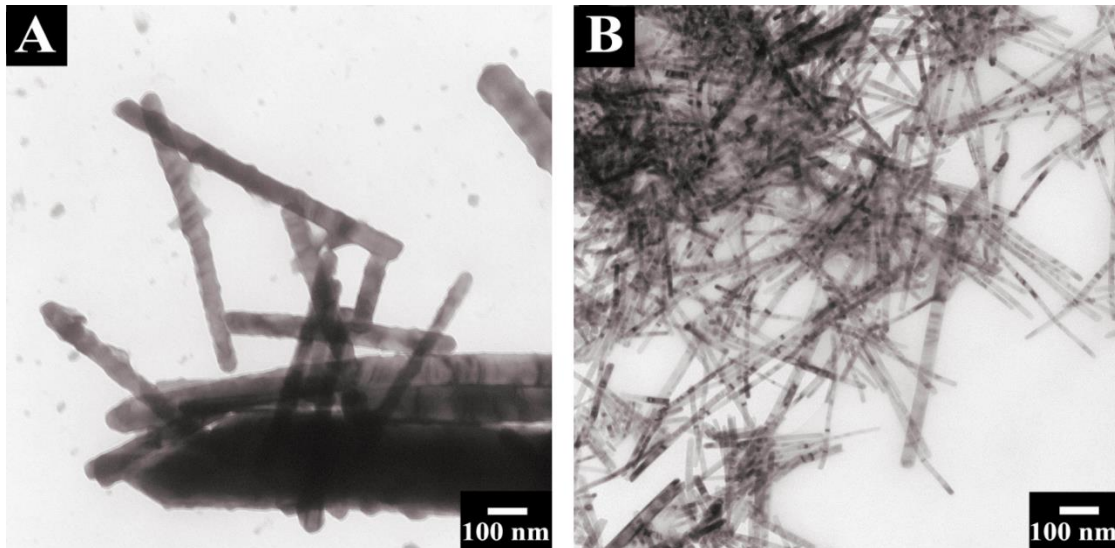


**Figure 5-3 TEM images of ZnO prepared (A) without CA and (B) in the presence of CA.**

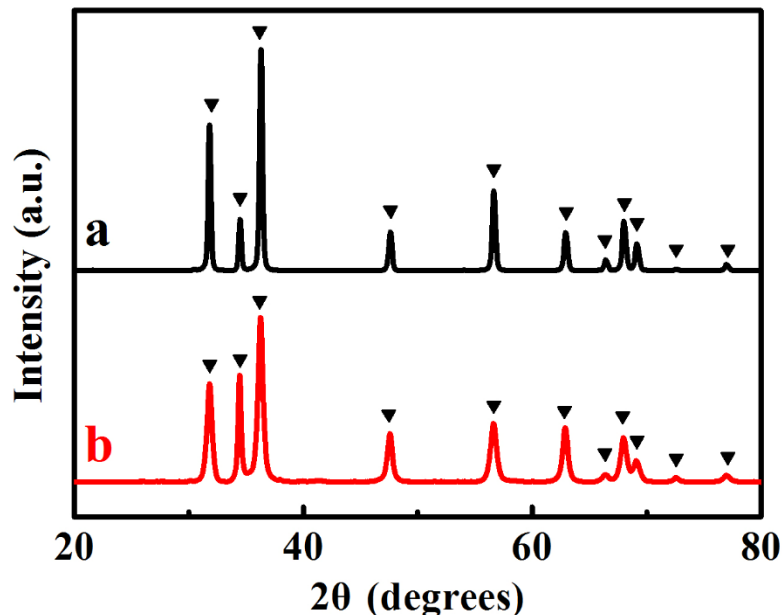


**Figure 5-4 X-ray diffraction pattern of ZnO prepared (A) without and (B) in the presence of CA ( $\blacktriangledown$  - peaks, corresponding to the JCPDS file 36-1451).**

The X-ray diffraction patterns (Fig.5-4) of the particles showed peaks of the wurtzite phase. The  $2\theta$  diffraction angles of the peaks in the diffraction pattern are in agreement with the JCPDS file 36-1451. The difference in the relative intensities of the peaks, compared to the JCPDS file 36-1451, can be attributed to the rod-like morphology of the particles[86]. The broadening of peaks for ZNO prepared in the presence of CA is related to the smaller particles size. It is suggested that the reduction in the diameter of the ZnO particles, prepared in the presence of CA is related to CA adsorption on the surface of growing ZnO particles during the hydrothermal synthesis. The adsorption of CA on the (1010) plane can inhibit the growth of the ZnO particles. As a result, the

diameter of the particles, prepared in the presence of CA, reduced significantly, compared to the diameter of the particles, prepared without CA.

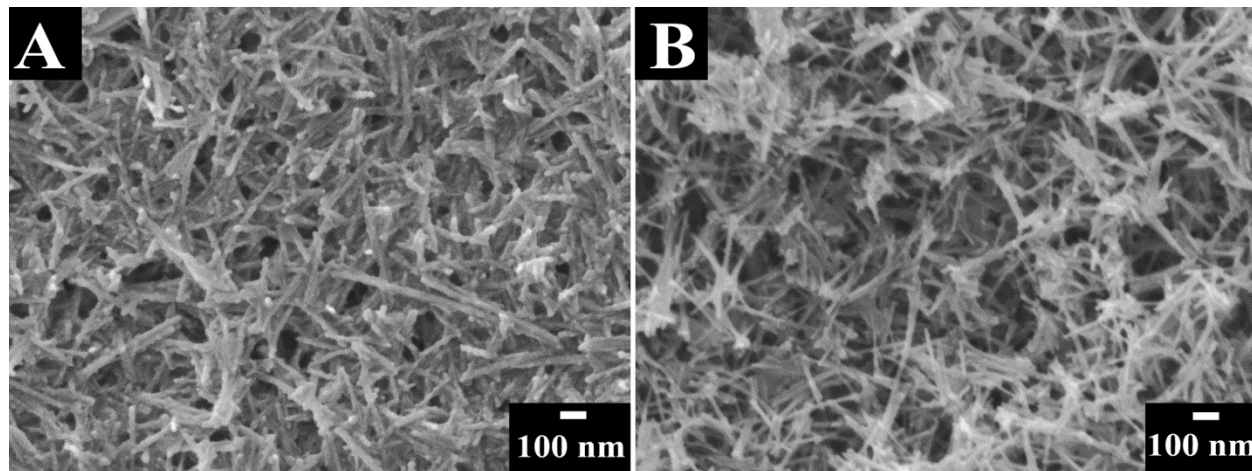


**Figure 5-5 SEM images of the films prepared by EPD at deposition voltages of (A) 30 and (B) 50 V from  $4 \text{ g L}^{-1}$  suspensions of ZnO, prepared in the presence of CA.**

The EPD experiments provided additional evidence of the CA adsorption on the ZnO particles. The ZnO suspensions, prepared without CA were unstable and showed rapid sedimentation immediately after the ultrasonic agitation. In contrast, the suspensions, prepared in the presence of CA, showed good stability for more than one week. EPD has not been achieved from the suspensions of ZnO, prepared without CA. In contrast, ZnO particles, prepared in the presence of CA, were deposited on anodic substrates by EPD. Fig.5-5 shows SEM images of ZnO films, deposited by EPD. The films contained ZnO nanorods, the dimensions of the nanorods are in agreement with the TEM data (Fig.5-3(B)). The increase in the deposition voltage resulted in increased porosity of the films (Fig.5-5(A and B)). The increased porosity can result from gas

evolution at the electrode surface. It is suggested that adsorbed CA imparted a charge to the ZnO particles and allowed for improved suspension stability and film formation by EPD.

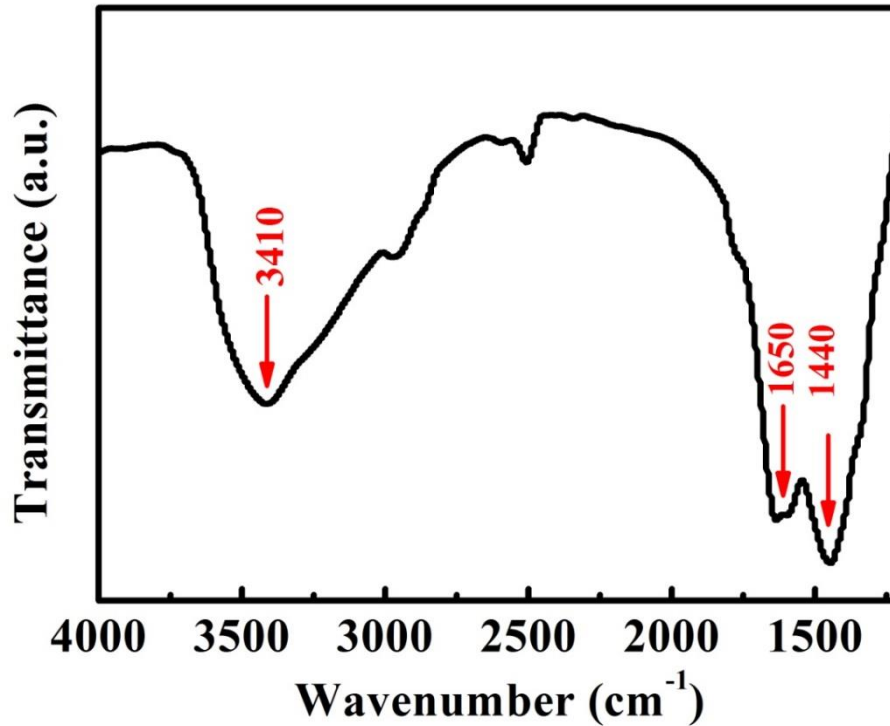


**Figure 5-6 FTIR spectra of deposit, obtained by EPD from 4 g L<sup>-1</sup> suspensions of ZnO, containing 1 g L<sup>-1</sup> CA.**

The adsorption of CA on the ZnO nanorods has also been confirmed by the results of FTIR studies of the deposited material (Fig.5-6). The absorptions at 1440 and 1650 cm<sup>-1</sup> are related to symmetric COO<sup>-</sup> stretching vibrations and C–C stretching vibrations of aromatic ring of CA[87], respectively. The broad absorption at 3410 cm<sup>-1</sup> is associated with the stretching vibration of OH groups of adsorbed water molecules[88].

The experimental results presented above show different avenues for the applications of CA adsorption in materials processing. The adsorption of CA on ZnO was confirmed by EPD experiments, electron microscopy and FTIR data. The use of CA as a dispersant for the hydrothermal synthesis of ZnO allowed for the reduced size and increased aspect ratio of the ZnO nanorods. As-prepared ZnO nanorods, containing adsorbed CA formed stable suspension due to electrosteric dispersing effect of CA. The use of CA as a dispersant allowed for the fabrication of ZnO films. The dispersants from the catechol family offer advantages for colloidal nanotechnology of oxide films due to strong adsorption of the catechol ligands. Future expansion of this work will result in the development of advanced dispersants for synthesis of nanoparticles and film formation by EPD.

### **5.1.1.2 Electrophoretic Deposition of Functional Organic Molecules (BiqCOOH) and Composite Films**

2, 2'-Bicinchoninic acid (BiqCOOH) exhibits a set of functional properties, which motivated the work of fabricating BiqCOOH films. 2,2'-Biquinoline (Biq), its derivatives and Biq-metal ion complexes are important materials for photo- and electroluminescence devices [89, 90], electro-optical displays [91, 92], solar cells [93], corrosion inhibition[92], medicine and other applications[94, 95]. It was found that BiqCOOH was capable of forming 3-D crystalline networks with various metal ions due to its unique bonding capabilities [96]. Four functional groups of BiqCOOH can act as hydrogen bond donors or acceptors in these 3-D networks with  $\pi$ - $\pi$

interactions of the BiqCOOH molecules enhancing the network ordering [96]. The ordering in the BiqCOOH based structures is enhanced by the  $\pi$ - $\pi$  interactions of the BiqCOOH molecules [96].

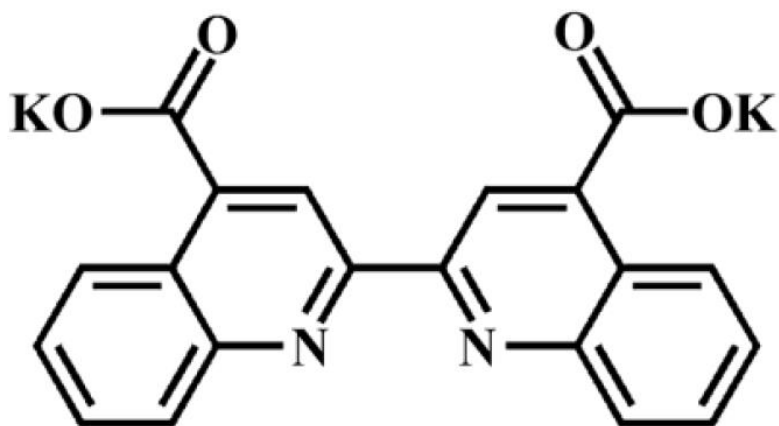


**Figure 5-7 Chemical structure of BiqCOOK molecule.**

The expanding applications of Biq and related materials generate motivation to develop new, simpler, and more robust procedures for the fabrication of films and composites. Our goal was the manufacturing of BiqCOOH films and nanocomposites. The interest in BiqCOOH is attributed to unique functional properties of this molecule, described above. Moreover, the interesting chemical structure of this molecule (Fig.5-7), which includes chelating (N containing ligands[96]) and charged (dissociation of two -COOK groups) ligands bonded to a polyaromatic backbone, makes BiqCOOH very promising for application as a dispersant for EPD. The results presented below indicate that electrochemical deposition is an effective way to achieve this goal.

This study presents a facile strategy for EPD of different materials, such as Pd metal, Ni oxide using  $\text{BiqCOO}^-$  as anionic dispersing and binding species.

In EPD process, the decomposition of water at electrodes surface will result in anodic surface pH decrease (Eq.5-1)



The protonation of the  $\text{COO}^-$  groups at the anode (Eq.5-2), the neutralization of the charge and precipitation of insoluble  $\text{BiqCOOH}$  promoted film deposition.



The SEM studies of the films prepared in a water-ethanol solvent showed separated flower-like morphology (Fig.5-8(a)). As a result, the film exhibited significant porosity. The SEM data, obtained at higher magnifications (Fig.5-8(b)) showed that flower-like assemblies contained long particles. Many individual particles were oriented nearly perpendicular to the substrate surface. The long particles deposited from the water-ethanol solvent showed nearly rectangular cross sections.

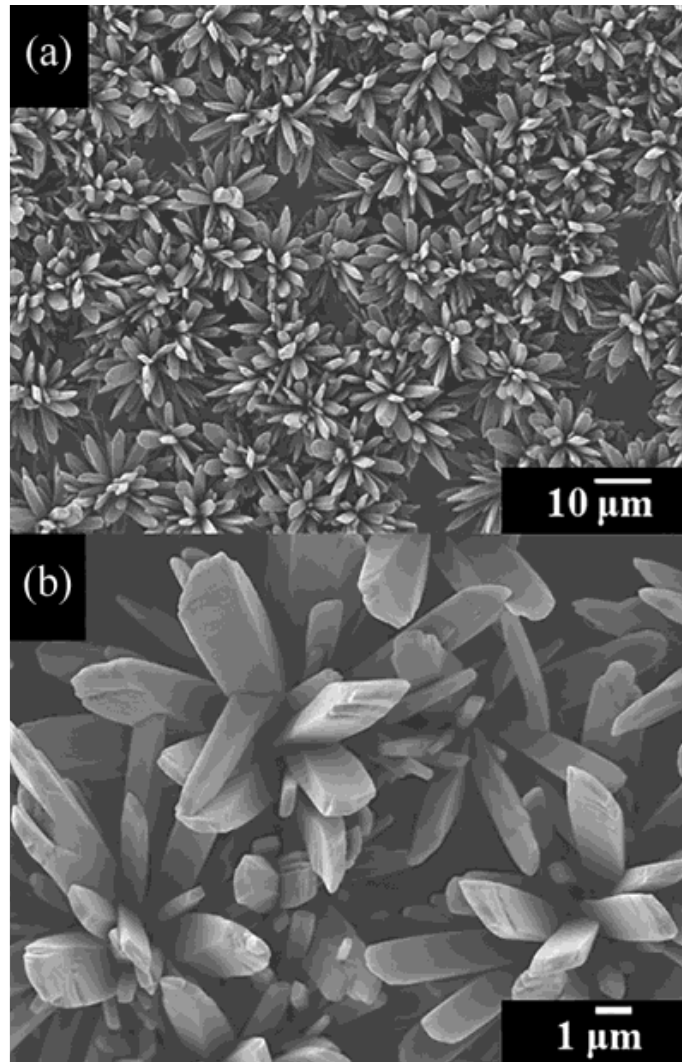


**Figure 5-8 SEM images at different magnifications for the deposit obtained from  $1 \text{ g L}^{-1}$  BiqCOOK solution in a water-ethanol solvent at a deposition voltage of 30 V.**

The film forming and chelating properties of anionic BiqCOOK allowed for the use of BiqCOOK as a dispersing and binding agent for EPD of different materials. Previous investigations [97] showed BiqCOOK adsorption on Pd particles. In our investigation Pd particles were dispersed and charged using BiqCOOK and deposited on stainless steel substrates by anodic

EPD. Fig.5-9(A) shows an SEM image of the Pd film. The SEM image indicated the formation of a porous film, containing Pd particles. BiqCOOH is clearly seen between the particles. It is suggested that BiqCOOH, adsorbed on Pd, acted as a binder for the Pd particles and promoted incorporation of Pd particles into the growing film. The binding mechanism involved complex formation between Pd and BiqCOOH.

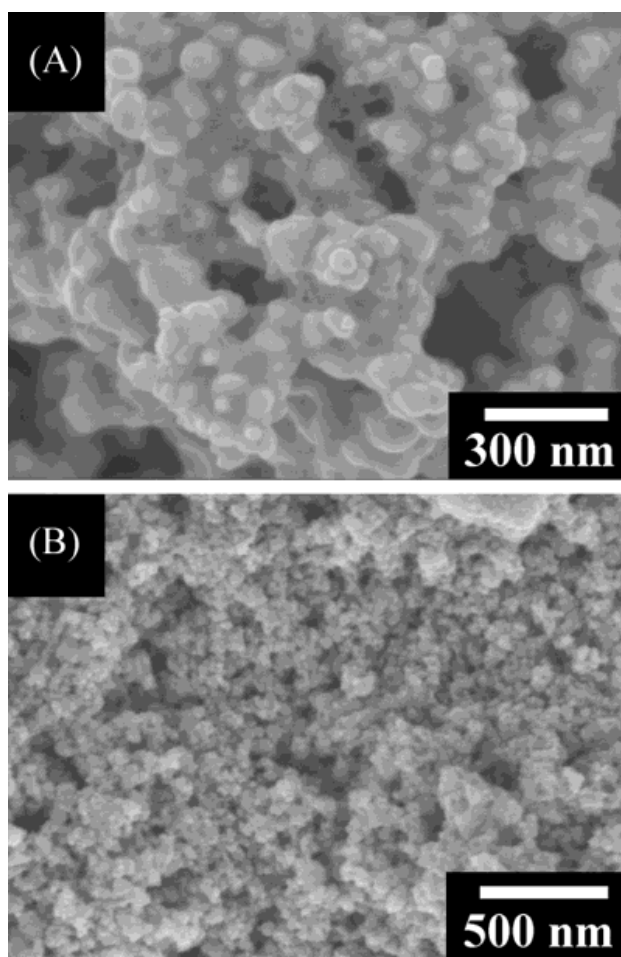


**Figure 5-9 SEM images of films, prepared from 1 g L<sup>-1</sup> BiqCOOK solution in a water–ethanol solvent, containing (a) 4 g L<sup>-1</sup> Pd, (b) 10 g L<sup>-1</sup> NiO at a deposition voltage of 30 V.**

Moreover, it was found that BiqCOOK adsorbed on NiO particles and allowed for their improved dispersion and EPD. Fig.5-9(B) shows the microstructure of the NiO film. The SEM image indicated film porosity, which can result from packing of NiO particles and gas evolution at the electrode during deposition. The BiqCOOK adsorption on the Pd and NiO particles resulted from the complex formation involving N-containing ligands of BiqCOOK and Pd or Ni atoms on the particle surface.

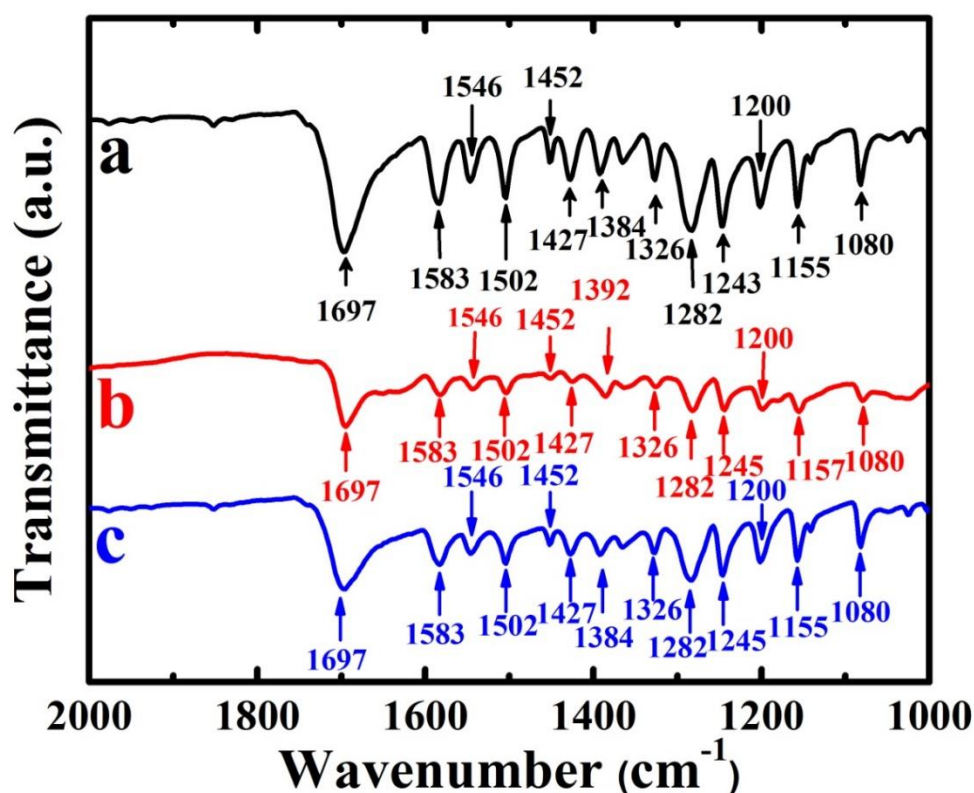


Figure 5-10 FTIR spectra of deposits, prepared from 1 g L<sup>-1</sup> BiqCOOK solution in a (a) water-ethanol solvent, containing (b) 4 g L<sup>-1</sup> Pd and (c) 10 g L<sup>-1</sup> NiO at a deposition voltage of 30 V.

The co-deposition of BiqCOOH with Pd and NiO was confirmed by the results of FTIR analysis. The FTIR spectra (Fig.5-10) of the deposited materials showed absorptions similar to the absorptions of pure BiqCOOH films. The spectra contained adsorption at  $1697\text{ cm}^{-1}$ , related to the vibration of protonated COOH groups.

Thin films of BiqCOOH were deposited by anodic electrochemical deposition from BiqCOOK solutions. The mechanism of EPD has been developed, which involved the electrophoretic transport of anionic  $\text{BiqCOO}^-$  species to the anode surface, where local pH conditions promoted the formation of insoluble BiqCOOH. The polyaromatic chelating BiqCOOK molecules showed adsorption on materials of different types, such as Pd and NiO. EPD method allowed for the deposition and co-deposition of Pd and NiO using  $\text{BiqCOO}^-$  as a dispersing and binding species. The films prepared by electrodeposition can be used for applications utilizing the functional properties of BiqCOOH and other deposited materials

### **5.1.1.3 Using Tannic acid as a capping agent for synthesis and dispersant for EPD**

Tannic acid (TA) is a natural high molecular weight polyphenol [98], which exhibits a unique set of properties for biomedical, pharmacological, food additive and other applications[99-101]. Recently interest has been generated in the development of composite TA films and coatings, utilizing bio-functional properties of TA[98].

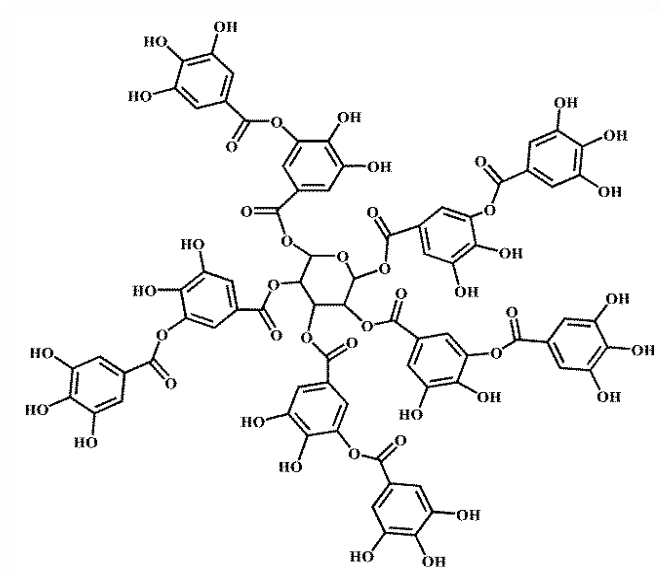


**Figure 5-11 Chemical structure of TA molecule.**

The chemical structure of TA (Fig.5-11) includes multiple galloyl groups, which promote electrostatic, hydrogen bonding, and hydrophobic interactions [102, 103]. The galloyl groups of TA provide binding sites for the formation of chelates with different metals. Several investigations [104-107] were focused on the synthesis of inorganic nanoparticles of controlled size and shape using TA as a reducing, capping and dispersing agent. TA was found to be an efficient capping agent for the hydrothermal synthesis of ZnO nanorods, which were then deposited by EPD using TA as dispersing and charging agent. The obtained films can be used for different applications based on the functional properties of TA and catalytic, flame retardant, charge storage and electronic properties of the co-deposited materials.

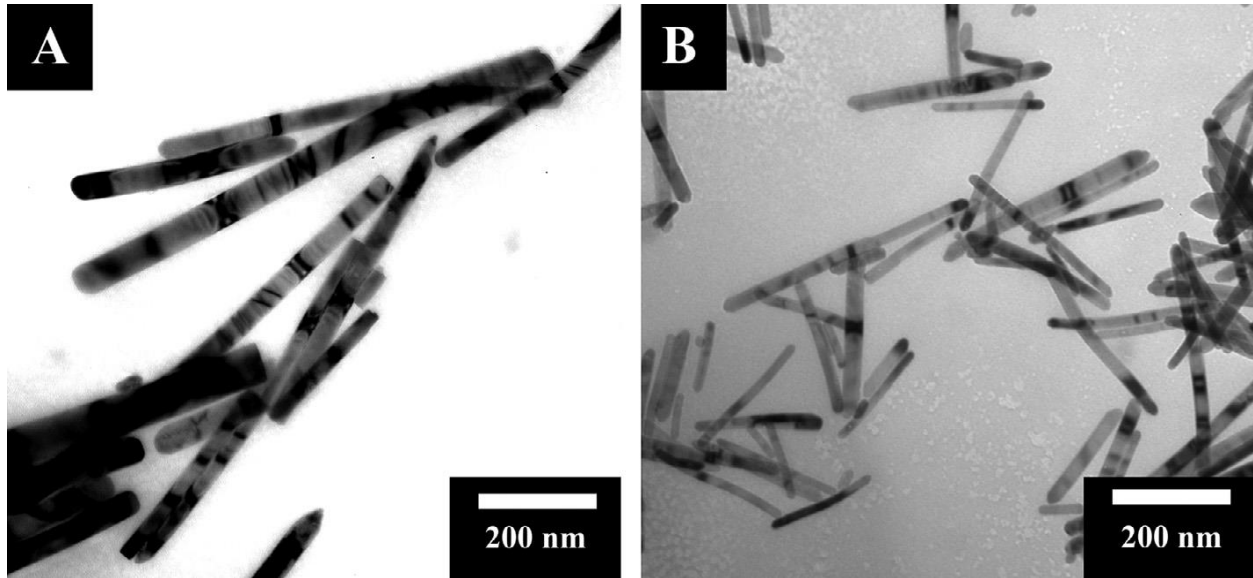


**Figure 5-12 TEM images of ZnO prepared (A) without TA and (B) in the presence of TA.**

Fig.5-12 compares the TEM images of ZnO particles, prepared without TA and in the presence of TA. The electron microscopy data indicated that the typical diameter of the rodlike particles, prepared without TA, was in the range of 50–100 nm and the length was 0.2–1.0  $\mu\text{m}$ . The size of the ZnO particles prepared in the presence of TA was significantly smaller. The particles, prepared in the presence of TA showed a nanorod morphology with typical diameter of the nanorods in the range of 15–40 nm and length of 0.2–0.3  $\mu\text{m}$ .

The ZnO particles prepared without and in the presence of TA showed X-ray diffraction patterns of the wurtzite phase (Fig.5-13). The  $2\theta$  diffraction angles of the peaks in the diffraction pattern are in agreement with the JCPDS file 36-1451. The difference in the relative intensities of the peaks, compared to the JCPDS file 36-1451, can be attributed to the rod-like morphology of the particles [86]. It is suggested that the reduction in the diameter of the ZnO particles, prepared

in the presence of TA is related to TA adsorption on the surface of growing ZnO particles during the hydrothermal synthesis. The adsorbed TA inhibited the growth of the ZnO particles.

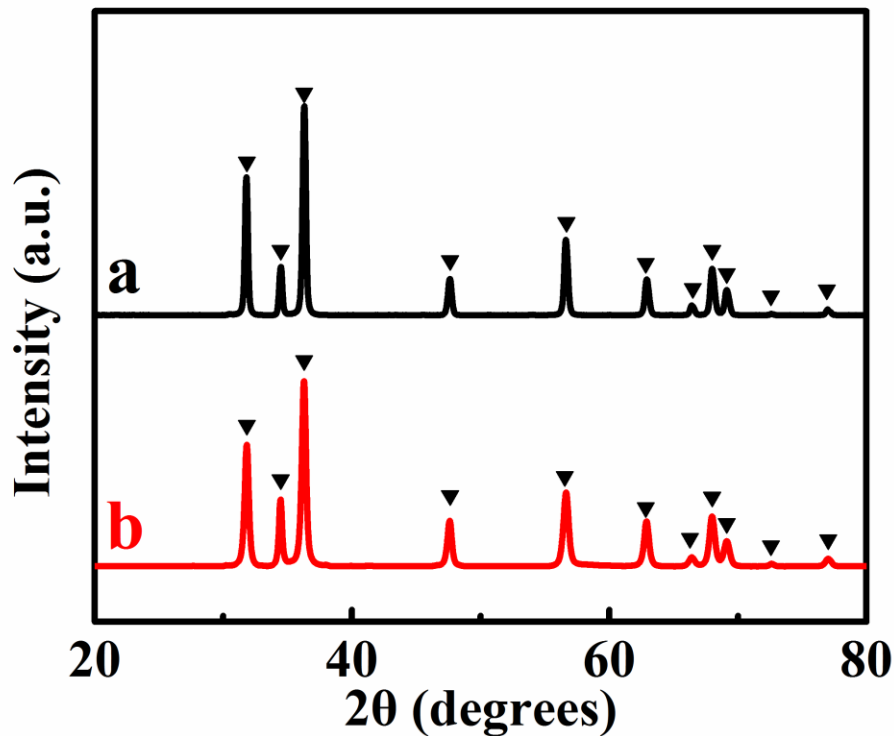


**Figure 5-13 X-ray diffraction patterns of ZnO, prepared (A) without TA and (B) in the presence of TA (▼ - ZnO, JCPDS file 36-1451).**

The ZnO particles, prepared using TA as a capping agent were deposited by EPD using TA as a dispersant and charging agent. The SEM image of the film (Fig.5-13) shows ZnO nanorods in the TA matrix.

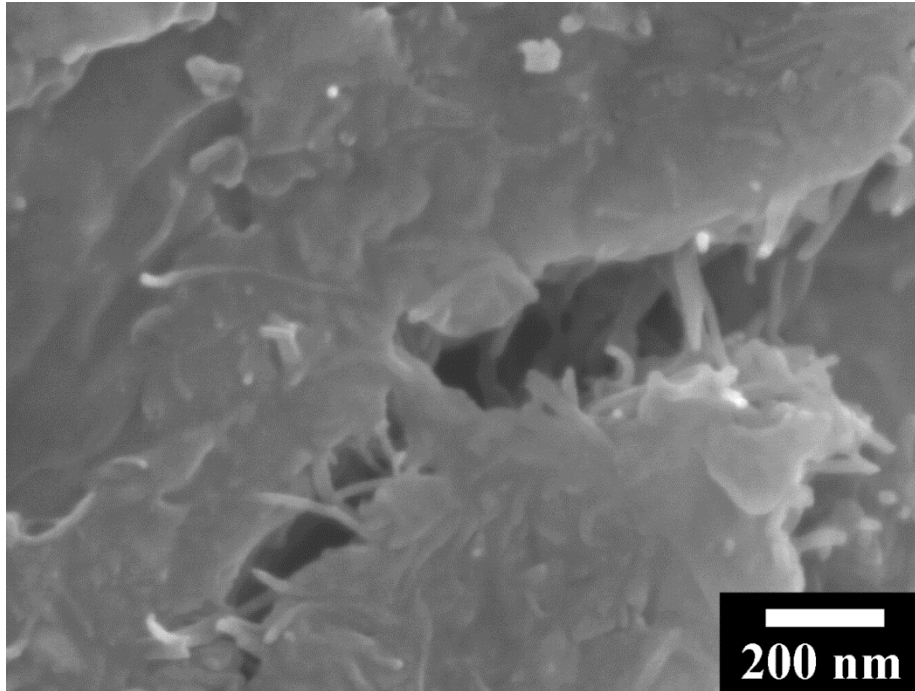


**Figure 5-14 SEM image of the film, prepared at a deposition voltage of 30 V from 4 g L<sup>-1</sup> ZnO suspensions in ethanol, containing 1 g L<sup>-1</sup> TA. ZnO was synthesized in the presence of TA, arrow show ZnO particles.**

#### **5.1.1.4 Using Lauryl gallate as a reducing and dispersing agent for the fabrication of silver nanoparticles by liquid–liquid extraction**

The goal of this investigation was the use of lauryl gallate (LG) for the synthesis and dispersion of inorganic particles and fabrication of advanced composites using a liquid–liquid extraction technique. The structure of LG includes the galloyl group and a long hydro-carbon chain (Fig.5-15A). LG is well soluble in n-butanol; however, it is insoluble in water. The results

presented below indicated that LG allowed for the reduction of  $\text{Ag}^+$  ions to form Ag nanoparticles (AgNp) and extraction of AgNp to the n-butanol phase.

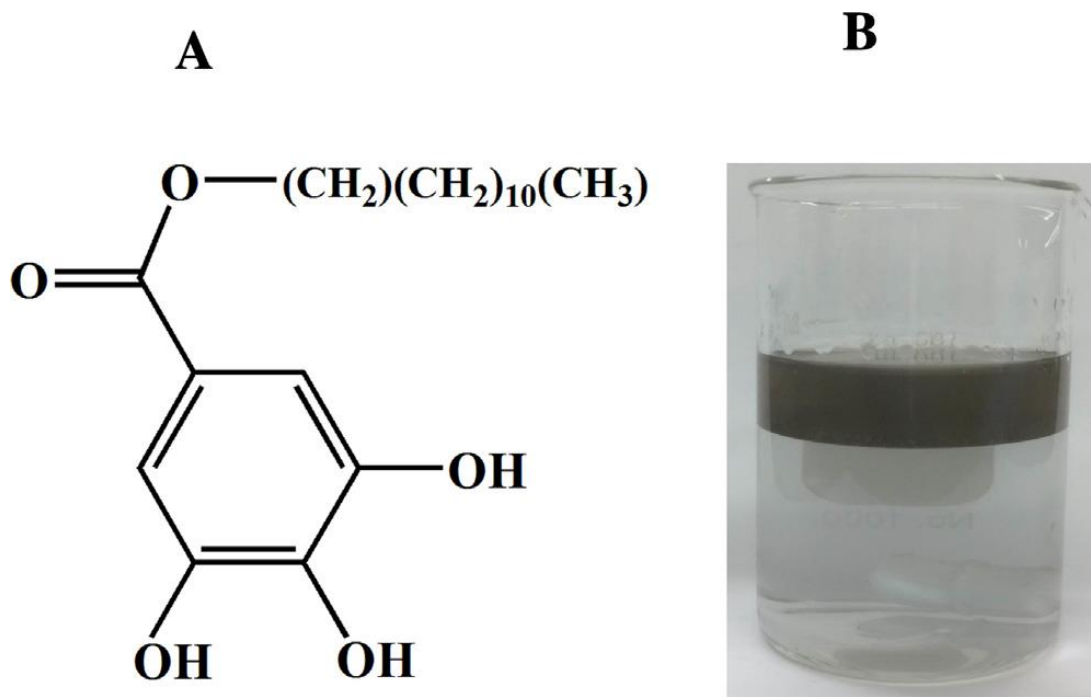


**Figure 5-15 (A) Chemical structure of LG, (B) extraction of AgNp to the n-butanol phase using LG.**

Our approach was based on the use of LG as a reducing and dispersing agent. We suggested that the galloyl group of LG can provide LG adsorption on inorganic surfaces via a mechanism, similar to the adsorption mechanisms of gallic acid and catecholates, which involved phenolic OH groups [81]. The larger size of LG, compared to that of gallic acid, offers the advantages of improved steric stabilization of inorganic particles by adsorbed LG. It was hypothesised that similar to other head and tail surfactants [108, 109], containing long hydrocarbon chains, the LG molecules can be used for the dispersion of carbon nanotubes. Therefore, it was expected that LG

can be used as a co-dispersant for the fabrication of composites, containing different oxides, metals and carbon nanotubes.

Based on literature data on the redox properties of the galloyl group of gallic acid [110, 111] and application of gallic acid and lauryl gallate as a reducing agent for  $\text{Ag}^+$ , we suggested that LG, containing a galloyl ligand, can also be used as a reducing agent for the formation of AgNp from the  $\text{AgNO}_3$  solutions. The water-n-butanol two-phase solvent system is widely used for the extraction of different solutes from aqueous to the n-butanol phase [112-115]. In our investigation we used the water-n-butanol system for particle extraction.

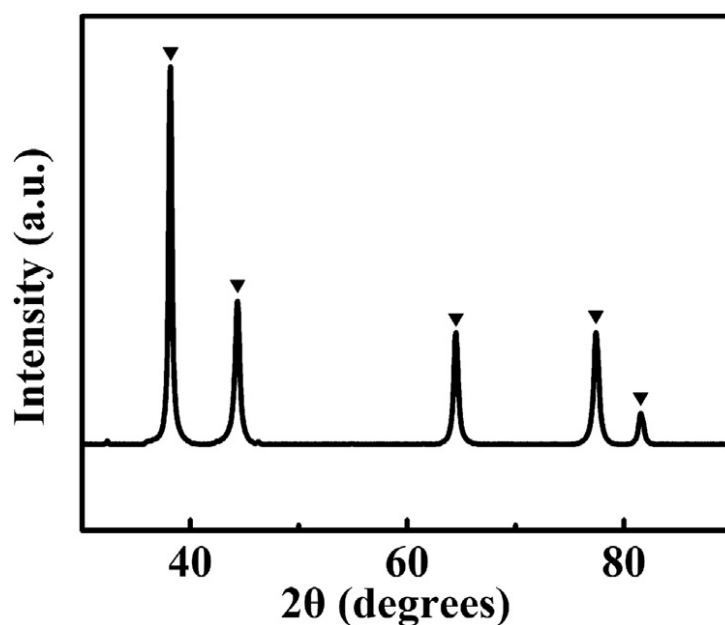


**Figure 5-16 X-ray diffraction pattern of AgNp, obtained by reduction of  $\text{AgNO}_3$  with LG (▼ - JCPDS file 04-0783).**

The XRD studies of the particles, prepared from the  $\text{AgNO}_3$  solutions showed diffraction peaks of Ag, corresponding to the JCPDS file 04-0783 (Fig.5-16). Therefore, similar to gallic acid,

the LG molecules can be used as a reducing agent for the synthesis of Ag. It is important to note that LG is insoluble in water, but well soluble in n-butanol. This is in contrast to gallic acid, which is well soluble in water and allows synthesis of AgNp in aqueous solutions of AgNO<sub>3</sub>. The redox reaction of Ag<sup>+</sup> and LG during stirring of the aqueous and n-butanol phases resulted in the formation of AgNp, which were transferred to the n-butanol phase by the adsorbed LG. Turning again to Fig.5-15B, it is seen the liquid–liquid separation after stirring resulted in the formation of Ag suspension in n-butanol. Fig.5-17 shows a TEM image of the AgNp. The particle size was in the range of 30–100 nm. The selected area electron diffraction pattern(Fig.5-17, inset) showed particle crystallinity in agreement with the X-ray diffraction data (Fig.5-16).

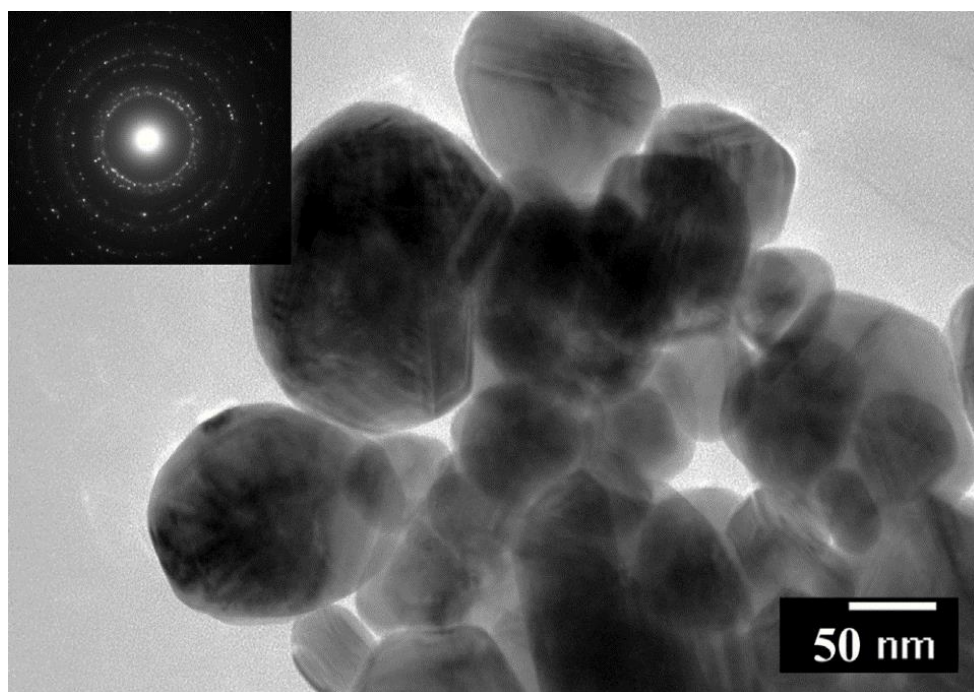


**Figure 5-17 TEM image of AgNp, obtained by reduction of AgNO<sub>3</sub> with LG, inset shows a corresponding selected area electron diffraction pattern.**

The extraction of the Ag particles from the aqueous to the n-butanol phase was possible due to LG adsorption on the particles. The adsorption was confirmed by the FTIR studies of the extracted particles. The FTIR spectra (Fig.5-18) showed characteristic peaks of adsorbed LG [116]. However, similar to other investigations of LG adsorption on TiO<sub>2</sub> particles [116, 117], the peaks of adsorbed material in the range of 1000–1800 cm<sup>-1</sup> showed significant broadening, compared to the peaks of pure LG. The adsorption mechanism of LG on inorganic particles involves complexation of metal atoms on the particle surface with phenolic OH group of LG [117].

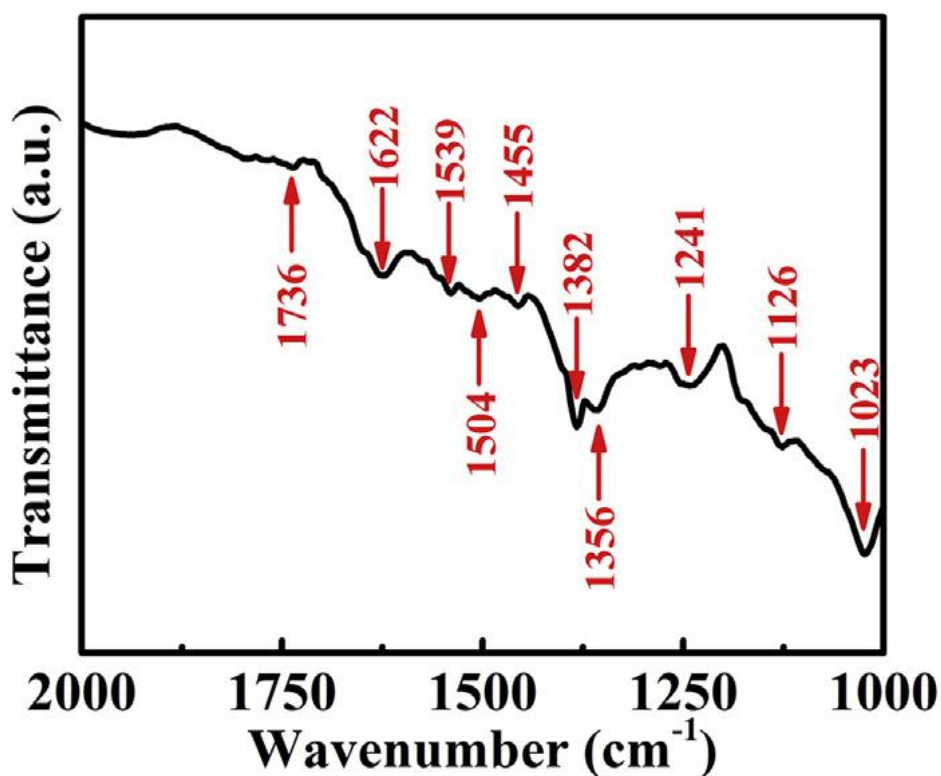


Figure 5-18 FTIR spectra of AgNp extracted to n-butanol using LG.

## 5.1.2 Chelating polymers

### 5.1.2.1 PAZO as universal dispersant for EPD

In this investigation, the poly[1-[4-(3-carboxy-4hydroxyphenylazo) benzenesulfonamido]-1,2-ethanediyl, sodium salt] (PAZO) was used as a charging and dispersing agent for the EPD of composite materials. Thanks to the chemical structure (Fig.5-19), PAZO shows significant benefits for application in EPD.

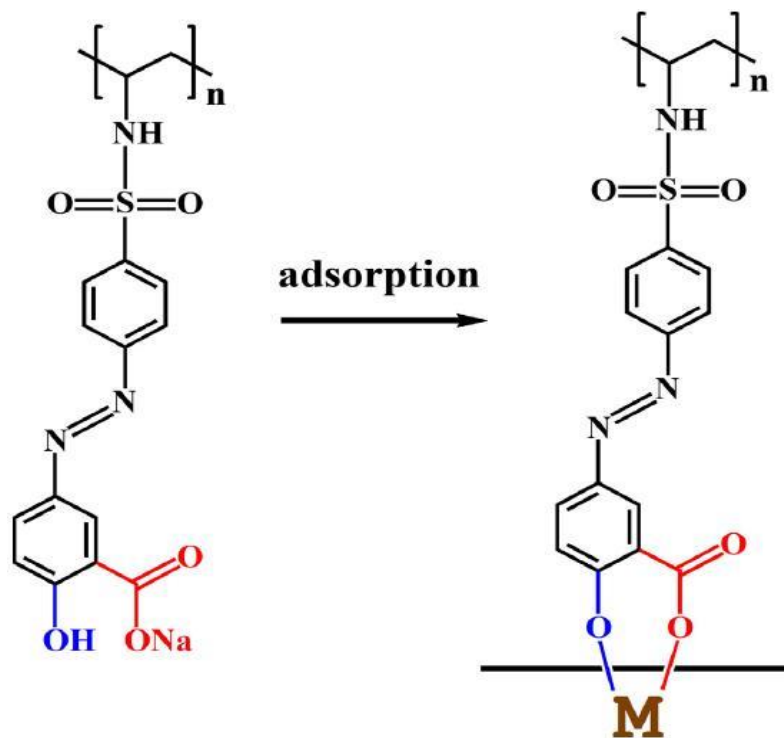


Figure 5-19 Structure and adsorption mechanism of PAZO on surface of inorganic material.

The pH dependent charge of the PAZO monomers is related to  $\text{COO}^-$  groups. The chelating salicylate ligands of the PAZO monomers can create multiple adsorption sites on surfaces of inorganic particles (Fig.5-19). Therefore, improved adsorption can be expected, compared to the small salicylate family dispersants which only contain a single salicylate ligand [81]. Moreover, the use of PAZO polymer, containing charged monomers with anionic salicylate ligands, offers the advantages of improved electrosteric stabilization.

It is known that PAZO exhibits important physical properties, which are currently under intensive investigation for applications in photonics, optoelectronics, memory devices and sensors [118-120]. PAZO showed a photo-induced birefringence [118], resulting from reversible trans-cis-trans photoisomerization of azo groups (Fig.5-19). Of particular interest are investigations focused on the analysis of optical storage and photochromic properties, surface-relief grating [121, 122], azobenzene trans-cis-trans transitions, birefringence [19] and development of light sensitive biosensors [119]. Therefore, the use of PAZO as a dispersing, charging and film forming agent for the EPD technology can add functional properties to the deposited material.

Our experimental results presented below indicate that pure PAZO films can be prepared by constant voltage EPD. An important finding was the possibility of EPD of various materials, using PAZO as a charging, dispersing, binding and film forming agent. This was exemplified by the deposition of individual oxides, such as ZnO, complex oxides such as  $\text{Al}_2\text{TiO}_5$ ,  $\text{ZrSiO}_4$ , different nitrides, such as BN, and also hydrotalcite clay. The deposition rate, deposit composition and microstructure can be varied. As a natural extension of this investigation we have demonstrated a possibility of EPD of composites, using PAZO as a co-dispersant for different

materials. The results indicated that a large number of applications are possible because of the use of PAZO for EPD technology.

PAZO is an anionic polyelectrolyte, containing  $\text{COO}^-$  groups, which exhibit pH-dependent charge. In this investigation we used a soluble Na salt of PAZO. It is known [118] that insoluble acidic form of PAZO can be obtained by precipitation at low pH. The pH-dependent charge and pH-dependent solubility of PAZO [118, 123] are important properties for the fabrication of PAZO films by anodic EPD. In this process, the electrochemical decomposition of water resulted in a local pH decrease at the anode surface:



Electrophoresis causes accumulation of anionic PAZO molecules at the anode surface, where charge neutralization of  $\text{COO}^-$  groups and precipitation of the acidic form of PAZO results in the formation of PAZO films:



The addition of PAZO to the suspensions of individual oxides, such as ZnO, complex oxides such as  $\text{Al}_2\text{TiO}_5$ ,  $\text{ZrSiO}_4$ , different nitrides, such as BN, and also hydrotalcite clay, allowed for anodic deposits of these materials to be formed by EPD. The deposition yield in the EPD process depends on various parameters, such as deposition time, electric field, concentration of particles, particle size, particle density and particle surface area, concentration of dispersant, chemical properties of particles, composition of solvent and other factors. We present the deposition yield data for different materials at selected deposition voltage of 100 V and deposition

time of 4 min in a mixed ethanol–water (25% water) solvent for PAZO concentrations in the range of 0–1 g L<sup>-1</sup>. The experimental results presented below give an example of the deposition conditions and quantitative information about the deposition yield at the selected conditions. However, the same materials can also be deposited at different voltages, deposition times, solvent composition and concentrations of PAZO and inorganic particles.

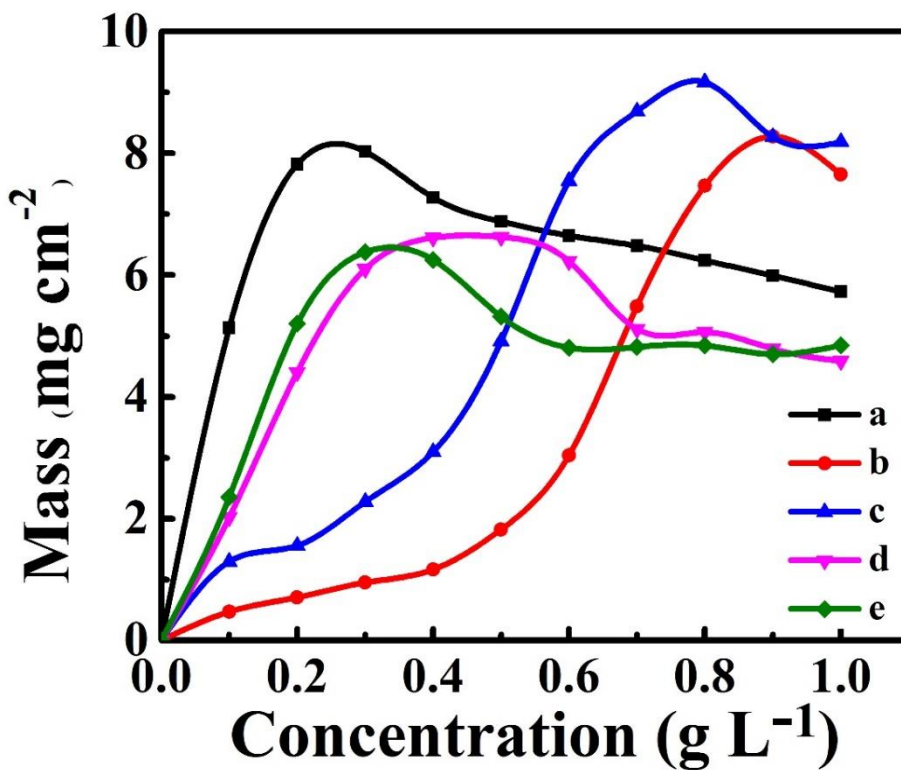


**Figure 5-20** Deposit mass versus PAZO concentration in suspensions, containing 4 g L<sup>-1</sup> of (a) ZNO, (b) Al<sub>2</sub>TiO<sub>5</sub>, (c) ZrSiO<sub>4</sub>, (d) BN, (e)Hydrotalcite at a deposition voltage of 100 V and deposition time of 4 min.

It is suggested that the increase in PAZO concentration in the suspensions resulted in increasing adsorption of PAZO on the particles of oxides and nitrides, and therefore increasing particle charge and mobility. As a result, we observed the increase in deposition yield with increasing PAZO concentration in the range of low concentrations (Fig.5-20). The deposition yields versus PAZO concentration dependences exhibited maxima, enabling the optimal PAZO concentration for each material to be determined for selected deposition conditions.

The SEM images of deposits formed from  $4 \text{ g L}^{-1}$  suspensions listed previously in a  $1 \text{ g L}^{-1}$  PAZO solution are shown in Fig.5-21. Deposition from these relatively concentrated suspensions resulted in porous films. The film porosity was the result of particle packing, with the pores comparable in size to the deposited particles. It was found that the deposit morphology and composition could be varied by changing the particle concentration.

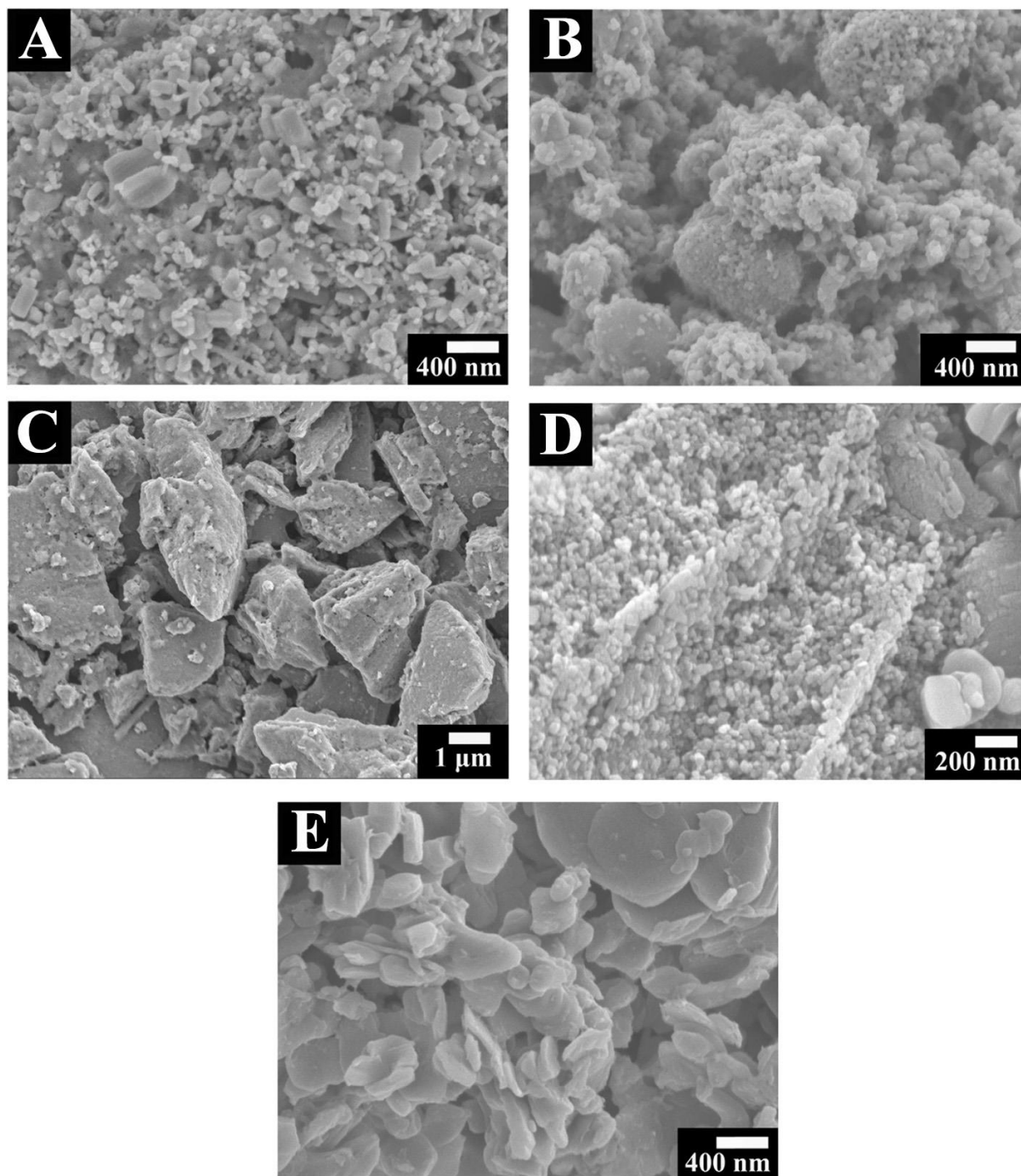


**Figure 5-21 SEM images of deposits, prepared from 1 g L<sup>-1</sup> PAZO solutions, containing 4 g L<sup>-1</sup> (A) ZnO, (B) Al<sub>2</sub>TiO<sub>5</sub>, (C) ZrSiO<sub>4</sub>, (D) BN, and (E) Hydrotalcite.**

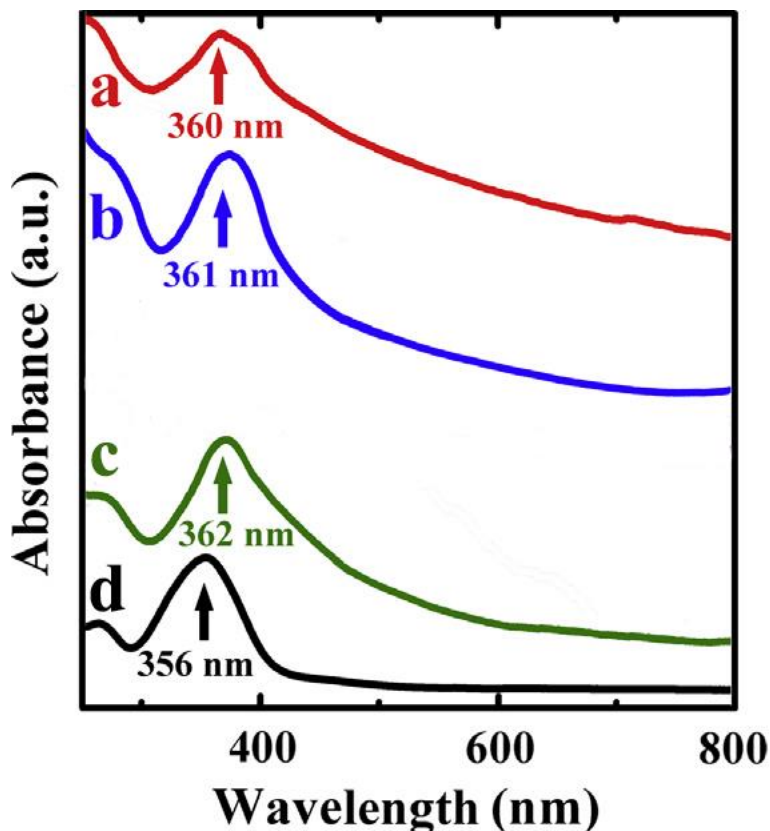


**Figure 5-22 UV-Vis spectra of the deposits, prepared from 1 g L<sup>-1</sup> PAZO solutions, containing 4 g L<sup>-1</sup> of (a) BN, (b) hydrotalcite, (c) ZnO and (d) ZrSiO<sub>4</sub>.**

The porous deposits, shown in Figs.5-21, contained PAZO, adsorbed on the inorganic particles which was confirmed by UV-Vis analysis of the deposits. Fig.5-22 shows typical UV-Vis spectra of different materials. The UV-Vis spectra showed maxima in the range of 356–363 nm. Such absorption maxima are related to PAZO, adsorbed on the particle surface. It is known that UV-Vis spectra of PAZO exhibit absorption at ~360 nm which has been attributed to the

trans-cis photoisomerization of PAZO [124], indicating adsorption of PAZO on the deposited particles surface. The confirmation of PAZO adsorption on the surface of the particles by UV-Vis spectroscopy seems to support the suggested deposition mechanism, which involved the adsorption of PAZO on the particle surface and electrophoresis of the particles, with adsorbed charged polymer. The chelating salicylate ligands of PAZO monomers provided multiple adsorption sites for PAZO adsorption on inorganic materials. The charge neutralization of PAZO at the electrode surface (Eq.5-3) promoted deposition. The adsorption of PAZO on different materials was also confirmed by thermogravimetry. The adsorbed amount of PAZO was found to be 5.39, 6.59 and 15.68 mg/g for ZnO, ZrSiO<sub>4</sub>, and Al<sub>2</sub>TiO<sub>5</sub>, respectively.

PAZO films were prepared by anodic EPD under constant voltage conditions. The deposition mechanism of PAZO has been developed, which involved the electrophoresis of the negatively charged PAZO species towards the anode, the local pH decreases at the anode surface, charge neutralization and deposition of the insoluble acidic form of PAZO. It was found that PAZO exhibits unique adsorption properties on various materials, attributed to the chelating properties of the salicylate ligands of PAZO monomers. The salicylate ligands of individual monomers created multiple adsorption sites and provided adsorption on inorganic surfaces by complexation of metal atoms. The adsorption properties are of critical importance for PAZO application as a dispersing agent for EPD. The properties of PAZO for application in EPD have been exemplified by EPD of a large variety of different materials, including individual oxides (ZnO), complex oxide compounds (Al<sub>2</sub>TiO<sub>5</sub>, ZrSiO<sub>4</sub>), different nitrides (BN) and also hydrotalcite clay. These results allowed to overcome the limitations of other dispersing agents, which can be used for specific materials only, and paved the way for application of PAZO as a universal dispersing agent for EPD

of inorganic materials. Another major finding was the possibility of fabrication of composites using PAZO as a co-dispersant for different materials. It was found that the method offers advantages of high deposition rate, deposit microstructure and composition control, the ability to deposit thin and thick films. The versatility of PAZO as a universal charging, film-forming and dispersing agent coupled with the flexibility and control offered by EPD opens new strategies for future work on the development of specifically engineered composite films for a wide variety of applications, utilizing optical, magnetic, ferroelectric, catalytic, electrochemical and other properties of PAZO and inorganic materials.

### 5.1.2.2 EPD of materials using poly(styrene-alt-maleic acid) as a dispersant

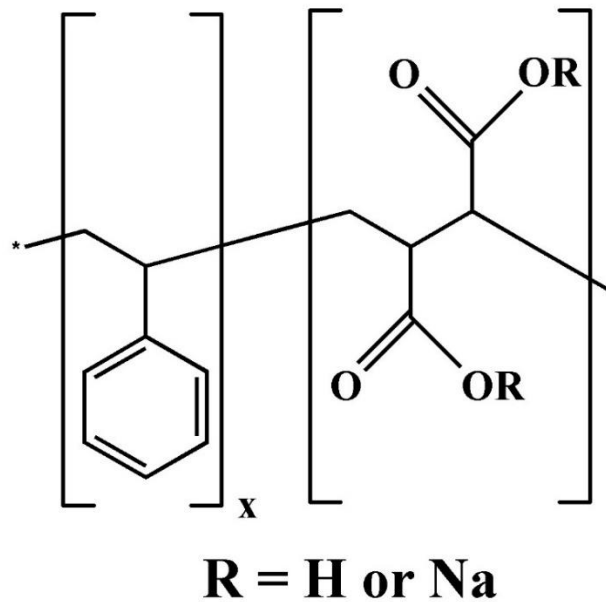


Figure 5-23 Chemical structure of PMSS.

Poly(styrene-alt-maleic acid) sodium salt (PMSS) was used as a dispersant for EPD of materials. PMSS is a chelating polymer. The chelating properties of PMSS are attributed to  $\text{COO}^-$  groups (Fig.5-23), which provide electric charge for the electrosteric dispersion.

It was found that PMSS adsorbed on ceramic particles, provided electrosteric dispersion and allowed for their EPD. We present (Fig.5-24) the deposition yield data for different materials at selected deposition voltage of 70 V and deposition time in the range of 1-3.5 min in a mixed ethanol-water (40% water) solvent. The deposition yield increased with increasing deposition time, indicating the possibility of controlled deposition.

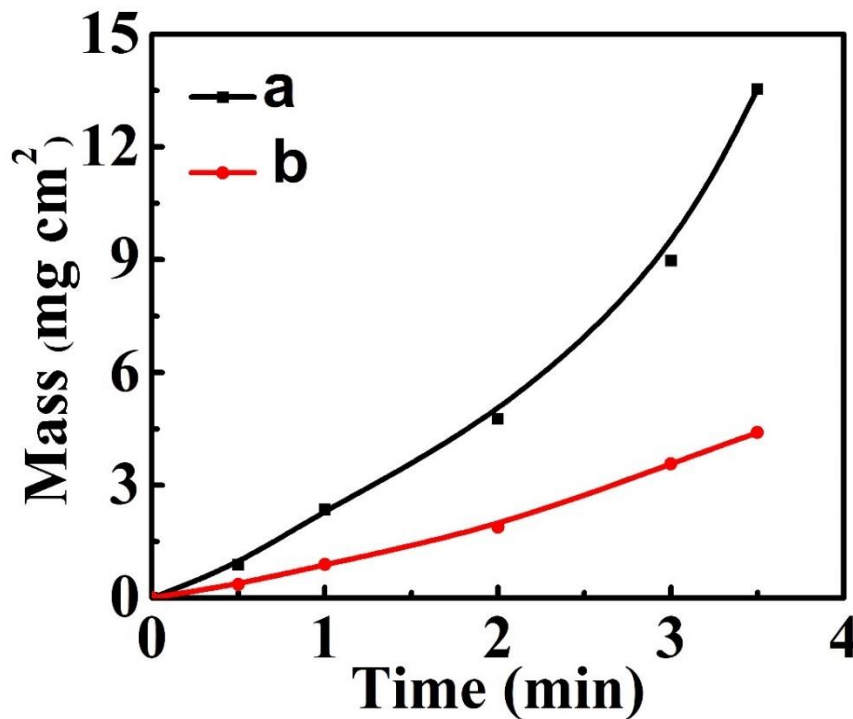
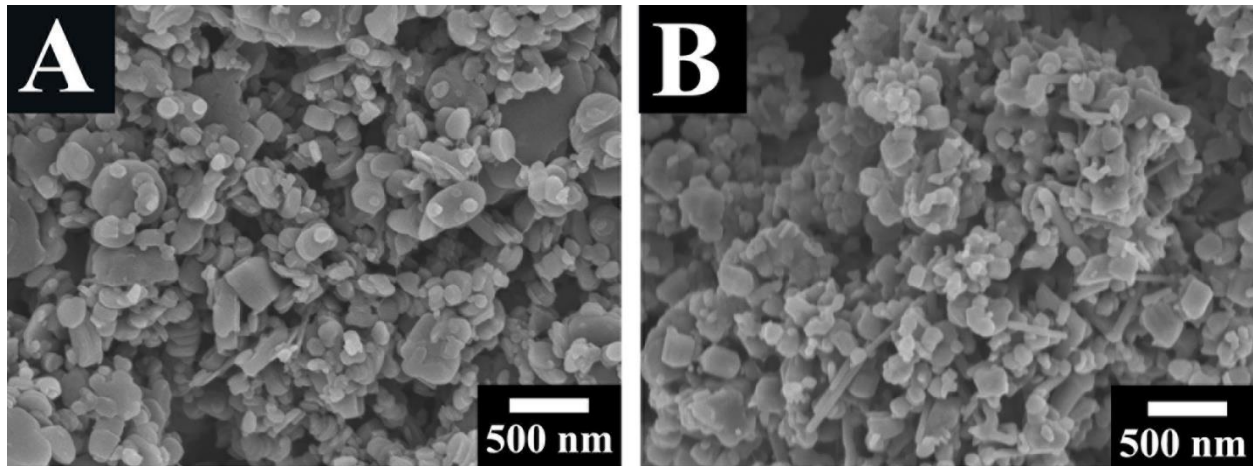


Figure 5-24 Deposit mass versus time for deposits prepared from 1 g L<sup>-1</sup> PMSS solutions, containing 10 g L<sup>-1</sup> (a) BN and (b) Si<sub>3</sub>N<sub>4</sub>.

Fig.5-25 shows SEM images of the deposited materials. The particle size is in agreement with the data provided by the powder manufacturers. The deposit porosity is attributed to packing of the particles and gas evolution at the electrode surface.



**Figure 5-25 SEM images of deposits, prepared from  $1 \text{ g L}^{-1}$  PMSS solutions, containing  $10 \text{ g L}^{-1}$  (A) BN and (B)  $\text{Si}_3\text{N}_4$ .**

## 5.2 Electrophoretic deposition of ceramics using weak polyelectrolytes

The polyelectrolytes can be categorized into two groups: strong polyelectrolytes, for which the degree of ionization is independent of the solution pH, and weak polyelectrolytes, for which the degree of ionization is determined by the solution pH. Weak polyelectrolytes usually contain functional groups like carboxylic or amino groups with pH dependent charge. In this part, alginate acid, a weak polyelectrolyte, was used to fabricate alginate-huntite composite coatings.

EPD offers many processing advantages for the deposition of polymers for biomedical devices, corrosion protection and energy storage devices [125, 126]. Various strategies for EPD of polymers and polymer matrix composites have been exemplified [126]. An important requirement for many applications of polymer coatings is their flame retardancy [127]. There is a strong need to incorporate FRA in various polymer products [127-129]. It was recognised that mineral huntite ( $\text{Mg}_3\text{Ca}(\text{CO}_3)_4$ ) is a promising FRA for many applications. The flame retardant properties of huntite [130, 131] are related to its endothermic decomposition and release of  $\text{CO}_2$  gas, which reduces the oxygen access to the flammable polymer material. Huntite offers advantage of lower cost, compared to other FRA, such as aluminium hydroxide and magnesium hydroxide [131]. Moreover, the production of aluminium and magnesium hydroxides generates a problem related to the disposal of toxic chemical waste [131]. It is expected that huntite can replace toxic [128, 129] halogenated FRA, in many polymer products. Polymer-huntite composites showed improved mechanical properties compared to pure polymers [130, 131]. The goal of this investigation was

the development of the EPD method for the deposition of polymer coatings, containing huntite as an FRA. The approach was based on anodic EPD using alginate as model anionic polymers. For the first time we demonstrate the possibility of EPD of polymer–huntite composites.

Alginic acid coatings can be deposited by anodic EPD from sodium alginate solutions. In this method, electrophoresis of the anionic alginate molecules, results in their accumulation at the anode surface. The deposition mechanism involved local pH decrease at the anode surface, protonation of  $\text{COO}^-$  groups of the polymers and precipitation of insoluble alginic acid at the electrode [132].

The major difficulties in the fabrication of composite coatings were related to the dispersion, charging and deposition of huntite. Sedimentation tests showed that alginate improved dispersion and stability of the huntite suspensions. The huntite suspensions, containing alginate were stable for more than 3 days. Anodic deposits were obtained from huntite suspensions, containing alginate. The deposit mass increased with increasing deposition time, indicating the possibility of EPD of coatings of controlled mass (Fig.5-26). The deposition yield, achieved from huntite suspensions, containing alginate was significantly higher, compared to that achieved from pure polymer solutions [132]. The electrophoretic mobilities of the huntite particles in the  $4 \text{ g L}^{-1}$  huntite suspensions without additives, containing  $1 \text{ g L}^{-1}$  sodium alginate were found to be  $-0.32 \cdot 10^{-9}$  and  $-1.12 \cdot 10^{-7} \text{ m}^2 \text{ s}^{-1} \text{ V}^{-1}$ , respectively.

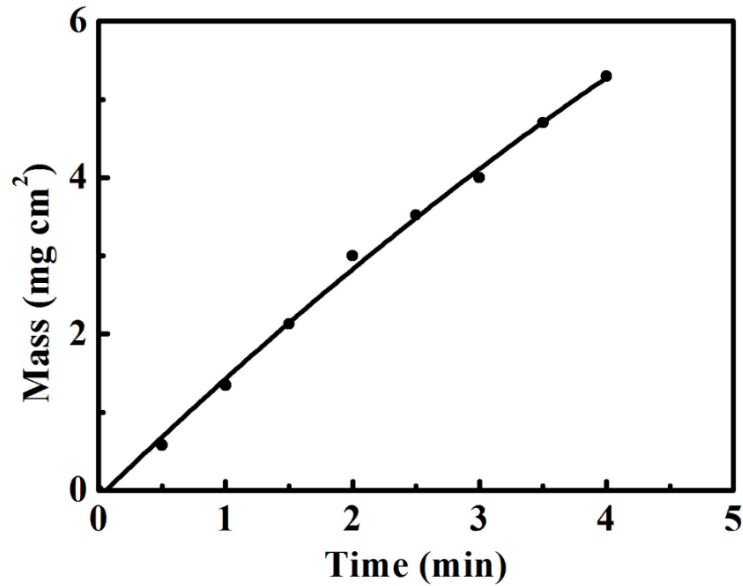


**Figure 5-26 Deposit mass versus time for deposits prepared from 4 g L<sup>-1</sup> huntite suspension, containing 1 g L<sup>-1</sup> sodium alginate.**

The comparison of X-ray diffraction patterns of as-received huntite and composite coatings showed that huntite was incorporated into the polymer coatings (Fig.5-27A). The XRD patterns of coatings showed peaks of huntite, similar to the peaks of as-received huntite material. The formation of composite coatings was also confirmed by FTIR. The FTIR spectrum of as-received huntite showed characteristic absorptions [133] at 870 and 891 cm<sup>-1</sup>, attributed to carbonate ligands (Fig.5-27B). Similar absorptions observed in the spectra of the composite coatings.

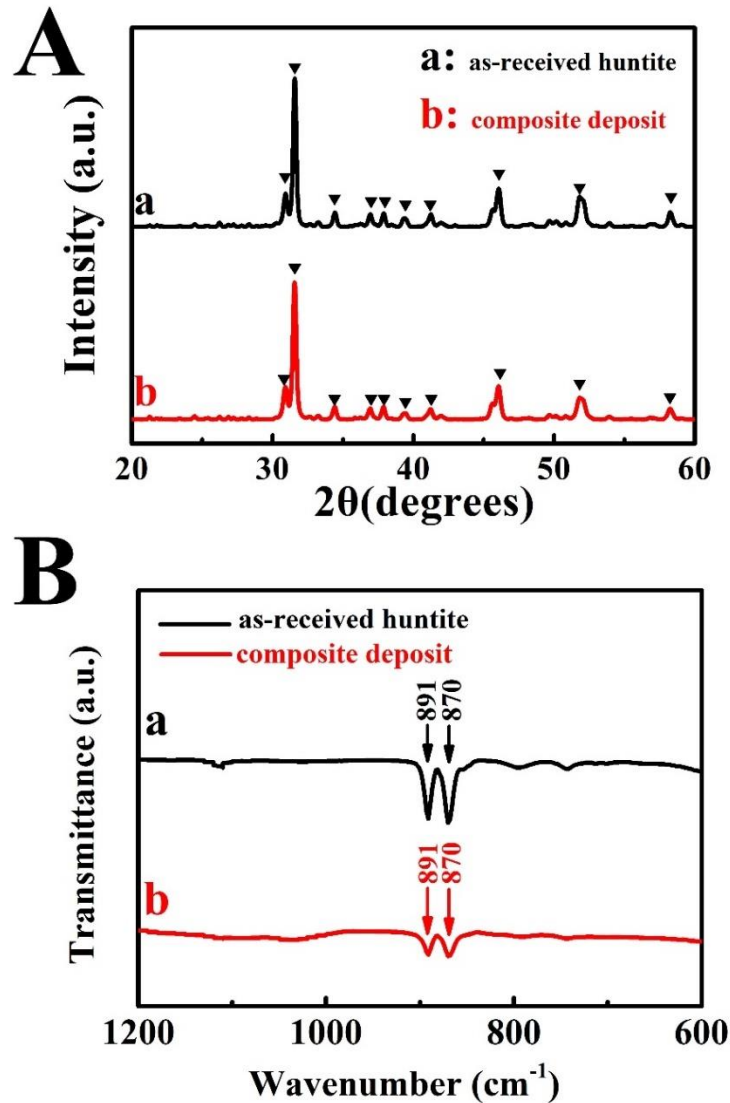
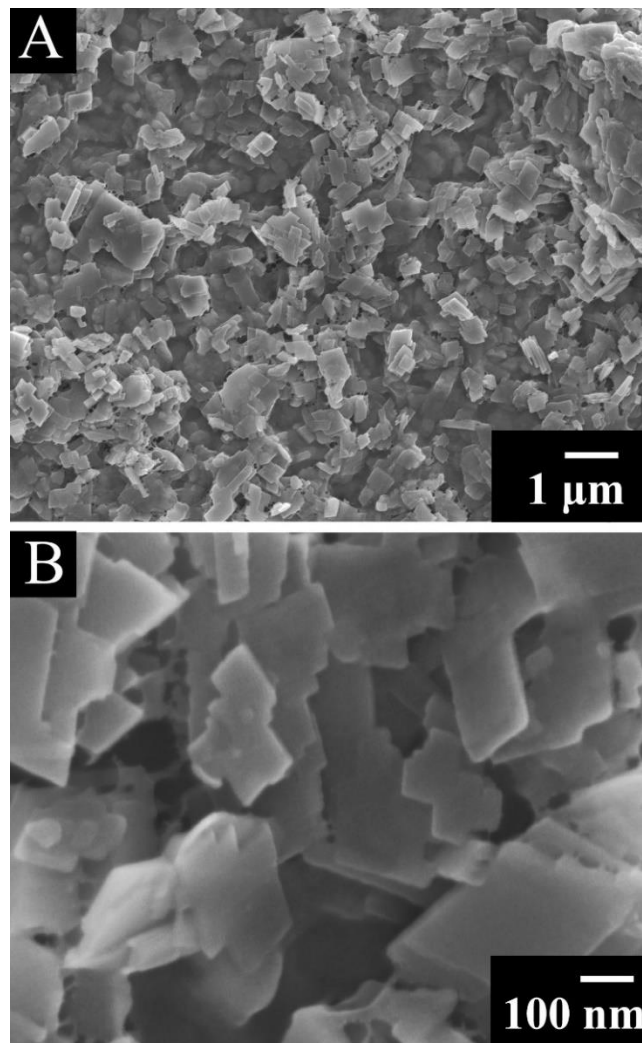


Figure 5-27 (A) XRD and (B) FTIR data for (a) as-received huntite, and (b) deposit, prepared from  $4 \text{ g L}^{-1}$  huntite suspension, containing  $1 \text{ g L}^{-1}$  sodium alginate ( $\blacktriangledown$  - huntite, JCPDS file 014-0409).

The SEM studies (Fig.5-28) at low magnifications showed the formation of continuous coatings, containing platy huntite particles. The SEM images at higher magnifications showed that

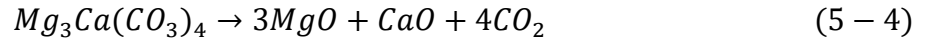
the typical size of the plate-like particles is on the submicrometre scale. The shape of the huntite particles is of special interest for flame retardant applications. It is known[131] that platy morphology helps to reduce the rates of heat transfer and gas transfer. It is also beneficial for the polymer reinforcement [131]. The adhesion test (ASTM standard D3359) showed that coating adhesion corresponded to 5B classification.



**Figure 5-28 SEM images at different magnifications for coatings, prepared from 4 g L<sup>-1</sup> huntite suspension, containing (A and B) 1 g L<sup>-1</sup> sodium alginate.**

The TGA studies of as-received huntite showed two major steps in mass loss (Fig.5-29A).

The total mass loss of 48.9 % at 1000 °C is related to release of four CO<sub>2</sub> molecules:



The first step in the mass loss (36.7%) below ~600 °C corresponds to release of three CO<sub>2</sub> molecules [134] (theoretical mass loss 37.4%) bonded to Mg atoms. A step in the mass loss at higher temperature is related to release of additional CO<sub>2</sub> molecule, bonded to Ca atoms. No mass loss was observed at temperatures above 800 °C.

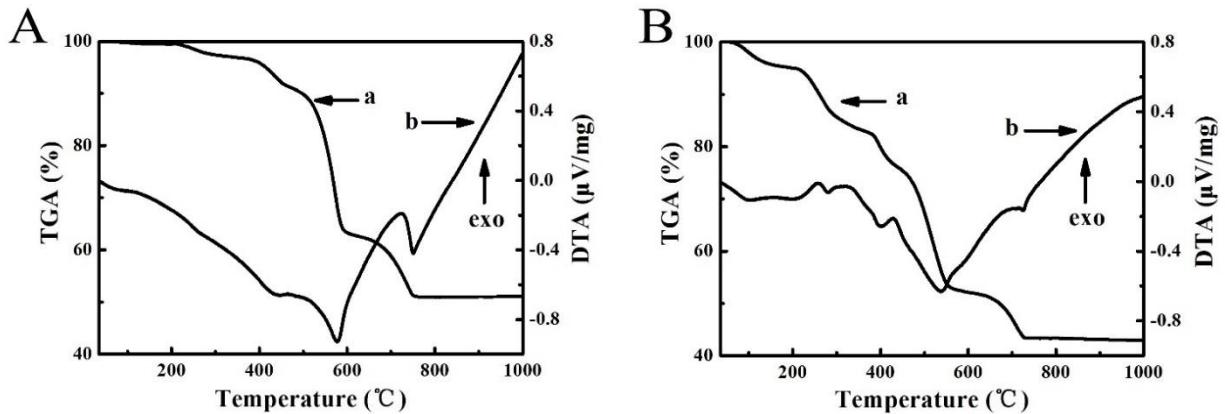


**Figure 5-29 (a) TGA and (b) DTA data for (A) as-received huntite and deposits, prepared from 4 g L<sup>-1</sup> huntite suspension, containing (B) 1g L<sup>-1</sup> sodium alginate.**

The DTA data showed two endothermic peaks, corresponding to observed steps in the mass loss. The TGA data for the composite materials (Fig.5-29B) showed several steps in mass loss. The total mass loss for alginic acid–huntite composites at 1000 °C was found to be 57.1%. The additional mass loss for deposits (Fig.5-29B), compared to that of pure huntite (Fig.5-29A), can

be attributed to burning out of the polymers. Therefore, the results of TGA analysis confirmed the formation of composite coatings. The compositions of the coatings, estimated from the results of the TGA analysis, were found to be 84.0 mass% huntite and 16.0 mass% alginic acid. The corresponding DTA data showed endothermic peaks related to decomposition of huntite and small exotherms below 500 °C, related to burning out of the polymers.

The results of this investigations indicated that composite coatings with relatively large huntite content can be obtained. Moreover, we found that the amount of huntite in the coatings can be varied by the variation of the huntite concentration in the polymer solutions. It is suggested that alginate adsorbed on huntite particles and imparted a negative charge for anodic EPD. The adsorption mechanism can result from interactions of carboxylic groups of the polymers with Mg and Ca atoms on the particle surface. It is expected that similar approach can be used for the codeposition of huntite with other anionic polymers. EPD is especially attractive for the deposition of FRA materials due to room temperature processing and stoichiometry control of the inorganic phase.

The Tafel plots presented in Fig.5-30 indicated that composite coating provided corrosion protection of stainless steel, as indicated by increased corrosion potential and reduced anodic current. The corrosion potentials were -389.3 and -150.9 mV, corrosion currents were 2.552 and 0.0668  $\mu\text{A cm}^{-2}$ , and corrosion rates were 26.44 and 0.69  $\mu\text{m/year}$  for uncoated samples and alginic acid–huntite coated samples, respectively. It is suggested that platy morphology of the huntite particles was also beneficial for there reduction of electrolyte diffusion rate and improved corrosion protection. Taking into account the industrial importance of EPD for the deposition of

various polymers, the results of this investigation indicated that EPD is a promising technique for the fabrication of flame retardant coatings for various applications.

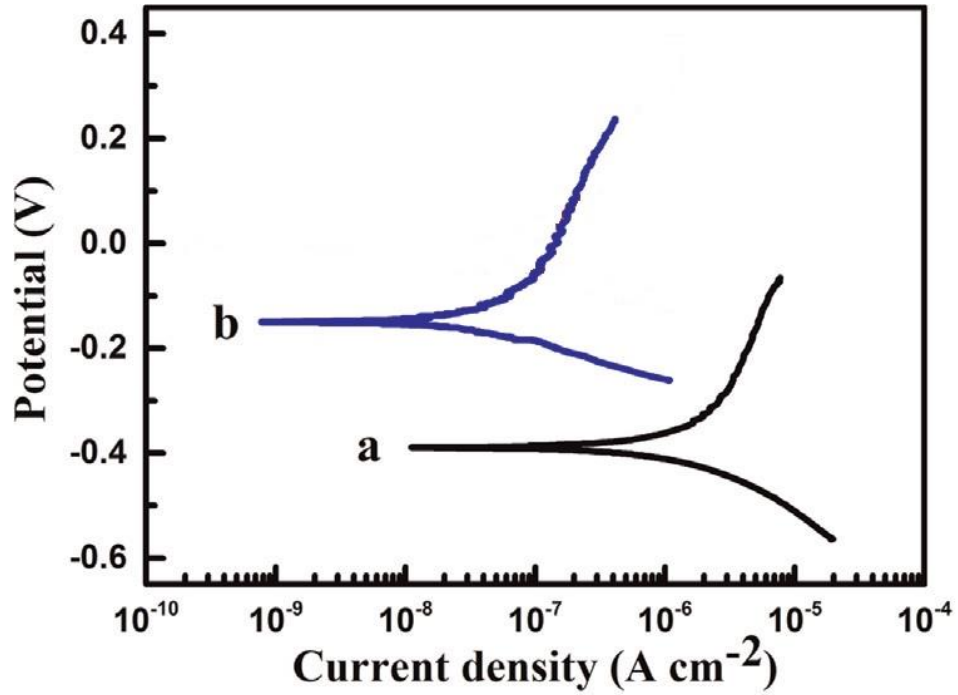


Figure 5-30 Tafel plots for (a) uncoated stainless steel, and coated from 4 g L<sup>-1</sup> huntite suspension, containing and (b) 1 g L<sup>-1</sup> sodium alginate.

## 5.3 Electrophoretic deposition of ceramics using strong polyelectrolytes

The common difficulties related to electrodeposition of strong polyelectrolytes, such as poly (vinylbenzyl trimethyl ammonium chloride) PVT, are related to their pH-independent charge and mutual molecular repulsion at the electrode. We suggested that such difficulties can be avoided in the electrodeposition of PVT composites with oxide or hydroxide materials. Oxide particles can be deposited by EPD [135-137] or by electrosynthesis [138-140]. The objective of our investigation was electrodeposition of PVT-zirconia composites, using combined electrochemical strategies, based on EPD and electrosynthesis. The charge compensation mechanism has been developed, which allowed efficient co-deposition of PVT and zirconia at high deposition rates. The results provide a strategy for electrodeposition of various new composites for applications based on the functional properties of polyelectrolytes and co-deposited materials.

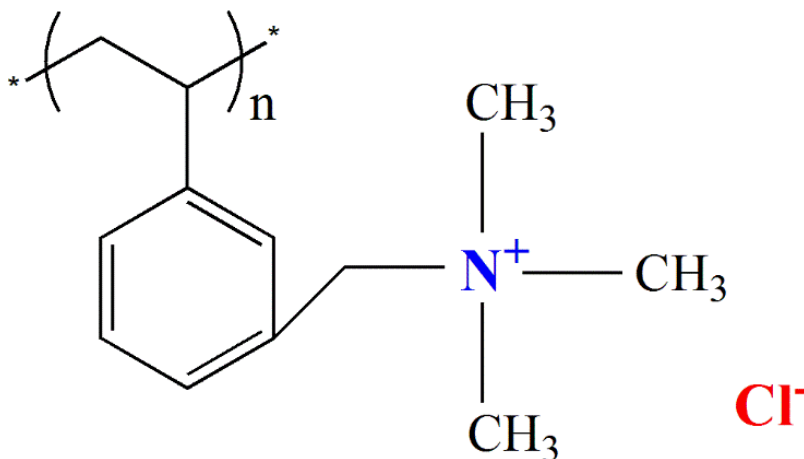
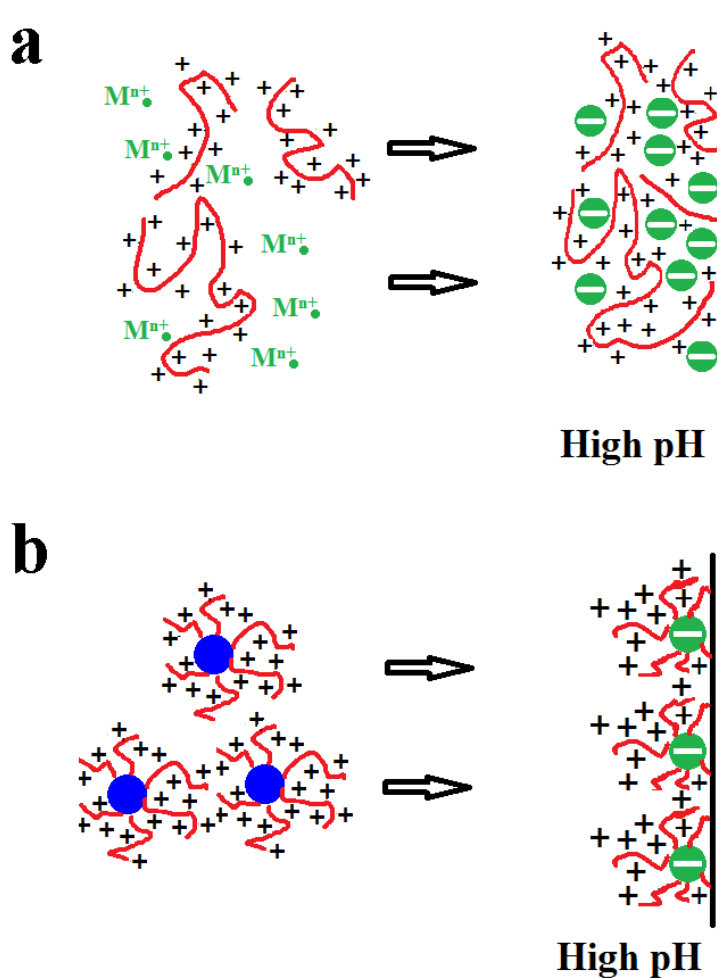


Figure 5-31 Chemical structure of PVT.

The chemical structure of PVT (Fig.5-31) includes aromatic monomers, containing charged  $N^+C_3H_9$  ligands with pH independent charge. The electrodeposition of PVT, presented difficulties related to mutual molecular repulsion at the electrode. Fig.5-32 illustrates two electrochemical mechanisms, which have been designed for the deposition of PVT-zirconia films.



**Figure 5-32 Electrodeposition mechanisms, combining EPD of PVT and (a) electrosynthesis or (b) EPD of zirconia.**

The first strategy was based on electrophoresis of PVT and electrosynthesis of zirconia (Fig.5-32a). The dissociation of  $ZrOCl_2$  resulted in the formation of cationic species, which electromigrated to the cathode and formed zirconia particles in high pH conditions at the cathode. The electrosynthesis of zirconia particles involved the interaction of zirconium species in the solutions with  $OH^-$  ions, formed in the reduction reaction [1]. It is known (22) that the pH of the zirconia isoelectric point is 5.6-7.2. Therefore, the zirconia particles, formed by electrosynthesis at the cathode, were negatively charged. Electrophoresis resulted in the migration of cationic PVT to the electrode surface. The electrostatic interactions of positively charged PVT and negatively charged zirconia promoted deposit formation.

The second strategy (Fig.5-32b) involved the adsorption of PVT on zirconia particles, prepared by chemical precipitation. In this case the zirconia suspensions were used with pH close to the isoelectric point of zirconia. The adsorbed cationic PVT provided electrosteric dispersion of zirconia. The zirconia particles, containing adsorbed PVT, as well as free PVT accumulated at the electrode surface by the electrophoretic transport. In the high pH conditions at the cathode surface the zirconia particles acquired a negative charge, which compensated a positive charge of PVT.

In both strategies, the co-deposition enhanced the deposition of individual components and the deposition efficiency was dependent on the relative amounts of zirconia and PVT components. The experimental data presented below provide proof of concepts and show the feasibility of electrodeposition of PVT-zirconia composites.

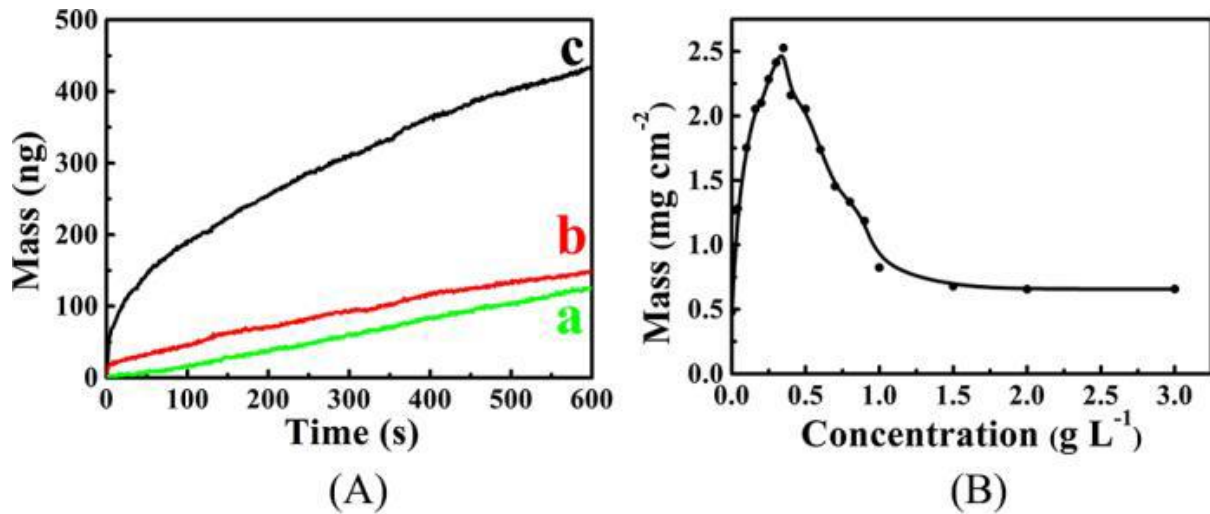


**Figure 5-33 (A) Time dependence of QCM mass gain for deposition from solutions, containing (a) 0.7 mM  $\text{ZrOCl}_2$ , (b) 0.05 g/L PVT, (c) 0.7 mM  $\text{ZrOCl}_2$  and 0.05 g/L PVT at a cell voltage of 5 V, (B) deposit mass versus PVT concentration in 5 mM  $\text{ZrOCl}_2$  solutions at a current density of  $10 \text{ mA cm}^{-2}$  and a deposition time of 5 min.**

The QCM data obtained in dilute solutions showed that the electrodeposition yields from the pure PVT and  $\text{ZrOCl}_2$  solutions was low Fig.5-33A (a, b) due to the mutual electrostatic repulsion of positively charged PVT or negatively charged zirconia, formed in the electrode reactions. However, the co-deposition of both materials resulted in the deposition yield (Fig.5-33A(c)) increase in agreement with the suggested deposition mechanism (Fig.5-32a). Electrodeposition has also been performed in the solutions of higher concentrations, where the  $\text{ZrOCl}_2$  concentration was 5 mM and PVT concentration was 0-3  $\text{g L}^{-1}$ . The yield of deposition (Fig.5-33B) increased with PVT concentration, showed a maximum at 0.35  $\text{g L}^{-1}$  and then gradually decreased. We suggested that the addition of positively charged PVT to the solutions

allowed for compensation of the negative charge of zirconia, electrosynthesized at the electrode and allowed for the formation of a composite (Fig.5-32A). However, further addition of PVT to the solutions led to the accumulation of PVT at the electrode, which blocked the electro-synthesis of zirconia in the electrode reactions. As a result, the deposition yield decreased at PVT concentrations above  $0.35 \text{ g L}^{-1}$ .

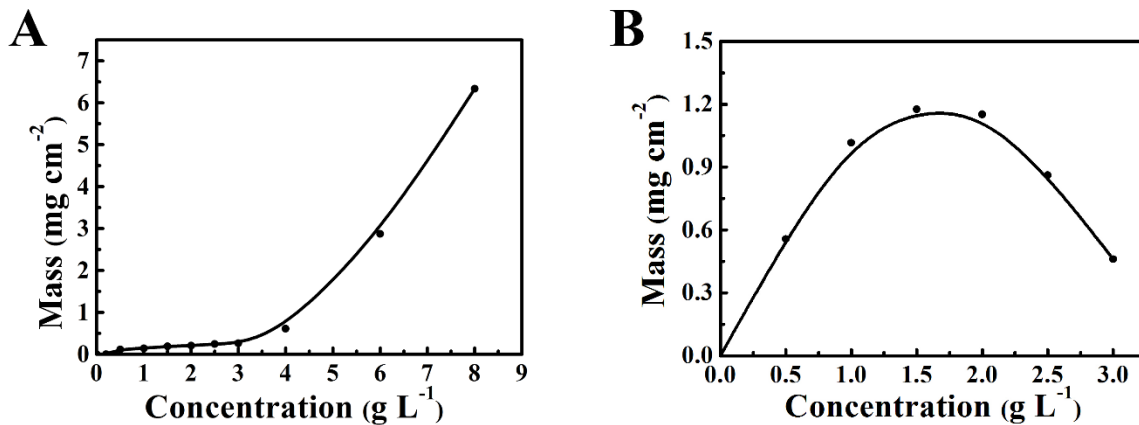


**Figure 5-34 Deposit mass versus (A) zirconia concentration in  $0.5 \text{ g L}^{-1}$  PVT solutions and (B) versus PVT concentration in  $4 \text{ g L}^{-1}$  zirconia solutions at a deposition voltage of  $100 \text{ V}$  and deposition time of  $5 \text{ min}$ .**

The addition of zirconia particles to the PVT solutions led to increased deposit mass (Fig.5-34A), especially in the zirconia concentration of  $4\text{-}8 \text{ g L}^{-1}$ , indicating co-deposition of both materials. We did not observe deposition of zirconia from pure zirconia suspensions. The addition of PVT to the zirconia allowed electrosteric stabilization and charging of the zirconia particles. The mass of the deposits increased with concentration increase of PVT in the zirconia suspensions (Fig.5-34B), exhibited a maximum at  $\sim 1.6 \text{ g L}^{-1}$  and decreased at higher PVT concentrations. Such

decrease resulted from increased concentration of PVT at the electrode surface and enhanced electrostatic repulsions.

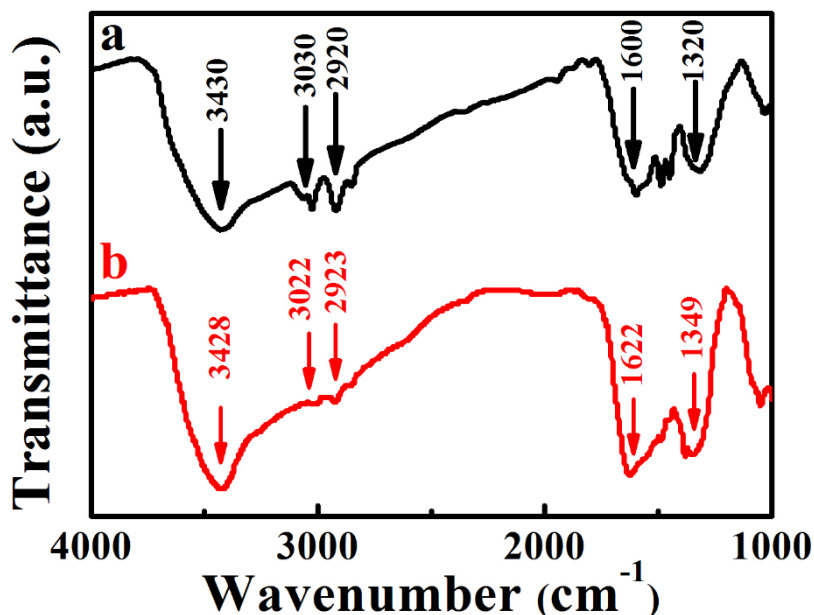


**Figure 5-35 FTIR spectra of deposits, prepared from (a) 5 mM  $ZrOCl_2$  solutions, containing  $0.35\text{ g L}^{-1}$  PVT at a current density of  $10\text{ mA cm}^{-2}$  and (b)  $6\text{ g L}^{-1}$  zirconia solutions, containing  $0.5\text{ g L}^{-1}$  PVT at a deposition voltage of 100 V.**

The co-deposition of PVT and zirconia was confirmed by FTIR, TGA and DTA studies. Fig.5-35 shows FTIR spectra of the composite materials, prepared by two methods. The broad absorptions at  $1320\text{ cm}^{-1}$  (Fig.5-35a) and  $1349\text{ cm}^{-1}$  (Fig.5-34b) resulted from hydroxyl stretching[141] of hydrous zirconia. The broad peaks at  $1600\text{ cm}^{-1}$  (Fig. 5-34a) and  $1622\text{ cm}^{-1}$  (Fig.5-35b) resulted from the C—C stretching vibrations [77] of aromatic ring of PVT. The absorptions at  $2920$  and  $3030\text{ cm}^{-1}$  (Fig.5-35a) and  $2923\text{ cm}^{-1}$  (Fig.5-34b) can be attributed to

—CH<sub>2</sub> and —CH<sub>3</sub> stretching vibrations [141] of PVT. The broad peaks at 3430 cm<sup>-1</sup> (Fig.5-35a) and 3428 (Fig.5-35b) resulted from stretching of OH groups of adsorbed water [77].

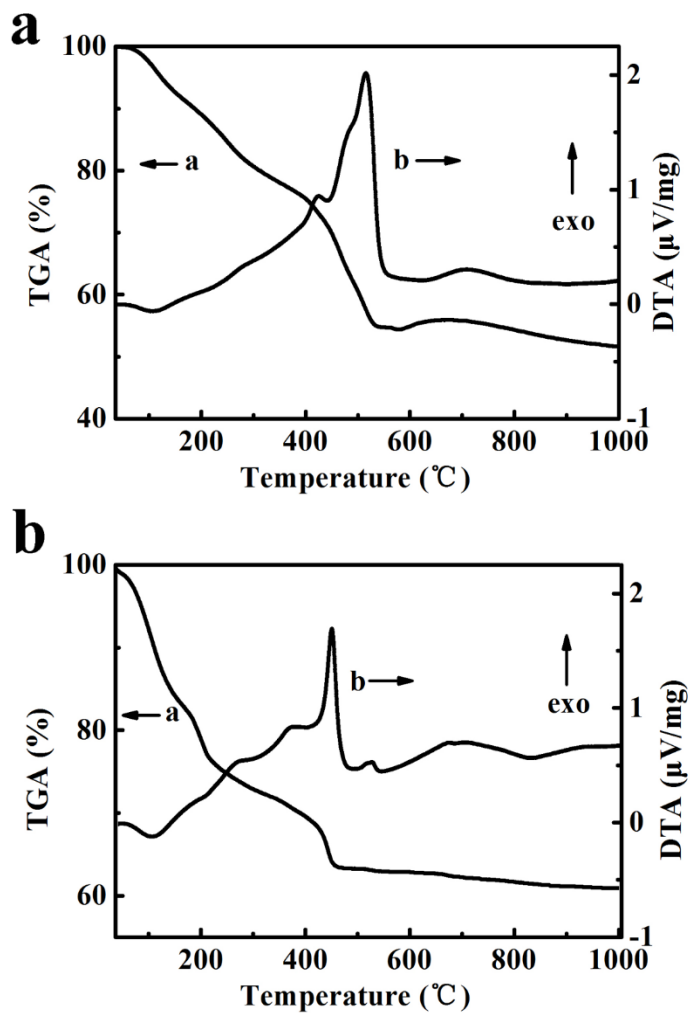


**Figure 5-36 (a) TGA and (b) DTA data for deposits, prepared from (A) 5 mM ZrOCl<sub>2</sub> solutions, containing 0.35 g L<sup>-1</sup> PVT and (B) 6 g L<sup>-1</sup> zirconia solutions, containing 0.5 g L<sup>-1</sup> PVT.**

Fig.5-36 shows TGA and DTA data for the composite materials. The mass loss in the TGA data resulted from burning out of PVT and dehydration of hydrated zirconia. The loss of mass at temperature of 1000 °C was 48% (Fig.5-36a) and 41% (Fig.5-36b), respectively. The remaining mass was related to the dehydrated zirconia. The exothermic peaks at ~450-500 °C were observed due to burning out of PVT.

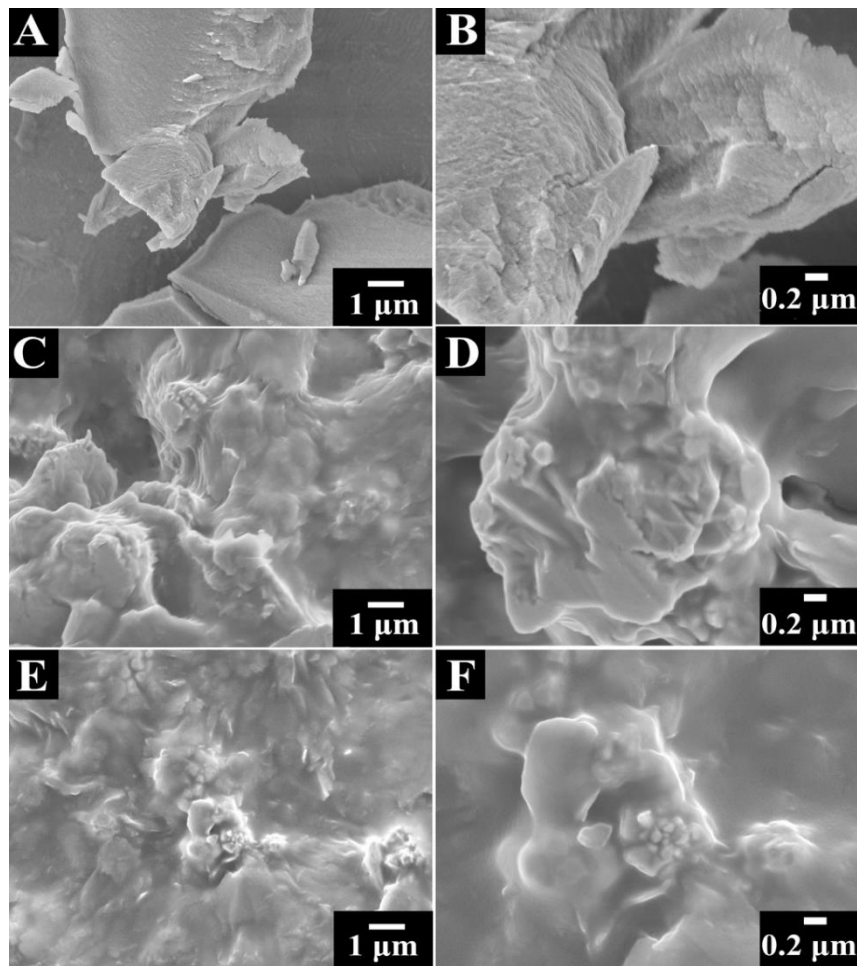


**Figure 5-37 SEM images at different magnifications of deposits, obtained from 5 mM  $ZrOCl_2$  solutions, containing (A, B) 0.35, (C, D) 0.7 and (E, F) 0.9 g L<sup>-1</sup> PVT at a current density of 10 mA cm<sup>-2</sup>.**

Fig.5-37 shows SEM images of the films prepared by a method, involving the electrosynthesis of zirconia and EPD of PVT. The films, prepared from 5 mM solutions of  $ZrOCl_2$ , containing  $0.35 \text{ g L}^{-1}$  PVT showed significant cracking and contained large agglomerated particles (Fig.5-37A, B). Crack free films (Fig.5-37C) were obtained from 5 mM solutions of  $ZrOCl_2$ , containing  $0.7 \text{ g L}^{-1}$  PVT. The films showed zirconia particles in the polymer matrix. Some particles formed agglomerates with PVT, as it is illustrated by the SEM image at higher magnification (Fig.5-37D). The increase in the PVT concentration to  $0.9 \text{ g L}^{-1}$  allowed the crack-free films with reduced agglomeration (Fig.5-37E, F). The composite films, prepared from zirconia suspensions, containing  $1 \text{ g L}^{-1}$  PVT, showed a crack-free microstructure with zirconia nanoparticles in the PVT matrix. Film prepared at higher zirconia concentrations mainly contained zirconia particles with small pores, related to particle packing. The PVT provided binding of the PVT particles. The co-deposition strategies, based on EPD and electrosynthesis can be beneficial for electrodeposition of various composites, utilizing properties of strong polyelectrolytes and inorganic materials.

In summary, electrodeposition mechanisms have been developed for the fabrication of PVT-zirconia composites, involving EPD of PVT and EPD or electrosynthesis of zirconia. The mechanisms are based on the charge compensation and heterocoagulation of positively charged PVT and negatively charged zirconia particles. The co-deposition mechanisms allowed for enhanced deposition of individual components. The film mass, composition and microstructure can be varied and optimized by changing the deposition conditions. In the proposed approach the problems related to the electrostatic repulsion of PVT and deposit formation can be avoided. The

results open a strategy to the deposition of other composites, containing strong polyelectrolytes and nanoparticles of inorganic material.

## 5.4 Electrophoretic deposition of quaternized hydroxyethylcellulose ethoxylate and composite materials.

Quaternized hydroxyethylcellulose ethoxylate (HCE) is a promising material for the fabrication of composite organic-inorganic coatings by EPD due to electric charge and excellent film forming properties of this material. Fig.5-38 shows the chemical structure of HCE, which has cationic groups.

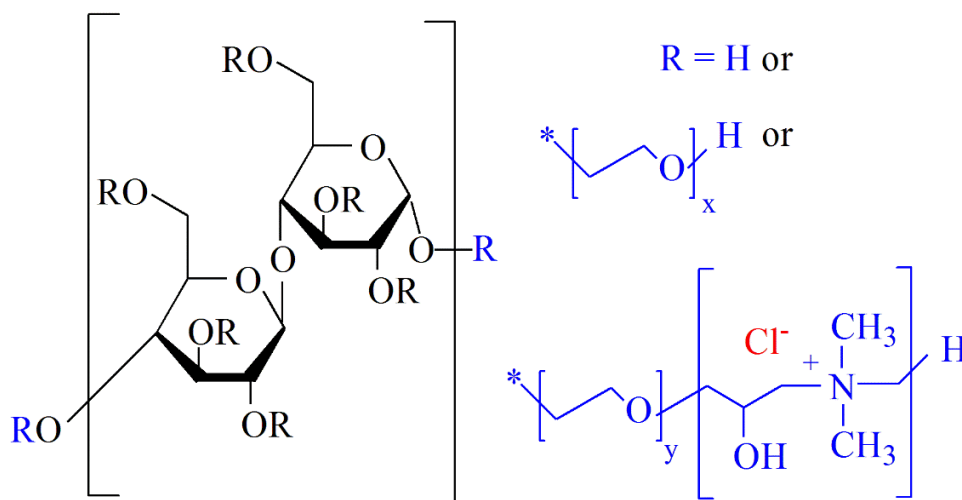
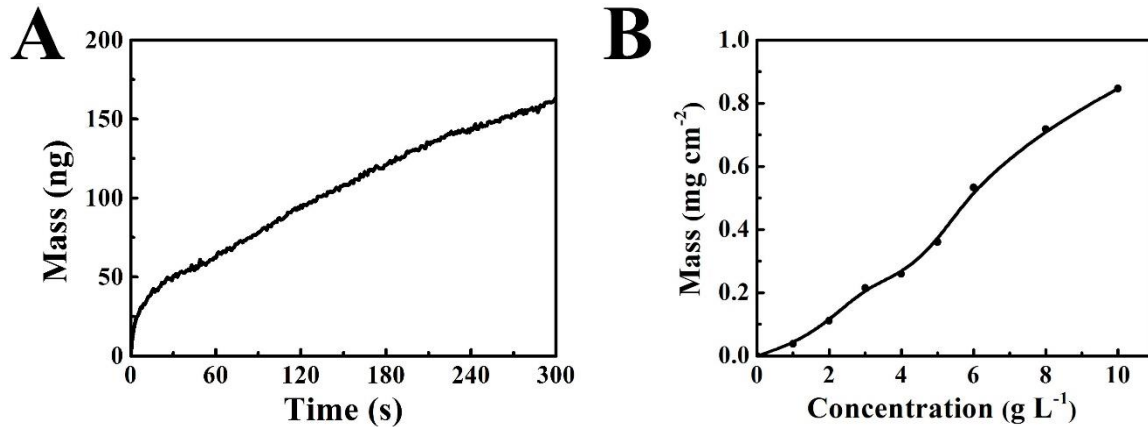


Figure 5-38 Chemical structure of HCE.



**Figure 5-39 (A) Time dependence of QCM mass gain for deposition from 0.05 g/L HCE solution at a cell voltage of 5V (B) Deposit mass versus HCE concentration in pure HCE solutions at a voltage of 30V and a deposition time of 5 min.**

It was found that HCE can be deposited by the cathodic EPD method. The kinetics of the deposition process was studied by the QCM method (Fig.5-39A). The deposit mass increased with increasing deposition time at a constant voltage, indicating the possibility of controlled deposition of films of different mass and different thickness. The deposition yield increased with increasing concentration of HCE in the solutions, as shown in the Fig.5-39B. Therefore, the deposit mass can also be varied and controlled by the variation of HCE concentration in the solutions.

It was found that HCE can be used as efficient charging, dispersing, binding and film forming agent for the EPD of materials of different types, including individual oxides, such as TiO<sub>2</sub> (rutile), complex oxide compounds such as Al<sub>2</sub>TiO<sub>5</sub>, MWCNT and hydrotalcite clay. The use of HCE allowed for the fabrication of stable suspensions. The deposition yield increased with increasing deposition time (Fig.5-40A). However, relatively low deposit yield was achieved for

$\text{Al}_2\text{TiO}_5$ , CNT and hydrotalcite. It was found that the deposition yield can be enhanced using gallocyanine as a dispersing agent (Fig.5-40B). The adsorption of gallocyanide on the particle surface resulted from the complexation of metal atoms on the particle surface with catechol group of gallocyanine. Fig.5-41 shows SEM images of the deposits, prepared by EPD. The images of the deposits show inorganic particles in the polymer matrix and confirm co-deposition of materials.

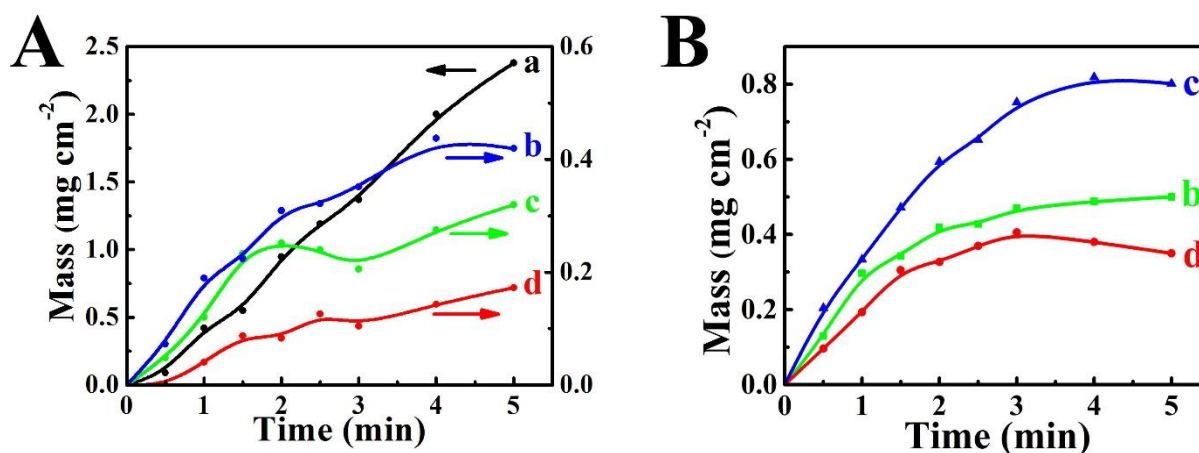


**Figure 5-40** Deposit mass versus time for deposits prepared from (A) 2 g L<sup>-1</sup> HCE solutions, containing 4 g L<sup>-1</sup> (a) rutile, (b) Al<sub>2</sub>TiO<sub>5</sub>, (c) hydrotalcite and (d) CNT (B) 2 g L<sup>-1</sup> HCE and 0.5 g L<sup>-1</sup> gallocyanine solutions, containing 4 g L<sup>-1</sup> (b) Al<sub>2</sub>TiO<sub>5</sub>, (c) hydrotalcite and (d) CNT.

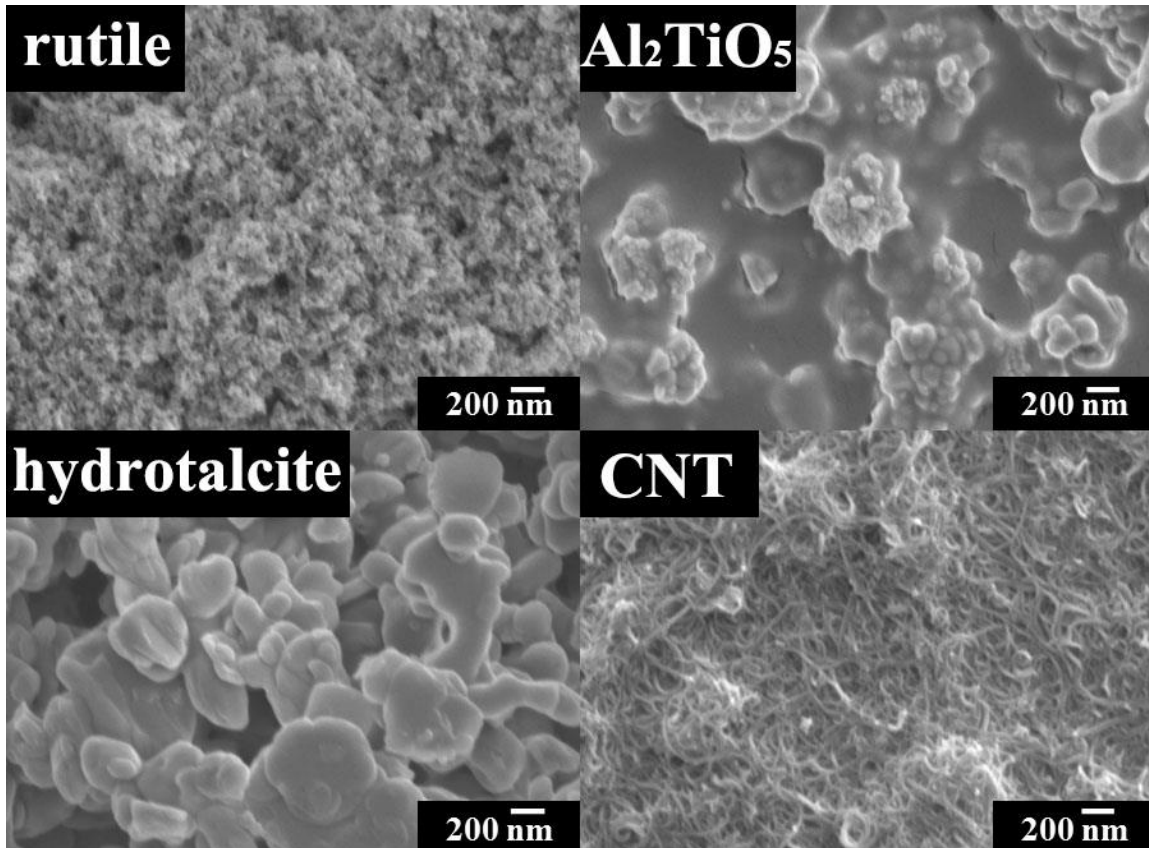


**Figure 5-41 SEM images of deposits, prepared from 2 g L<sup>-1</sup> HCE solutions, containing 4 g L<sup>-1</sup> rutile, Al<sub>2</sub>TiO<sub>5</sub>, hydrotalcite and CNT.**

In summary, we developed composite materials using HCE as a charging, dispersing and film forming agent. HCE can be deposited as individual material or co-deposited with other materials to form composites. The deposition yield and film morphology can be varied. Enhanced deposition yield can be achieved using gallocyanine as a disespant.

## 5.5 Fabrication of PPy-MWCNT composites

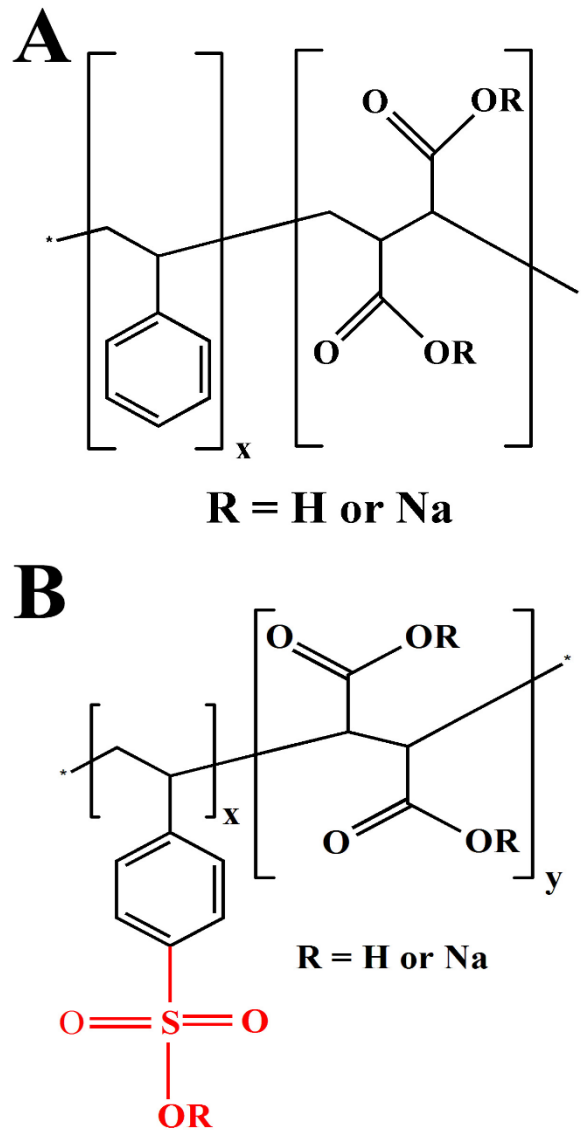
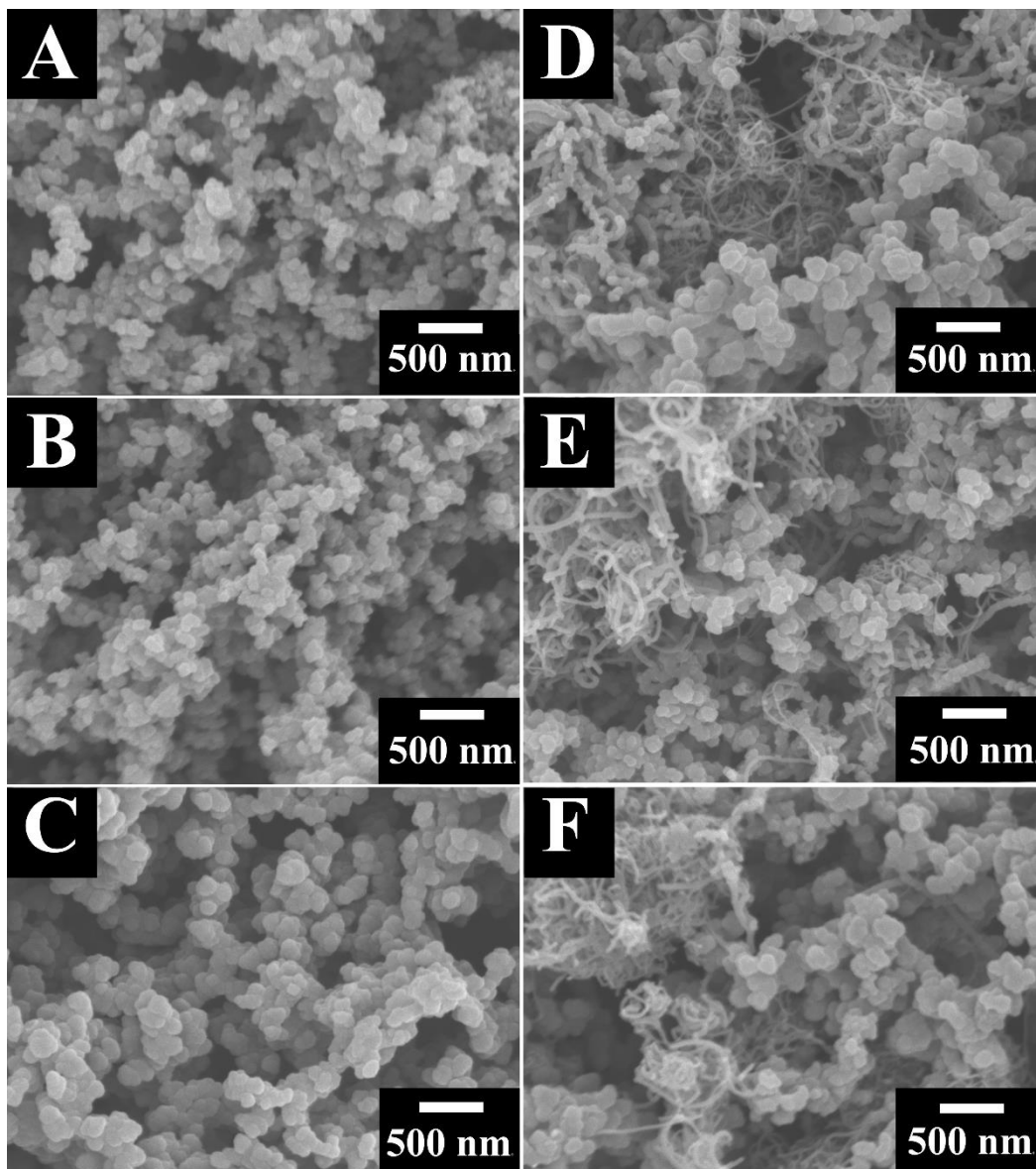


**Figure 5-42 Chemical structure of (A) PMSS and (B)PMSS-SR11 or PMSS-SR31.**

PMSS and poly(4-styrenesulfonic acid-*co*-maleic acid) sodium salt with 4-styrenesulfonic acid:maleic acid mole ratio of 1:1 (PMSS –SR11 ) and 3:1 (PMSS –SR31 ) were used for the

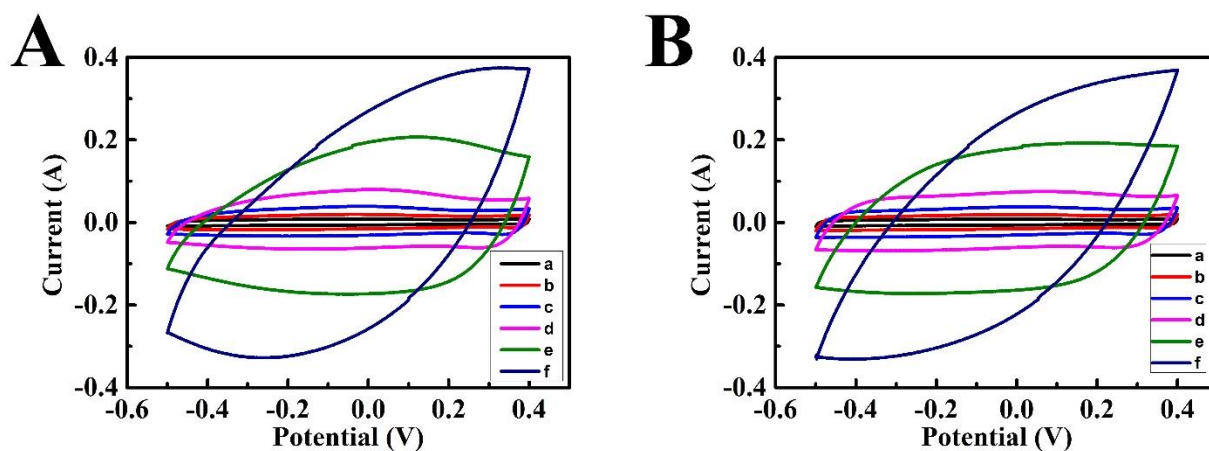
fabrication of polypyrrole (PPy) –MWCNT composites. In this approach the anionic polymers were used as anionic dopants for PPy polymerization and dispersants for MWCNT. PPy is important energy storage material for supercapacitors. The use of MWCNT as an additive is important for the fabrication of composites with improved electronic conductivity. Fig. 5-42 shows chemical structures of the polymers. The charge of PMSS is attributed to  $\text{COO}^-$  groups. The charge of PMSS –SR11 and PMSS –SR31 is attributed to  $\text{COO}^-$  and  $\text{SO}_3^-$  groups. The comparison of experimental data for PMSS, PMSS –SR11 and PMSS –SR31 provided an insight into the influence of charged groups on the performance of the composite materials.

Fig.5-43 shows SEM images of the materials prepared by chemical polymerization. The SEM images of pure PPy powders shows particles with particle size on the nanometric scale. The powders showed low agglomeration. The small particle size and low agglomeration are important for supercapacitor applications, because such morphology allows for good electrolyte access to the active material, which is prerequisite for high capacitance. The SEM images of powders, prepared in the presence of MWCNT showed nanoparticles of PPy and MWCNT.



**Figure 5-43 SEM images of PPy prepared (A, B, C) without MWCNTs and (D, E, F) in the presence of MWCNTs. (A, D), (B, E) and (C, F) were prepared in the presence of PMSS, PMSS-SR11 and PMSS-SR31, respectively.**

Figs.5-44-5-46 provide a summary of CV data for PPy and PPy-MWCNT materials prepared using different polymers. The active mass loading of the electrodes was  $20 \text{ mg cm}^{-2}$ . The relatively high active mass loading is important for practical applications in supercapacitor devices. The CVs showed nearly box shape at low scan rates, indicating nearly ideal capacitive behavior in a voltage window of  $-0.5$ - $+0.4$ V. However, significant deviation from the ideal box shape was observed at a scan rate of  $100 \text{ mV s}^{-1}$  due to poor electrolyte access to the active material.



**Figure 5-44** CVs at scan rates of (a) 2, (b) 5, (c)10, (d)20, (e)50, (f)100  $\text{mV s}^{-1}$ , for mass loading  $\sim 20 \text{ mg cm}^{-2}$  (A) pure PPy electrodes and (B) PPy/MWCNT composite electrodes doped with PMSS.

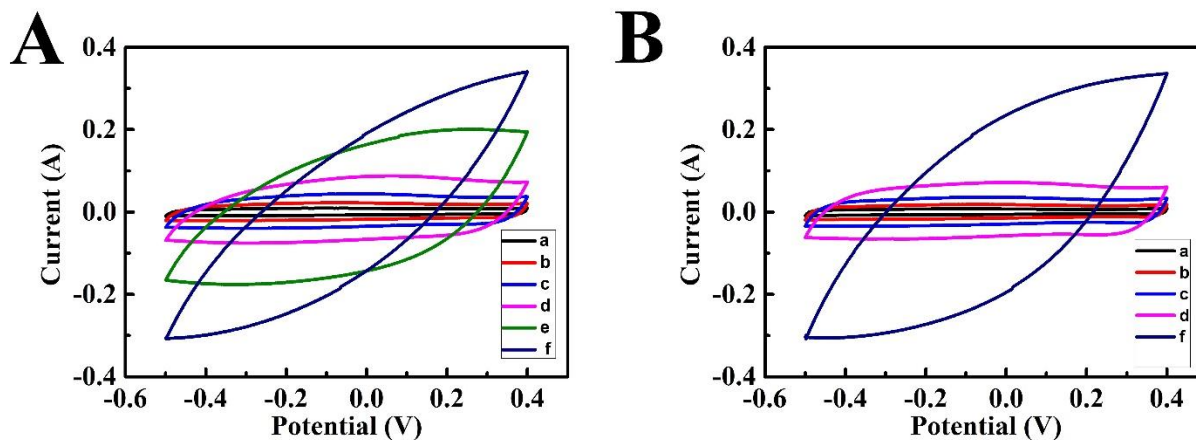


Figure 5-45 CVs at scan rates of (a) 2, (b) 5, (c) 10, (d) 20, (e) 50, (f) 100  $\text{mV s}^{-1}$ , for mass loading  $\sim 20 \text{ mg cm}^{-2}$  (A) pure PPy electrodes and (B) PPy/MWCNT composite electrodes doped with PMSS-SR11.

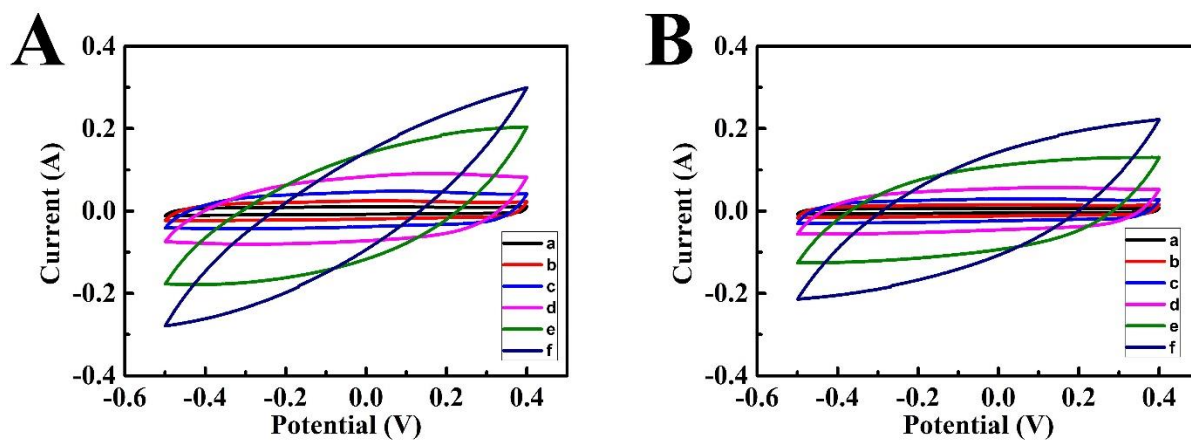
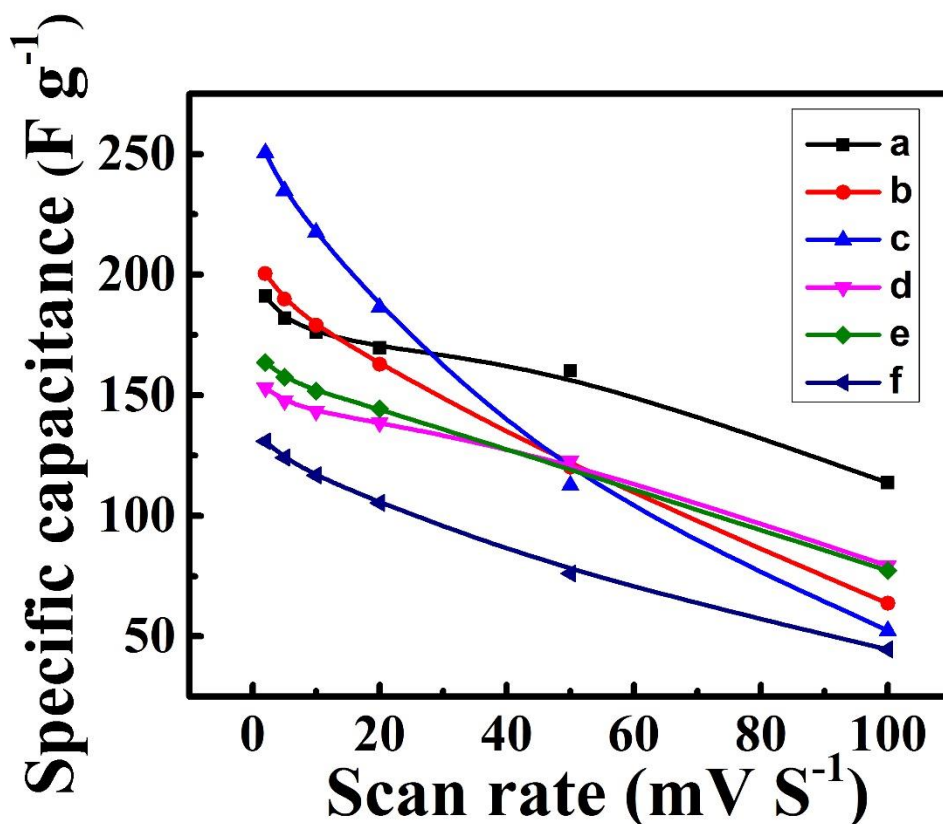


Figure 5-46 CVs at scan rates of (a) 2, (b) 5, (c) 10, (d) 20, (e) 50, (f) 100  $\text{mV s}^{-1}$ , for mass loading  $\sim 20 \text{ mg cm}^{-2}$  (A) pure PPy electrodes and (B) PPy/MWCNT composite electrodes doped with PMSS-SR31.



**Figure 5-47 Cs vs. scan rate of ES electrodes, prepared with pure PPy powders doped with (a) PMSS, (b) PMSS-SR11, (c) PMSS-SR11, and PPy/MWCNT composite materials with PPy/MWCNT mass ratio of 4:1, doped with (d) PMSS, (e) PMSS-SR11 and (f) PMSS-SR31, at**

In Fig.5-47, the PPy electrodes, prepared using PMSS–SR31 as a dopant showed the highest capacitance of 250 F g<sup>-1</sup> at a scan rate of 2 mV s<sup>-1</sup>. However, the capacitance decreased drastically with increased scan rate due to the poor electronic and ionic conductivities of the active material. The results indicated that PPy electrodes prepared using PMSS–SR31 dopant with larger number of SO<sub>3</sub><sup>-</sup> groups showed improved performance at low scan rates. However, the use of

PMSS dopant allowed for improved capacitance retention at high scan rates and significantly higher capacitance at high scan rates. The PPy-MWCNT electrodes showed reduced capacitance at low scan rates due to low capacitance of MWCNT. However, the use of MWCNT allowed for enhanced capacitance at high scan rates and improved capacitance retention for PMSS-SR11 and PMSS-SR31 based PPy materials.

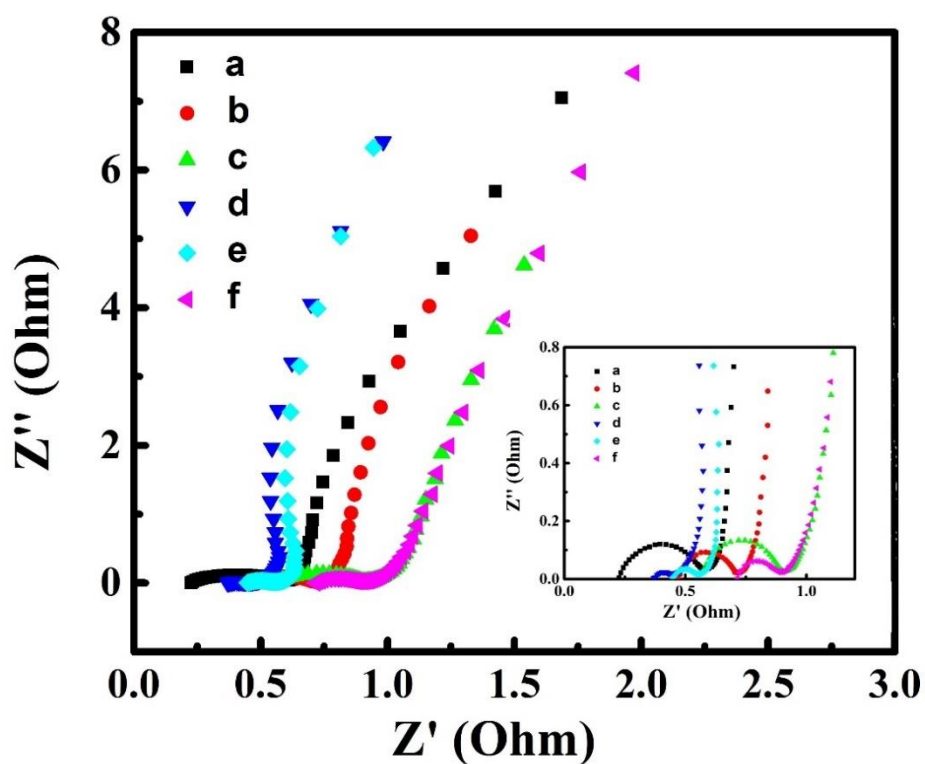


**Figure 5-48** Nyquist plot of  $Z^*$  (inset shows high frequency range) for ES electrodes, prepared with pure PPy powders doped with (a) PMSS, (b) PMSS-SR11, (c) PMSS-SR31, and PPy/MWCNT composite materials with PPy/MWCNT mass ratio of 4:1, doped with (d) PMSS, (e) PMSS-SR11 and (f) PMSS-SR31, at electrode mass loading of  $\sim 20 \text{ mg cm}^{-2}$ .

The analysis of the impedance data presented in the Nyquist plots showed relatively low resistance  $Z'=R$  (Fig.5-46). The low radius of the semicircles (Fig.5-46, inset) indicate low contact resistance of the electrodes. The composite electrodes, containing MWCNT showed reduced resistance, compared to the resistance of pure PPy. The difference is attributed to higher conductivity of MWCNT. The investigated materials are promising for application in supercapacitor devices.

In summary, new dopants such as PMSS, PMSS-SR11 and PMSS-SR31 were used for the synthesis of PPy and fabrication of PPy-MWCNT composites. The electrodes showed good electrochemical performance and can be used for practical applications in supercapacitors. The use of polymer with  $\text{SO}_3^-$  groups allowed for enhanced capacitance at low scan rates, however, the PMSS polymer with  $\text{COO}^-$  groups allowed for improved capacitance retention at high scan rates and higher capacitance at high scan rates. The use of MWCNT allowed for improved capacitance retention and lower resistance of the composites.

## Chapter 6 Conclusions

This research resulted in the development of novel composites, which exhibited advanced functional properties. New scientific and engineering contribution of this work to colloidal nanotechnology included the development of advanced chelating dispersing agents, such as different small organic molecules and chelating polymers. The unique feature of such dispersion agents is their strong adsorption on the surface of different materials, which allows superior dispersion. The chelating monomers of chelating polymers, such as PAZO and PMSS provided multiple adsorption sites for bonding to metal atoms on the particles surface. We analyzed and developed new fundamental adsorption and dispersion mechanisms. An important finding was the possibility of co-dispersion and co-deposition of advanced materials of different types using universal dispersing agents and formation of composites by EPD method.

It was found that CA can be used as an efficient dispersing agent for the synthesis of ZnO nanorods of reduced size and a dispersing agent for the EPD of ZnO films. In another strategy chelating BiqCOOK molecules were utilized for the efficient dispersion and EPD. We discovered film forming and dispersion properties of such molecules and developed a deposition mechanism. Another important achievement of this work was the application of tannic acid as an efficient capping and dispersing agent for synthesis and EPD of inorganic materials and composites. An important discovery was the use of lauryl gallate dispersant as a reducing agent for the synthesis of AgNp and a vehicle for particle dispersion and extraction in the liquid-liquid extraction method.

Further advancements in our new technologies allowed us to develop composite films using anodic EPD using weak polyelectrolytes, such as alginate. The composite coatings exhibited protective and flame retardant properties. We analyzed the deposition mechanisms and kinetics as well as microstructure of the coatings prepared at different conditions.

We have developed electrochemical strategies for the deposition of composites, based on strong polyelectrolytes. The approach is based on the EPD of the polyelectrolyte molecules and electrosynthesis of EPD of ceramic particles. The electrostatic heterocoagulation mechanism was proposed for the deposit formation. We investigated the deposition kinetics, composition and microstructure of the composites prepared by the new strategies. The new electrochemical strategies can be used for the deposition of other composites, based on functional polymers with pH independent charge.

We discovered a possibility of EPD of HCE films and developed electrochemical strategies for deposition of composites. It was found that HCE can be used as a multifunctional dispersing agent for deposition of different materials and a film forming agent.

New methods have been developed for the chemical synthesis of PPy based composites, using PMSS, PMSS–SR11 and PMSS–SR31 as anionic dopants for chemical polymerization and dispersants for MWCNT. The composites showed promising performance for application in electrodes of electrochemical supercapacitors. Good electrochemical performance was achieved at high active mass loadings. The electrodes showed high capacitance, large voltage window and low impedance. The analysis of electrochemical testing results and chemical structure of PMSS,

PMSS–SR11 and PMSS–SR31 provided an insight into the influence of the anionic functional groups on the capacitance and capacitance retention a high charge-discharge rates.

## Chapter 7 Future work

The performed research provided a scientific foundation for the further development of new dispersing and film forming agents for colloidal nanotechnology. It is expected that CA, tannic acid and BiqCOOH can be used as capping agents for the synthesis of various functional materials, their dispersion and EPD. Our results indicate that search for advanced capping and dispersing agents for nanotechnology must be focused on charged molecules with chelating groups. Of particular importance is the use of chelating polymers as dispersing and film forming agents. The chelating polymers show significantly stronger adsorption on various materials, compared to small organic molecules, containing a single chelating group. Further research in this direction will result in the development of various chelating polymers for application in synthesis of materials and colloidal nanotechnology.

The proof of concept studies of liquid-liquid extraction technology offers a new and unexplored route for the synthesis of nanoparticles of controlled size. In this approach, the problems related to particle agglomeration can be avoided. Therefore, future research must be directed towards the development of new chelating agents, which can be used as reducing agents and vehicles for dispersion and liquid-liquid extraction. Further investigation of materials from lauryl gallate family is a promising direction.

It is expected that further development of electrochemical techniques based on the use of strong and weak polyelectrolytes will result in advanced coatings, utilizing functional properties of polymers, inorganic materials, CNT and other functional materials. Of particular importance is

the heterocoagulation method based on the use of electrosynthesis of oxide particles and EPD of polymers. It is expected that the electrosynthesis of nanoparticles in the polymer matrix will allow the fabrication of non-agglomerated nanoparticles with reduced and controlled size. This method can be used for the polymer-mediated electrosynthesis of quantum dots.

Further development of new chemical strategies will result in the fabrication of composites for electrochemical energy storage, corrosion protection, flame retardant, optical and other functional applications. EPD offers an efficient tool in the fabrication of various materials for advanced applications.

## Bibliography

- [1] Series RL. EN-AVT-129. May; 2005.
- [2] Oriakhi C. Nano sandwiches. *Chemistry in Britain* 1998;34:59-62.
- [3] Arbatti M, Shan X, Cheng ZY. Ceramic-polymer composites with high dielectric constant. *Advanced Materials* 2007;19:1369-72.
- [4] Chen Y, Zhou S, Yang H, Wu L. Structure and properties of polyurethane/nanosilica composites. *Journal of applied polymer science* 2005;95:1032-9.
- [5] Vaessen DM, Ngantung FA, Palacio ML, Francis LF, McCormick AV. Effect of lamp cycling on conversion and stress development in ultraviolet - cured acrylate coatings. *Journal of applied polymer science* 2002;84:2784-93.
- [6] Vaessen D, McCormick A, Francis L. Effects of phase separation on stress development in polymeric coatings. *Polymer* 2002;43:2267-77.
- [7] Ajayan P. Nanotubes from carbon. *Chemical reviews* 1999;99:1787.
- [8] Thostenson ET, Ren Z, Chou T-W. Advances in the science and technology of carbon nanotubes and their composites: a review. *Composites science and technology* 2001;61:1899-912.
- [9] Lau AK-T, Hui D. The revolutionary creation of new advanced materials—carbon nanotube composites. *Composites Part B: Engineering* 2002;33:263-77.
- [10] Qian D, Dickey EC, Andrews R, Rantell T. Load transfer and deformation mechanisms in carbon nanotube-polystyrene composites. *Applied physics letters* 2000;76:2868-70.
- [11] Star A, Stoddart JF, Steuerma D, Diehl M, Boukai A, Wong EW, et al. Preparation and properties of polymer - wrapped single - walled carbon nanotubes. *Angewandte Chemie International Edition* 2001;40:1721-5.
- [12] Tang BZ, Xu H. Preparation, alignment, and optical properties of soluble poly (phenylacetylene)-wrapped carbon nanotubes. *Macromolecules* 1999;32:2569-76.
- [13] Kumar S, Dang TD, Arnold FE, Bhattacharyya AR, Min BG, Zhang X, et al. Synthesis, Structure, and Properties of PBO/SWNT Composites. *Macromolecules* 2002;35:9039-43.
- [14] Mitchell CA, Bahr JL, Arepalli S, Tour JM, Krishnamoorti R. Dispersion of functionalized carbon nanotubes in polystyrene. *Macromolecules* 2002;35:8825-30.
- [15] Hill DE, Lin Y, Rao AM, Allard LF, Sun Y-P. Functionalization of carbon nanotubes with polystyrene. *Macromolecules* 2002;35:9466-71.
- [16] Pang X, Zhitomirsky I. Electrophoretic deposition of composite hydroxyapatite-chitosan coatings. *Materials Characterization* 2007;58:339-48.
- [17] Zhitomirsky I. Cathodic electrodeposition of ceramic and organoceramic materials. *Fundamental aspects. Advances in colloid and interface science* 2002;97:279-317.
- [18] Boccaccini AR, Zhitomirsky I. Application of electrophoretic and electrolytic deposition techniques in ceramics processing. *Current Opinion in Solid State and Materials Science* 2002;6:251-60.
- [19] Gal - Or L, Silberman I, Chaim R. Electrolytic ZrO<sub>2</sub> coatings I. electrochemical aspects. *Journal of the Electrochemical Society* 1991;138:1939-42.
- [20] CHAIM R, ZHITOMIRSKY I, GAL-OR L, BESTGEN H. Electrochemical Al<sub>2</sub>O<sub>3</sub>-ZrO<sub>2</sub> composite coatings on non-oxide ceramic substrates. *Journal of Materials Science* 1997;32:389-400.
- [21] Zhitomirsky I. Electrolytic deposition of oxide films in the presence of hydrogen peroxide. *Journal of the European Ceramic Society* 1999;19:2581-7.

- [22] Zhitomirsky I. New developments in electrolytic deposition of ceramic films: Focus on Electronics. American Ceramic Society Bulletin 2000;79:57-63.
- [23] Hughes A, Taylor R, Hinton B, Wilson L. XPS and SEM characterization of hydrated cerium oxide conversion coatings. Surface and Interface Analysis 1995;23:540-50.
- [24] Sogami I, Ise N. On the electrostatic interaction in macroionic solutions. The Journal of chemical physics 1984;81:6320-32.
- [25] Zhitomirsky I. JOM-e Miner Met Mater Soc J 52; 2000.
- [26] Hamaker H. Formation of a deposit by electrophoresis. Transactions of the Faraday Society 1940;35:279-87.
- [27] Mizuguchi J, Sumi K, Muchi T. A highly stable nonaqueous suspension for the electrophoretic deposition of powdered substances. Journal of the Electrochemical Society 1983;130:1819-25.
- [28] Zhitomirsky I. Electrophoretic deposition of chemically bonded ceramics in the system CaO-SiO<sub>2</sub>-P<sub>2</sub>O<sub>5</sub>. Journal of materials science letters 1998;17:2101-4.
- [29] Harbach F, Nienburg H. Homogeneous functional ceramic components through electrophoretic deposition from stable colloidal suspensions—I. Basic concepts and application to zirconia. Journal of the European Ceramic Society 1998;18:675-83.
- [30] Russ BE, Talbot JB. An analysis of the binder formation in electrophoretic deposition. Journal of The Electrochemical Society 1998;145:1253-6.
- [31] Shane MJ, Talbot JB, Kinney BG, Sluzky E, Hesse K. Electrophoretic deposition of phosphors: II. Deposition experiments and analysis. Journal of colloid and interface science 1994;165:334-40.
- [32] Kaya C, Boccaccini A, Trusty P. Processing and characterisation of 2-D woven metal fibre-reinforced multilayer silica matrix composites using electrophoretic deposition and pressure filtration. Journal of the European Ceramic Society 1999;19:2859-66.
- [33] Moreno R, Ferrari B. Advanced ceramics via EPD of aqueous slurries. American Ceramic Society bulletin 2000;79:44-8.
- [34] Werway E, Overbeek JTG. Theory of Stability of Lyophobic Colloids Elsevier. Amsterdam-New York 1948:34.
- [35] Cao G. Synthesis, properties and applications: World Scientific; 2004.
- [36] Sarkar P, Nicholson PS. Electrophoretic deposition (EPD): mechanisms, kinetics, and application to ceramics. Journal of the American Ceramic Society 1996;79:1987-2002.
- [37] Chu X, Nikolov A, Wasan D. Thin liquid film structure and stability: The role of depletion and surface - induced structural forces. The Journal of chemical physics 1995;103:6653-61.
- [38] Zhitomirsky I, Gal-Or L. Electrophoretic deposition of hydroxyapatite. Journal of Materials Science: Materials in Medicine 1997;8:213-9.
- [39] Larsen AE, Grier DG. Like-charge attractions in metastable colloidal crystallites. Nature 1997;385:230-3.
- [40] Trau M, Saville D, Aksay I. Assembly of colloidal crystals at electrode interfaces. Langmuir 1997;13:6375-81.
- [41] Besra L, Liu M. A review on fundamentals and applications of electrophoretic deposition (EPD). Progress in materials science 2007;52:1-61.
- [42] Ennis J, Sjöström L, Åkesson T, Jönsson B. Surface interactions in the presence of polyelectrolytes. A simple theory. Langmuir 2000;16:7116-25.
- [43] Hoogeveen NG, Stuart MAC, Fleer GJ. Polyelectrolyte adsorption on oxides: I. Kinetics and adsorbed amounts. Journal of colloid and interface science 1996;182:133-45.

- [44] Hoogeveen NG, Stuart MAC, Fler GJ. Polyelectrolyte adsorption on oxides: II. Reversibility and exchange. *Journal of colloid and interface science* 1996;182:146-57.
- [45] Okubo T, Suda M. Absorption of polyelectrolytes on colloidal surfaces as studied by electrophoretic and dynamic light-scattering techniques. *Journal of colloid and interface science* 1999;213:565-71.
- [46] Dickinson E, Eriksson L. Particle flocculation by adsorbing polymers. *Advances in Colloid and Interface Science* 1991;34:1-29.
- [47] Van der Biest OO, Vandeperre LJ. Electrophoretic deposition of materials. *Annual Review of Materials Science* 1999;29:327-52.
- [48] Labib ME, Williams R. The use of zeta-potential measurements in organic solvents to determine the donor—acceptor properties of solid surfaces. *Journal of colloid and interface science* 1984;97:356-66.
- [49] Yamashita K, Nagai M, Umegaki T. Fabrication of green films of single-and multi-component ceramic composites by electrophoretic deposition technique. *Journal of materials science* 1997;32:6661-4.
- [50] Damodaran R, Moudgil B. Electrophoretic deposition of calcium phosphates from non-aqueous media. *Colloids and Surfaces A: Physicochemical and Engineering Aspects* 1993;80:191-5.
- [51] Zhitomirsky I. Cathodic electrophoretic deposition of diamond particles. *Materials Letters* 1998;37:72-8.
- [52] Kuwabara K, Sugiyama K, Ohno M. All-solid-state electrochromic device. 1. Electrophoretic deposition film of proton conductive solid electrolyte. *Solid state ionics* 1991;44:313-8.
- [53] Paik U, Hackley VA, Choi S-C, Jung Y-G. The effect of electrostatic repulsive forces on the stability of BaTiO<sub>3</sub> particles suspended in non-aqueous media. *Colloids and Surfaces A: Physicochemical and Engineering Aspects* 1998;135:77-88.
- [54] Zhitomirsky I, Petric A. Cathodic electrodeposition of polymer films and organoceramic films. *Materials Science and Engineering: B* 2000;78:125-30.
- [55] Dahotre NB, Sudarshan T. *Intermetallic and ceramic coatings*: CRC Press; 1999.
- [56] Jones SL, Norman CJ. Dehydration of hydrous zirconia with methanol. *Journal of the American Ceramic Society* 1988;71.
- [57] Zhitomirsky I. Cathodic electrosynthesis of titanium and ruthenium oxides. *Materials Letters* 1998;33:305-10.
- [58] Zhitomirsky I. Cathodic electrosynthesis of titania films and powders. *Nanostructured materials* 1997;8:521-8.
- [59] Kosmulski M, Durand-Vidal S, Gustafsson J, Rosenholm J. Charge interactions in semi-concentrated titania suspensions at very high ionic strengths. *Colloids and Surfaces A: Physicochemical and Engineering Aspects* 1999;157:245-59.
- [60] Andrews J, Collins A, Cornish D, Dracass J. The forming of ceramic bodies by electrophoretic deposition. *Proc Br Ceram Soc*1969. p. 211-29.
- [61] Siracuse JA, Talbot JB, Sluzky E, Hesse K. The adhesive agent in cataphoretically coated phosphor screens. *Journal of the Electrochemical Society* 1990;137:346-8.
- [62] Sarkar P, Huang X, Nicholson PS. Zirconia/alumina functionally graded composites by electrophoretic deposition techniques. *Journal of the American Ceramic Society* 1993;76:1055-6.
- [63] Chen C-Y, Chen S-Y, Liu D-M. Electrophoretic deposition forming of porous alumina membranes. *Acta materialia* 1999;47:2717-26.
- [64] Wiley B, Sun Y, Mayers B, Xia Y. Shape - controlled synthesis of metal nanostructures: the case of silver. *Chemistry—A European Journal* 2005;11:454-63.
- [65] Evanoff DD, Chumanov G. Size-controlled synthesis of nanoparticles. 2. Measurement of extinction, scattering, and absorption cross sections. *The Journal of Physical Chemistry B* 2004;108:13957-62.

- [66] Merga G, Wilson R, Lynn G, Milosavljevic BH, Meisel D. Redox catalysis on “naked” silver nanoparticles. *The Journal of Physical Chemistry C* 2007;111:12220-6.
- [67] Iravani S. Green synthesis of metal nanoparticles using plants. *Green Chemistry* 2011;13:2638-50.
- [68] Korbekandi H, Iravani S, Abbasi S. Production of nanoparticles using organisms. *Critical Reviews in Biotechnology* 2009;29:279-306.
- [69] Clayden J, Greeves N. s. Warren, P. Wothers. *Organic Chemistry* 2000.
- [70] Li J, Xie H, Li Y. Fabrication of graphene oxide/polypyrrole nanowire composite for high performance supercapacitor electrodes. *Journal of Power Sources* 2013;241:388-95.
- [71] Shi K, Zhitomirsky I. Polypyrrole nanofiber–carbon nanotube electrodes for supercapacitors with high mass loading obtained using an organic dye as a co-dispersant. *Journal of Materials Chemistry A* 2013;1:11614-22.
- [72] Shi K, Zhitomirsky I. Electrophoretic nanotechnology of graphene–carbon nanotube and graphene–polypyrrole nanofiber composites for electrochemical supercapacitors. *Journal of colloid and interface science* 2013;407:474-81.
- [73] Shi K, Zhitomirsky I. Fabrication of Polypyrrole-Coated Carbon Nanotubes Using Oxidant–Surfactant Nanocrystals for Supercapacitor Electrodes with High Mass Loading and Enhanced Performance. *ACS applied materials & interfaces* 2013;5:13161-70.
- [74] Xia H, Wang Q, Qiu G. Polymer-encapsulated carbon nanotubes prepared through ultrasonically initiated in situ emulsion polymerization. *Chemistry of materials* 2003;15:3879-86.
- [75] Wang G, Zhang L, Zhang J. A review of electrode materials for electrochemical supercapacitors. *Chemical Society Reviews* 2012;41:797-828.
- [76] Ramya R, Sivasubramanian R, Sangaranarayanan M. Conducting polymers-based electrochemical supercapacitors—progress and prospects. *Electrochimica Acta* 2013;101:109-29.
- [77] Zhang T, Wojtal P, Rubel O, Zhitomirsky I. Density functional theory and experimental studies of caffeic acid adsorption on zinc oxide and titanium dioxide nanoparticles. *RSC Advances* 2015;5:106877-85.
- [78] Deakin MR, Buttry DA. Electrochemical applications of the quartz crystal microbalance. *Analytical Chemistry* 1989;61:1147A-54A.
- [79] Sauerbrey G. Verwendung von Schwingquarzen zur Wägung dünner Schichten und zur Mikrowägung. *Zeitschrift für physik* 1959;155:206-22.
- [80] Taberna P, Simon P, Fauvarque J-F. Electrochemical characteristics and impedance spectroscopy studies of carbon-carbon supercapacitors. *Journal of The Electrochemical Society* 2003;150:A292-A300.
- [81] Ata M, Liu Y, Zhitomirsky I. A review of new methods of surface chemical modification, dispersion and electrophoretic deposition of metal oxide particles. *RSC Advances* 2014;4:22716-32.
- [82] Sedó J, Saiz - Poseu J, Busqué F, Ruiz - Molina D. Catechol - Based Biomimetic Functional Materials. *Advanced Materials* 2013;25:653-701.
- [83] Lee BP, Messersmith PB, Israelachvili JN, Waite JH. Mussel-inspired adhesives and coatings. *Annual review of materials research* 2011;41:99.
- [84] Lee H, Dellatore SM, Miller WM, Messersmith PB. Mussel-inspired surface chemistry for multifunctional coatings. *science* 2007;318:426-30.
- [85] Waite JH. Surface chemistry: mussel power. *Nature materials* 2008;7:8-9.
- [86] Li Q, Kumar V, Li Y, Zhang H, Marks TJ, Chang RP. Fabrication of ZnO nanorods and nanotubes in aqueous solutions. *Chemistry of Materials* 2005;17:1001-6.
- [87] Cheong M, Zhitomirsky I. Electrodeposition of alginic acid and composite films. *Colloids and Surfaces A: Physicochemical and Engineering Aspects* 2008;328:73-8.

- [88] Wang Y, Zhitomirsky I. Electrophoretic deposition of manganese dioxide– multiwalled carbon nanotube composites for electrochemical supercapacitors. *Langmuir* 2009;25:9684-9.
- [89] Liang F, Chen J, Cheng Y, Wang L, Ma D, Jing X, et al. Synthesis, characterization, photoluminescent and electroluminescent properties of new conjugated 2, 2' -(arylenedivinylene) bis-8-substituted quinolines. *Journal of Materials Chemistry* 2003;13:1392-9.
- [90] Khatkar S, Kumar R, Khatkar A, Taxak V. Synthesis, characterization, enhanced photoluminescence and biological activity of Eu (III) complexes with organic ligands. *Journal of Materials Science: Materials in Electronics* 2015;26:7086-95.
- [91] Baudin HB, Davidsson J, Serroni S, Juris A, Balzani V, Campagna S, et al. Ultrafast energy transfer in binuclear ruthenium-osmium complexes as models for light-harvesting antennas. *The Journal of Physical Chemistry A* 2002;106:4312-9.
- [92] Yurdakul Ş, Yurdakul M. Vibrational frequencies and structural determination of 2, 2' -biquinoline. *Journal of molecular structure* 2007;834:555-60.
- [93] Wills KA, Mandujano-Ramírez HJ, Merino G, Mattia D, Hewat T, Robertson N, et al. Investigation of a copper (i) biquinoline complex for application in dye-sensitized solar cells. *RSC Advances* 2013;3:23361-9.
- [94] Clark A, Wilkes E, Scollary G. Chemistry of copper in white wine: a review. *Australian Journal of Grape and Wine Research* 2015;21:339-50.
- [95] González P, Knochen M, Sasaki MK, Zagatto EA. Pulsed flows in flow analysis: Potentialities, limitations and applications. *Talanta* 2015;143:419-30.
- [96] Zhang Y-N, Liu J-Q, Wang T, Wen G-L, Yang G-P, Wang Y-Y, et al. Design and syntheses of two novel Mn (II) and Cu (II) complexes with 2, 2' -biquinoline-4, 4' -dicarboxylate and N-containing bidentate co-ligand. *Journal of Molecular Structure* 2008;878:116-23.
- [97] Kumar A, Buttry DA. Size-dependent anodic dissolution of water-soluble palladium nanoparticles. *The Journal of Physical Chemistry C* 2013;117:26783-9.
- [98] Rahim MA, Ejima H, Cho KL, Kempe K, Müllner M, Best JP, et al. Coordination-driven multistep assembly of metal–polyphenol films and capsules. *Chemistry of Materials* 2014;26:1645-53.
- [99] Shutava TG, Balkundi SS, Vangala P, Steffan JJ, Bigelow RL, Cardelli JA, et al. Layer-by-layer-coated gelatin nanoparticles as a vehicle for delivery of natural polyphenols. *ACS nano* 2009;3:1877-85.
- [100] Kim B-S, Lee H-i, Min Y, Poon Z, Hammond PT. Hydrogen-bonded multilayer of pH-responsive polymeric micelles with tannic acid for surface drug delivery. *Chemical Communications* 2009:4194-6.
- [101] Kozlovskaya V, Harbaugh S, Drachuk I, Shchepelina O, Kelley-Loughnane N, Stone M, et al. Hydrogen-bonded LbL shells for living cell surface engineering. *Soft Matter* 2011;7:2364-72.
- [102] Costa E, Coelho M, Ilharco LM, Aguiar-Ricardo A, Hammond PT. Tannic acid mediated suppression of PNIPAAm microgels thermoresponsive behavior. *Macromolecules* 2011;44:612-21.
- [103] Shutava T, Prouty M, Kommireddy D, Lvov Y. pH responsive decomposable layer-by-layer nanofilms and capsules on the basis of tannic acid. *Macromolecules* 2005;38:2850-8.
- [104] Aguirre FMA, Becerra RH. New synthesis of bismuth oxide nanoparticles Bi<sub>2</sub>O<sub>3</sub> assisted by tannic acid. *Applied Physics A* 2015;119:909-15.
- [105] Dutta A, Dolui SK. Tannic acid assisted one step synthesis route for stable colloidal dispersion of nickel nanostructures. *Applied Surface Science* 2011;257:6889-96.
- [106] Yi Z, Li X, Xu X, Luo B, Luo J, Wu W, et al. Green, effective chemical route for the synthesis of silver nanoplates in tannic acid aqueous solution. *Colloids and Surfaces A: Physicochemical and Engineering Aspects* 2011;392:131-6.
- [107] Kandori K, Nishizawa H, Fukusumi M, Morisada Y. Control of the Morphology and Porosity of Hematite Particles through the Use of Tannic Acids. *Adsorption Science & Technology* 2008;26:269-77.

- [108] Vigolo B, Coulon C, Maugey M, Zakri C, Poulin P. An experimental approach to the percolation of sticky nanotubes. *Science* 2005;309:920-3.
- [109] Vigolo B, Penicaud A, Coulon C, Sauder C, Paillet R, Journet C, et al. Macroscopic fibers and ribbons of oriented carbon nanotubes. *Science* 2000;290:1331-4.
- [110] Kim D-Y, Sung JS, Kim M, Ghodake G. Rapid production of silver nanoparticles at large-scale using gallic acid and their antibacterial assessment. *Materials Letters* 2015;155:62-4.
- [111] Yajima S, Iwane Y, Nomura E, Taniguchi H, Kimura K. Silver-ion redox sensing based on colloid formation by gallate ester derivatives. *Analytica chimica acta* 2006;556:189-94.
- [112] Xu H-N, Huang W-N, He C-H. Modeling for extraction of isoflavones from stem of *Pueraria lobata* (Willd.) Ohwi using n-butanol/water two-phase solvent system. *Separation and Purification Technology* 2008;62:590-5.
- [113] Xu H-N, He C-H. Extraction of isoflavones from stem of *Pueraria lobata* (Willd.) Ohwi using n-butanol/water two-phase solvent system and separation of daidzein. *Separation and Purification Technology* 2007;56:85-9.
- [114] Bag M, Chattopadhyay P, Basu S. Substoichiometric extraction of chromium (III) with 2-picolinic acid into n-butanol. *Journal of Radioanalytical and Nuclear Chemistry* 2013;295:1525-9.
- [115] Ibrahim YA, Asfour A-F-F, Abdel-Megid MH, Zatout AA. Liquid-liquid extraction of phosphoric acid from aqueous solutions in pulsed columns. *Separation science and technology* 1994;29:415-27.
- [116] Bosch-Jimenez P, Lira-Cantu M, Domingo C, Ayllón JA. Solution processable TiO<sub>2</sub> nanoparticles capped with lauryl gallate. *Materials Letters* 2012;89:296-8.
- [117] Džunuzović ES, Džunuzović JV, Marinković AD, Marinović-Cincović MT, Jeremić KB, Nedeljković JM. Influence of surface modified TiO<sub>2</sub> nanoparticles by gallates on the properties of PMMA/TiO<sub>2</sub> nanocomposites. *European Polymer Journal* 2012;48:1385-93.
- [118] Goldenberg LM, Lisinetskii V, Ryabchun A, Bobrovsky A, Schrader S. Influence of the cation type on the DFB lasing performance of dye-doped azobenzene-containing polyelectrolytes. *Journal of Materials Chemistry C* 2014;2:8546-53.
- [119] Maaland SA, Cai R, Fulghum T, Advincula RC. Adsorption of fibrinogen on polyionic azobenzene layer-by-layer film using photoisomerization. *Polymer Preprints* 2008;49:990.
- [120] Li N, Lu J, Li H, Kang E-T. Nonlinear optical properties and memory effects of the azo polymers carrying different substituents. *Dyes and Pigments* 2011;88:18-24.
- [121] Madruga C, Alliprandini Filho P, Andrade MM, Gonçalves M, Raposo M, Ribeiro PA. Birefringence dynamics of poly {1-[4-(3-carboxy-4-hydroxyphenylazo) benzenesulfonamido]-1, 2-ethanediyl, sodium salt} cast films. *Thin Solid Films* 2011;519:8191-6.
- [122] Ferreira Q, Gomes PJ, Raposo M, Giacometti J, Oliveira ON, Ribeiro PA. Influence of ionic interactions on the photoinduced birefringence of Poly [1-[4-(3-Carboxy-4 Hydroxyphenylazo) benzene sulfonamido]-1, 2-ethanediyl, sodium salt] films. *Journal of nanoscience and nanotechnology* 2007;7:2659-66.
- [123] Rmaile HH, Schlenoff JB. "Internal p K a's" in Polyelectrolyte Multilayers: Coupling Protons and Salt. *Langmuir* 2002;18:8263-5.
- [124] Ferreira Q, Ribeiro PA, Raposo M. Villain's fractal growth of poly [1-[4-(3-carboxy-4-hydroxyphenylazo) benzenesulfonamido]-1, 2-ethanediyl, sodium salt] J-aggregates onto layer-by-layer films and its effect on film absorbance spectrum. *Journal of Applied Physics* 2013;113:243508.
- [125] Payne GF, Raghavan SR. Chitosan: a soft interconnect for hierarchical assembly of nano-scale components. *Soft Matter* 2007;3:521-7.
- [126] Zhitomirsky I. Electrophoretic deposition of organic-inorganic nanocomposites. *Journal of materials science* 2006;41:8186-95.

- [127] Kiliaris P, Papaspyrides C. Polymer/layered silicate (clay) nanocomposites: an overview of flame retardancy. *Progress in Polymer Science* 2010;35:902-58.
- [128] Weil ED. Fire-protective and flame-retardant coatings-A state-of-the-art review. *Journal of fire sciences* 2011;29:259-96.
- [129] Laoutid F, Bonnaud L, Alexandre M, Lopez-Cuesta J-M, Dubois P. New prospects in flame retardant polymer materials: from fundamentals to nanocomposites. *Materials Science and Engineering: R: Reports* 2009;63:100-25.
- [130] Atay HY, Çelik E. Mechanical Properties of Flame-Retardant Huntite and Hydromagnesite-Reinforced Polymer Composites. *Polymer-Plastics Technology and Engineering* 2013;52:182-8.
- [131] Hollingbery L, Hull TR. The fire retardant effects of huntite in natural mixtures with hydromagnesite. *Polymer degradation and stability* 2012;97:504-12.
- [132] Boccaccini A, Keim S, Ma R, Li Y, Zhitomirsky I. Electrophoretic deposition of biomaterials. *JR Soc. Interface* 7. S581–S613 2010.
- [133] Scherrer BE, Wherry WB. Vibrational spectra of the alkaline earth double carbonates. *American Mineralogist* 1977;62:36-50.
- [134] Hollingbery L, Hull T. The thermal decomposition of huntite and hydromagnesite—a review. *Thermochimica Acta* 2010;509:1-11.
- [135] Vijayalakshmi U, Chellappa M, Anjaneyulu U, Manivasagam G, Sethu S. Influence of Coating Parameter and Sintering Atmosphere on the Corrosion Resistance Behavior of Electrophoretically Deposited Composite Coatings. *Materials and Manufacturing Processes* 2016;31:95-106.
- [136] Shen S, Pan C, Chang S, Lin S. Wet deposition process for thin-film transistors. *Materials and Manufacturing Processes* 2014;29:498-503.
- [137] Osouli-Bostanabad K, Aghajani H, Hosseinzade E, Maleki-Ghaleh H, Shakeri M. High Microwave Absorption of Nano-Fe<sub>3</sub>O<sub>4</sub> Deposited Electrophoretically on Carbon Fiber. *Materials and Manufacturing Processes* 2016;31:1351-6.
- [138] Picca RA, Sportelli MC, Hötger D, Manoli K, Kranz C, Mizaikoff B, et al. Electrosynthesis and characterization of ZnO nanoparticles as inorganic component in organic thin-film transistor active layers. *Electrochimica Acta* 2015;178:45-54.
- [139] Bonke SA, Wiechen M, Hocking RK, Fang XY, Lupton DW, MacFarlane DR, et al. Electrosynthesis of highly transparent cobalt oxide water oxidation catalyst films from cobalt aminopolycarboxylate complexes. *ChemSusChem* 2015;8:1394-403.
- [140] Su Y, Zhitomirsky I. Pulse electrosynthesis of MnO<sub>2</sub> electrodes for supercapacitors. *Advanced Engineering Materials* 2014;16:760-6.
- [141] Li Y, Pang X, Epan R, Zhitomirsky I. Electrodeposition of chitosan–hemoglobin films. *Materials Letters* 2011;65:1463-5.